Università degli Studi di Palermo

AREA RICERCA E TRASFERIMENTO TECNOLOGICO
SETTORE DOTTORATI E CONTRATTI PER LA RICERCA
U. O. DOTTORATI DI RICERCA

Dottorato di Ricerca in Scienze Fisiche e Chimiche
Dipartimento di Fisica e Chimica – Emilio Segrè
Settore Scientifico Disciplinare – FIS-05

MODELING OF STELLAR ACTIVITY OF STARS HOSTING PLANETS

IL DOTTORE
ALFREDO BIAGINI

IL COORDINATORE
MARCO CANNAS

IL TUTOR
GIUSEPPINA MICELA

EVENTUALE CO TUTOR
ANTONINO PETRALIA

CICLO XXVXVI
ANNO CONSEGUIMENTO TITOLO 2024

Contents

Abstract

Stellar activity is one of the main sources of noise in exoplanet observations, especially for planets orbiting around young stars, because they are characterized by a high level of variability that affects both the spectroscopic and photometric observations. To study planet formation in young planetary systems and achieve a level of precision high enough to study exoplanets atmospheres, we need to model the stellar activity, both through spectroscopy and photometry, to correct its effects in the observations.

As a prototype of a very active star, we observed and modeled the very young star V1298 Tau, hosting a multi-planetary system, through multiband photometry characterizing its active regions after validating the method on solar data. We also developed a technique to simulate stellar activity effects on transiting planetary spectra. The simulations were used to verify our atmospheric retrieval capability and establish the level of complexity necessary for achieving the corrections needed to correctly interpret low-resolution spectroscopic data.

Finally, we analyzed LHS 1140b HST low-resolution transit spectra to test the level of activity of the star and its effect on the retrieval of the atmospheric composition of the planet. In this specific case, we found that the spectrum distortions are not due to star activity but to the non-solar stellar composition of the target. This is a warning for future studies to test if in some cases signals attributed to activity are in fact due to a wrong estimation of stars' composition, and to outline the need to characterize very well the host star.

Chapter 1

Introduction

1.1 Exoplanets

The first exoplanets were discovered in the '90s (Michel Mayor and Queloz 1995) after decades of suspects and attempts and now there are thousands of exoplanets confirmed, mainly thanks to the recent spatial missions, such as Kepler (Borucki et al. 2010) and TESS (Ricker et al. 2015, Transiting Exoplanet Survey Satellite).
The first exoplanets discovered were the two orbiting around the pulsar PSR 1257+12 (Wolszczan and Frail 1992), in 1992, while the first exoplanet orbiting a main sequence star was discovered in 1995, 51 Pegasi b (Michel Mayor and Queloz 1995). In recent years, we have discovered different kinds of exoplanets.

For example, the Jupiter-like and Neptune-like are giant planets, made of gas, mostly H_2 and He, such as we can find in our Solar System. When a Jupiter-like planet or a Neptune-like one orbits close to its host star, it is called "hot Jupiter" or "hot Neptune". Some of them (called "ultra-hot jupiters" and "ultra-hot neptunes") can have a temperature of thousands of Kelvins, like for example Kelt-9 b that has an equilibrium temperature of ~ 4000 K (Borsa et al. 2019). This kind of planets have no counterpart in our own Solar System and the comprehension of their formation mechanism is a fundamental field of research in exoplanetary studies. Some models predict that they could form only beyond the snow line of their host star and then migrate towards the center of their systems, because otherwise their gas and ice would be wiped out by the star itself (Schoonenberg and Ormel 2017). According to most models, these planets could have migrated towards their stars because of gravitational instabilities, resulting in a leading constrain in planetary formation, but it

is unclear why this has happened only in some stellar systems (Morbidelli and Raymond 2016) and not in others, like our own. Finally, it should be noted that hot Jupiters and hot Neptunes may be larger than giant planets of the same mass because inflated due to their high temperatures. They also may present a certain loss of their atmosphere because of the thermal velocity of the atoms in their upper atmosphere and because of the stellar wind (Murray-Clay, Chiang, and Murray 2009).
Because of their large mass and radius, and their small distance from their host star, hot Jupiters are the easiest type of planet to observe, producing a bias in the mass distribution of the observed exoplanets.

The terrestrial planets are rocky, solid planets that have mass $\sim M_\oplus$. Terrestrial planets with masses between 1 $M_\oplus$ and 10 $M_\oplus$ are called "super-earths". The limit in radius between a super earth and a mini-Neptune is estimated as about 1.6 $R_\oplus$ (Rogers 2015), with an overlapping region.
A gap in the radius distribution of the short period (< 100 d) known exoplanets has been observed between 1.6 $R_\oplus$ and 2.0 $R_\oplus$ (Fulton et al. 2017). The leading hypothesis to explain this gap requires evaporation of a substantial fraction of the gaseous envelope from larger planets that migrate from the large radius peak to the small radius peak (e.g. Modirrousta-Galian, Locci, and Giuseppina Micela 2020).

Nowadays, there is much interest into super-earths because, even if frequent around other stars, there are no super-earths in our Solar System, so the properties of this kind of planets are mostly unknown. Moreover, some super-Earths are thought to be suitable for the development of life.

1.2 Radial Velocity Detection Method

Radial velocity method is one of the two main techniques to study exoplanets, together with transit method that we will describe in the following section. This method implies the study of the Doppler shift of stellar light through spectroscopy.
Because of the orbital motion around the center of mass of the planet-star system stars hosting planets have a periodical motion, from and toward us, depending on the inclination

of the system. We can measure this motion thanks to the Doppler shift of the spectral lines of the star: we see a blue-shift when the star comes toward Earth, and a redshift when the star goes in the opposite direction.
From the periodicity of the motion of the spectral lines, the researcher can extract a periodogram with a Fourier transform of the data and find the frequencies related to the planets orbits.
The radial velocity method is capable of measuring a lower limit for the planetary mass because it measures directly the product $\mathrm{M} \cdot \sin \mathrm{i}$ where i is the angle between the orbital plane of the planet and our line of sight. Corrections for eccentricity are needed too in the calculations. This method is suitable to study exoplanets from Earth, but it requires many observations with a large telescope (diameter $>$ 1m) during a long time and it requires a high resolution and stable spectrographs. The planets easier to discover and study with this method are the hot Jupiters because their high mass and short orbital period ($<$ 10 days) produce large variations of stellar radial velocity.
This method can be combined with transit observations to constrain inclination and measure the planetary mass and radius.

1.3 Transit Method

Observing exoplanetary transits is the most prolific method to detect and study exoplanets. A transit occurs when a planet passes between its star and the observer during its orbital motion. The occultation of a fraction of the star surface leads to a decrease of the light that we measure, with a characteristic light-curve (see Figure 1.1) (Mandel and Agol 2002) with a maximum decrease in the observed stellar flux F_* described by:

$$\frac{\Delta F}{F_*} \sim (\frac{R_p}{R_*})^2 \tag{1.3.1}$$

where ΔF is the maximum difference in flux during the transit and $\mathrm{R_p}$ and R_* are the radii of the planet and star respectively. Given the usual difference between the dimensions of planets and stars, we expect a very narrow effect, enlightening the necessity of high signal-to-noise ratio (SNR) and the difficulties in small planet detection and study. For example, a transit of Earth seen from outside the Solar System would give a $\frac{\Delta \mathrm{F}}{\mathrm{F}_*}$ of about $< 1/10000$. In the case of Jupiter we have a ratio of $\sim 1/100$ instead, enhancing how tougher is to get

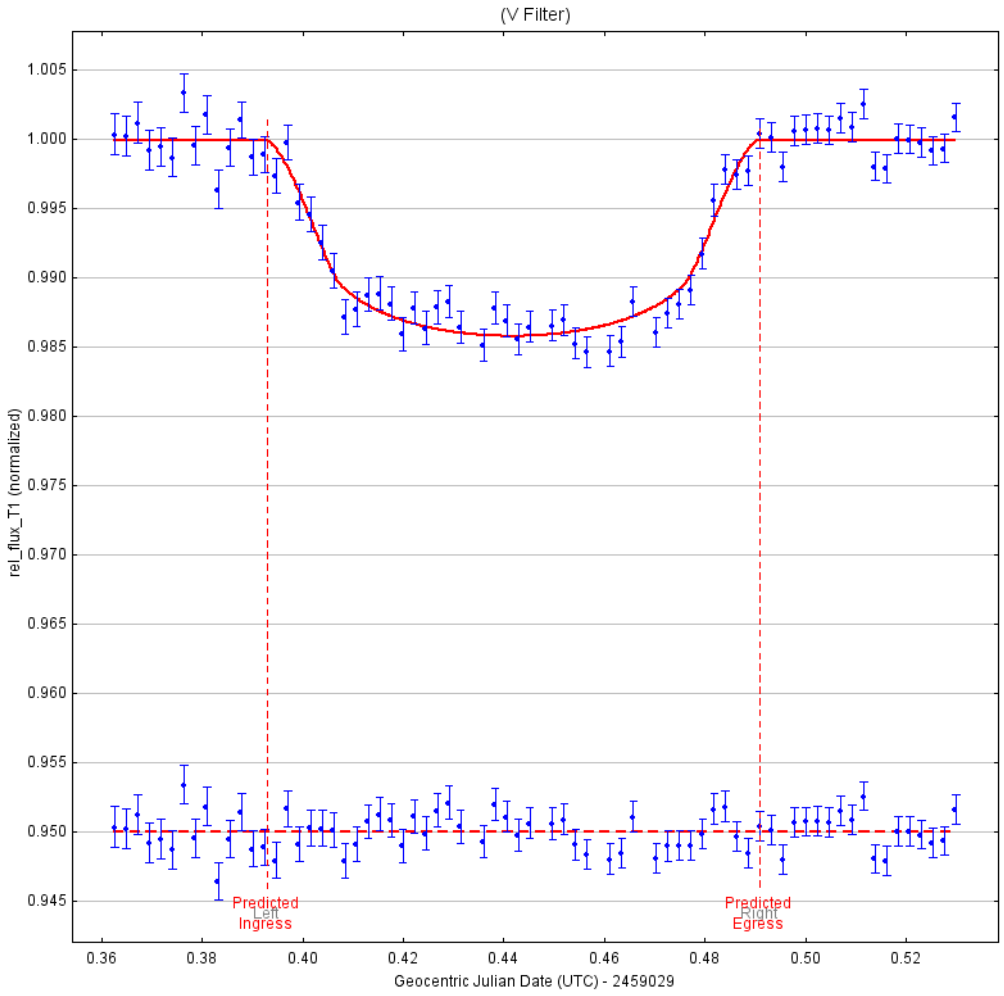

Figure 1.1: Example of the typical light-curve of a transit. This is the transit of HAT-P-23 b as observed from Osservatorio Polifunzionale del Chianti (OPC) in June 2020.

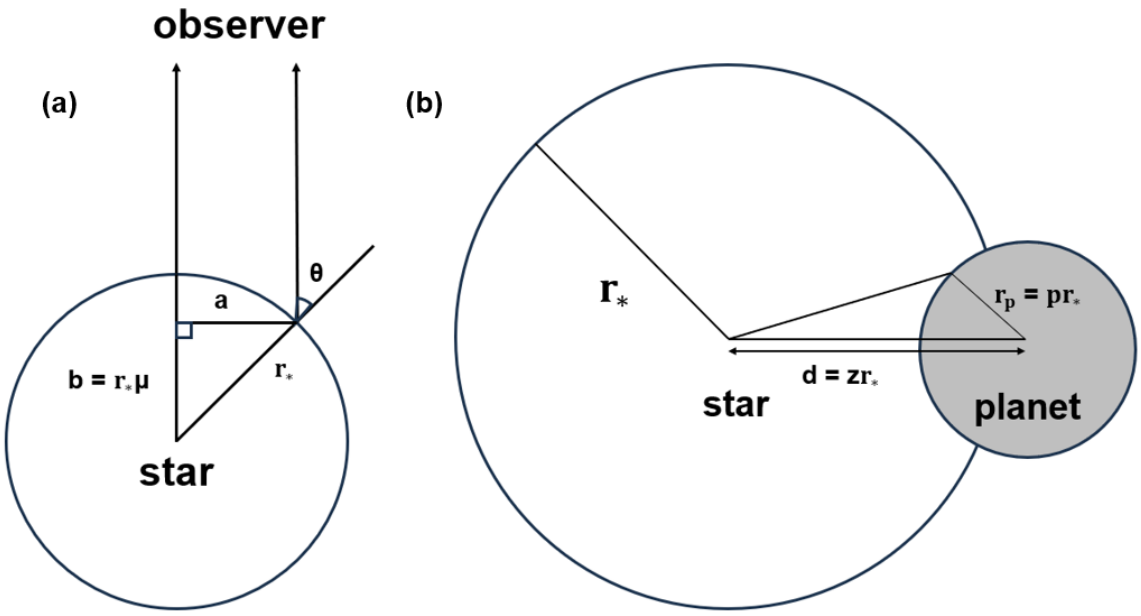

Figure 1.2: Right: Geometric scheme of limb darkening effect. Left: Transit geometric scheme, adapted from Mandel and Agol 2002

high SNR for small planets with respect to the giant ones. If the planet has an atmosphere, we expect to observe a change in the observed spectrum of the star during the transit, with spectral features due to molecules, clouds and to absorption/scattering processes in the planetary atmosphere itself.

In a transit observation, usually we are only interested in measuring a relative flux variation using Eq. 1.3.1 to measure the planetary radius. Knowing its value is fundamental because it can help us to constrain the inclination and, together with radial velocity observations, its density.

1.3.1 Radius Measurements

If we consider a uniform disk, the equations that describe the flux reduction during the transit are (Mandel and Agol 2002; Seager and Mallén-Ornelas 2003):

$$\begin{cases} 1 & z > 1 + p \\ 1 - \frac{1}{\pi}(p^2 k_0 + k_1 - \sqrt{\frac{4z^2 - (1 + z^2 - p^2)^2}{4}}) & 1 - p < z \leq 1 + p \\ 1 - p^2 & z \leq 1 - p \end{cases}$$

where:

- r_p and r_* are the planet and star radii respectively (see Figure 1.2)
- $\mathrm{p} = \mathrm{r_p}/\mathrm{r_*}$
- d is the distance between the center of the planet and the center of the star
- $z = d/r_*$
- $k_0 = \cos^{-1}[(p^2 + z^2 - 1)/2pz]$
- $k_1 = \cos^{-1}[(1 - p^2 + z^2)/2z]$

The hypothesis that the star can be considered a uniform disk is an approximation because the equations above do not take into account the limb darkening, an effect that makes the star brighter in the center with respect to the border, modifying the transit light-curve. This effect can be schematized as follows [1]:

$$I(r) = I(0)[1 - u(1 - \sqrt{\frac{(a^2 - r^2)}{r^2}})] \tag{1.3.2}$$

where a and r are the parameters of Figure 1.2 and u is the linear limb darkening coefficient. It is also possible to achieve slightly higher precision with a quadratic approximation using this alternative equation [2]:

$$I(r) = I(0)[1 - a(1 - \cos\theta) - b\sin^2\theta] \tag{1.3.3}$$

with a and b coefficients depending on the wavelength analyzed. Finally, it is possible a non-linear schematization of limb darkening as Claret 2000:

$$I(r) = 1 - \sum_{n=1}^{4} c_n(1 - \mu^{n/2}) \tag{1.3.4}$$

$$F(p, z) = \left[\int_0^1 2rI(r)\,dr\right]^{-1} \int_0^1 I(r)\frac{d[F^e(p/r, z/r)r^2]}{dr}dr \tag{1.3.5}$$

[1] `https://www.astro.uvic.ca/~tatum/stellatm/atm6.pdf`
[2] `https://www.astro.uvic.ca/~tatum/stellatm/atm6.pdf`

where $\mu = \cos\theta = (1 - r^2)^{1/2}$ with $0 \leq r \leq 1$ (radius normalized to stellar radius), I(r) is the specific intensity and F^e is the ideal transit light-curve without limb darkening effect. Note that $I(0) = 1$.

These coefficients are usually tabulated (Claret 2000), but can also be estimated by studying the ingress/egress part of the light-curve (K. A. Collins, Kielkopf, et al. 2017).

Observing a transit is possible to measure ΔF, t_f, t_t e P, where ΔF is the stellar flux variation during the transit, t_f is the time range of the flat part of the transit curve, t_t is the total duration of the transit (see Figure 1.3) and P is the period of the transit.

With the following assumptions and using the formalism of Seager and Mallén-Ornelas 2003:

- circular orbits, reasonable for planets very close to their host star, due to tidal effects
- $M_p << M_*$
- negligible planet luminosity
- known relation between stellar mass and radius, reasonable for main sequence stars
- the central part of the transit light-curve is nearly flat
- enough precision in the orbital period determination

we can use this system of equations:

$$\Delta F = (R_p/R_*)^2 \tag{1.3.6}$$

$$\frac{\sin(t_f\pi/P)}{\sin(t_t\pi/P)} = \frac{[1 - (R_p/R_*)]^2 - [(a/R_*)\cos i]^{2\,1/2}}{[1 - (R_p/R_*)]^2 + [(a/R_*)\cos i]^{2\,1/2}} \tag{1.3.7}$$

$$t_t = \frac{P}{\pi}\arcsin\left(\frac{R_*}{a}\frac{[1 + R_p/R_*]^2 - [(a/R_*)\cos i]^{2\,1/2}}{1 - \cos^2 i}\right) \tag{1.3.8}$$

$$P^2 = \frac{4\pi^2 a^3}{GM_*} \tag{1.3.9}$$

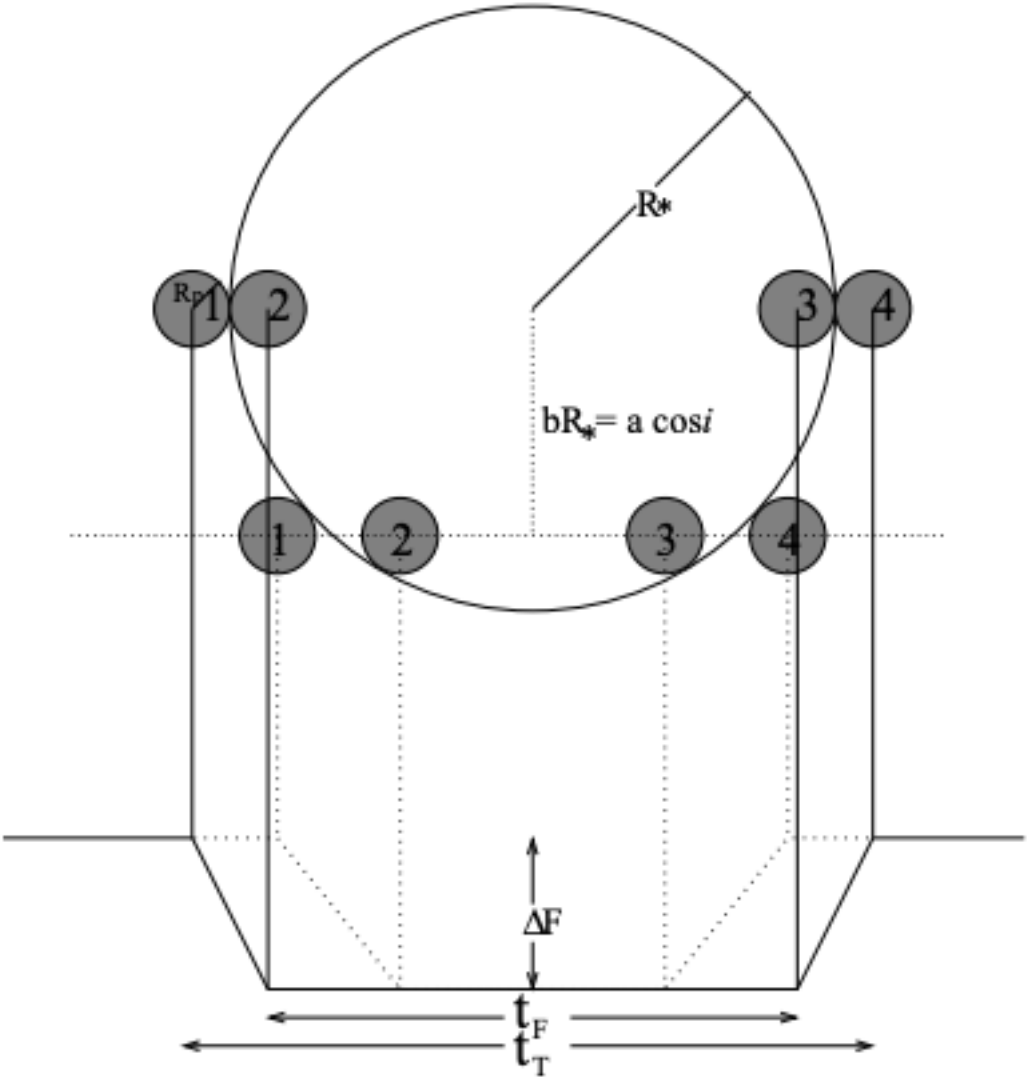

Figure 1.3: Transit phases scheme (Seager and Mallén-Ornelas 2003) that shows the different phases of an exoplanet transits and how their duration depends on the parameter of impact of the transit, b.

$$R_* = KM_*^x \tag{1.3.10}$$

where Eq. 1.3.9 is the Third Kepler's Law and Eq. 1.3.10 is the typical power law for main sequence stars. With this procedure, it is possible to derive the following parameters:

- major semi-axis of planetary orbit, a
- the stellar mass, M_*

- the planetary radius, R_p
- the radius of the star, R_*
- inclination angle of the planetary orbit with respect to line of sight, i.

1.3.2 Photometric observations

The transit method is applied to observations from space as those from spatial telescopes like CoRot (Auvergne et al. 2009), Kepler and TESS and also from ground campaigns, including the project ExoClock (Kokori et al. 2022). This method can be used to detect a large number of planets and, through repeated observations, measure the period of the orbit. Because of the presence of spots, whose effect on the stellar light-curve can be exchanged with that of a planet, it's fundamental to observe an exoplanet candidate during several periods to confirm its nature. Other effects, as the presence of variable sources contaminating the target, can produce false positive as well. Usually, this method is performed observing through only one photometrical band, scanning large areas of the sky. Obviously, only a fraction of the planetary systems is detectable through the transit method. The probability of detection through transit method for a planet is described as follows:

$$P_T \sim R_*/a \tag{1.3.11}$$

where P_T is the probability of transit observation, R_* is the stellar radius and a is the semi-axis of the planetary orbit. This probability is higher for planets close to their star and with large radius, creating a bias towards hot Jupiters.
In some cases, it is possible to use photometric transit observations to study also some of the non-transiting planets of the system, through two methods: TTV ("Transit Timing Variations") and TDV ("Transit Duration Variations"). These methods rely on the gravitational pull that the non-transiting planets have on the transiting one. The second planet gravity changes the semi-axis of the transiting planet orbit, a, its eccentricity e, and its periastron angle ω. These effects lead to a periodic variation of the periodicity of the transit.

1.3.3 Transit Spectral Analysis

When stellar light impacts on a planet can be altered by its atmosphere: molecules absorption, Rayleigh scattering, clouds and haze can obscure selected wavelengths leading to a measure of the planetary radius that changes along the observed spectrum. The measure of the changing planetary radius is the planetary spectrum. Observing planetary spectra is fundamental to find evidence of their atmosphere and to retrieve its temperature profile and composition, possibly looking for molecular signatures of habitability like e.g. H_2O, CH_4 and O_2. This kind of observation requires taking many stellar spectra during every phase of the transit and to fit the transit light-curve for each spectral bin, finding the planetary spectrum as the array of different values R_λ (planetary radius) measured at each wavelength λ.

The analysis of planetary atmospheres is usually difficult for three main reasons:

- stellar activity presents chromatic effects that resemble those due to a planetary atmosphere, leading to a wrong estimate of the planetary radius.
- the very narrow effect of the transit on the total flux requires very large spectral SNR during transit observations to have enough signal for the planetary spectrum.
- other components of atmosphere (i.e. clouds) that can hide the signatures of its chemical composition.

In particular, clouds and hazes can hide some molecular lines absorbing stellar light at short wavelengths. Moreover, Rayleigh scattering, i.e. the elastic scattering of light due to the particles in the atmosphere, whose efficiency is proportional to $\sim \frac{1}{\lambda^4}$, contributes in hiding molecular signatures (Seinfeld, Pandis, and Noone 1998; Sneep and Ubachs 2005). Finally, the possibility of overlapping molecular lines could lead to a wrong retrieval of molecules presence in the atmosphere.

1.4 Stellar Activity

The analysis of exoplanetary transit described above is based on the assumption of a uniform and quiet stellar surface, thus reducing the transit to a purely geometrical effect, but this is not the case for active stars. Stellar variability involves a variety of inhomogeneities on the

stellar surface, produced by the magnetic activity of the interior of the star (Berdyugina 2005) that leads to a large variety of phenomena like expansion/contractions of the star, stellar spots (Solanki 2003), faculae and flares (Ballerini et al. 2012) and their intrinsic evolution with a large variety of timescales: minutes-days for flares, days for the evolution of the active regions (faculae and spots) on the stellar surface, years for active regions cycles, billions of years for the evolution of the magnetic activity of the star (Berdyugina 2005).
The analysis of the stellar activity is crucial for understanding the stellar processes. Moreover, it is also fundamental for exoplanetary observations, since it is the main source of noise both for photometry and spectroscopy (e.g. Pont, Knutson, et al. 2008; Czesla et al. 2009; Sing, Désert, Lecavelier Des Etangs, et al. 2009; Sing, Pont, et al. 2011; Sing, Désert, Fortney, et al. 2011; Agol et al. 2010; Désert et al. 2011; Berta, Charbonneau, et al. 2011; Ballerini et al. 2012; Giuseppina Micela 2015; Scandariato and Giuseppina Micela 2015).
The presence of stellar spots, for example, can interfere with high resolution spectroscopic observations causing a distortion of the spectral lines affecting the estimate of the radial velocity of the star. It can also affect the photometric curves analysis hiding, simulating or modifying the signal of a transit in the stellar light-curve. Furthermore, stellar activity could affect the extraction of the exoplanetary transmission spectra, hampering the detection of atmospheric molecules and atmospheric features like clouds (Pont, Knutson, et al. 2008; Ballerini et al. 2012; Giuseppina Micela 2015).
The modelling of the stellar inhomegeneities on the stellar surface, could play a crucial role in the search and characterization of exoplanetary atmosphere for missions such as JWST (Greene et al. 2016, James Webb Space Telescope) and for the incoming ARIEL mission (Giovanna Tinetti et al. 2018, Atmospheric Remote-Sensing Infrared Exoplanet Large-survey), the M4-ESA mission dedicated to study the exoplanetary atmospheres.
Stellar activity is a very common phenomenon among solar-type stars with convective outer layers, but it is even more pronounced in young stars. Despite this, in recent years, young stars have become targets of significant interest because they can provide valuable insights into the early stages of formation and evolution of exoplanetary systems (Carleo et al. 2020).
It has been also verified that stellar activity is enhanced in fast rotating stars (Noyes et al. 1984) and this is in accordance with clues about a reduction of stellar rotation as the star ages (Skumanich 1972).

In recent years, ground- and space-based facilities have enabled us to discover thousands of exoplanets orbiting various types of stars, revealing a variety of these bodies with characteristics different from those of our own Solar System as seen in Section 1.
In order to observe and study both young planetary systems and exoplanetary atmospheres, it is fundamental to correctly model the stellar activity of the host stars to remove its effects from the observational data and to study its impact on planets.

1.4.1 Sources of Stellar Activity

The main phenomena involved in stellar activity on short-medium temporal scales are

- pulsations and granulation
- flares
- faculae
- spots

1.4.2 Pulsations and granulation

Pulsations are p-mode oscillatory waves (Sarkar et al. 2018) due to stellar convection in the external layers of the star and have a typical timescale of $\sim$ 3-15 minutes. Granulation is also the result of convection near the surface of the star. The dimension of the granulations cell depends on the plasma density, with a range between 0.3 (M stars) and 5 x 10^8 cm (F stars) (Beeck et al. 2013) with variations within a timescale of $\sim$ 10-22 minutes (Giuseppina Micela 2015). Granulation induced optical brightness fluctuations are stronger in hotter stars and decrease for cooler stars, because the plasma opacity arising at low temperatures reduces this brightness contrast inducing a transition to radiative regime near the photosphere, halting the granulation far deeper in the star: for example in a K0V star the external brightness fluctuation is reduced of $\sim 34\%$ with respect to the granulation effects expected to occur beneath the surface (Beeck et al. 2013). Granulation has no relevant effects on exoplanetary observations because the typical granulation cells are much smaller than planets, so their effect is averaged on a planetary scale. Any residual effect though can

be modelled using out-of-transit observation of the star (Sarkar et al. 2018).

1.4.3 Flares

Flares are very strong electromagnetic bursts that greatly enhance stellar luminosity in every spectral band, from X-rays to radio waves, on a timescale between seconds and days (Kowalski 2024). The origin mechanism of flares is the transfer of accumulated potential magnetic energy, due to plasma motions inside the star, to the stellar atmosphere, because of the magnetic reconnection of magnetic field lines. This energy is converted in kinetic energy of atmospheric plasma and then is next released through thermal radiation and non-thermal radiation. Non-thermal radiation origins from the rapid acceleration of charged particles to mildly relativistic energy (from $\sim$ 10 KeV to MeVKowalski 2024) due to magnetic reconnection. The best studied flares are solar flares, that have a bolometric energy $E_{bol} \sim 3 - 6$ x 10^{22} erg, but stellar flares may reach much higher energy, $\sim 10^2 - 10^4$ times the energy of the sunflares. These are called "super-flares" and mostly happen around young stars (Kowalski 2024). Stellar flares are a dominant source of stellar variability and have a timescale similar to or shorter than that of a transit. They are difficult to correct, but have the advantage of being easily detectable, for example through H alpha emission, so data affected by flares can be discarded from the analysis (Giuseppina Micela 2015).

1.4.4 Faculae

Faculae are bright regions on the stellar surface due to local magnetic fields that enhance the local temperature and so the radiance emission of the photosphere and chromosphere. They are usually linked to chromospheric plages (Solanki, Inhester, and Schüssler 2006; Chatzistergos et al. 2022), localized regions of bright chromospheric emission. On the Sun faculae contribution to the continuum emission is negligible near the center and maximum at the limb of the solar disk, where the contrast with the photosphere is enhanced due to limb darkening, while instead the chromospheric plages emission does not depend on their position on the stellar disk. Finally, a spectral feature linked to faculae and plages is Ca II H and K emission (Pizzolato et al. 2003; Xu, Gu, and Ioannidis 2021). It should be noted that faculae enhanced emission gives the Sun a total flux higher at the peak of its activity,

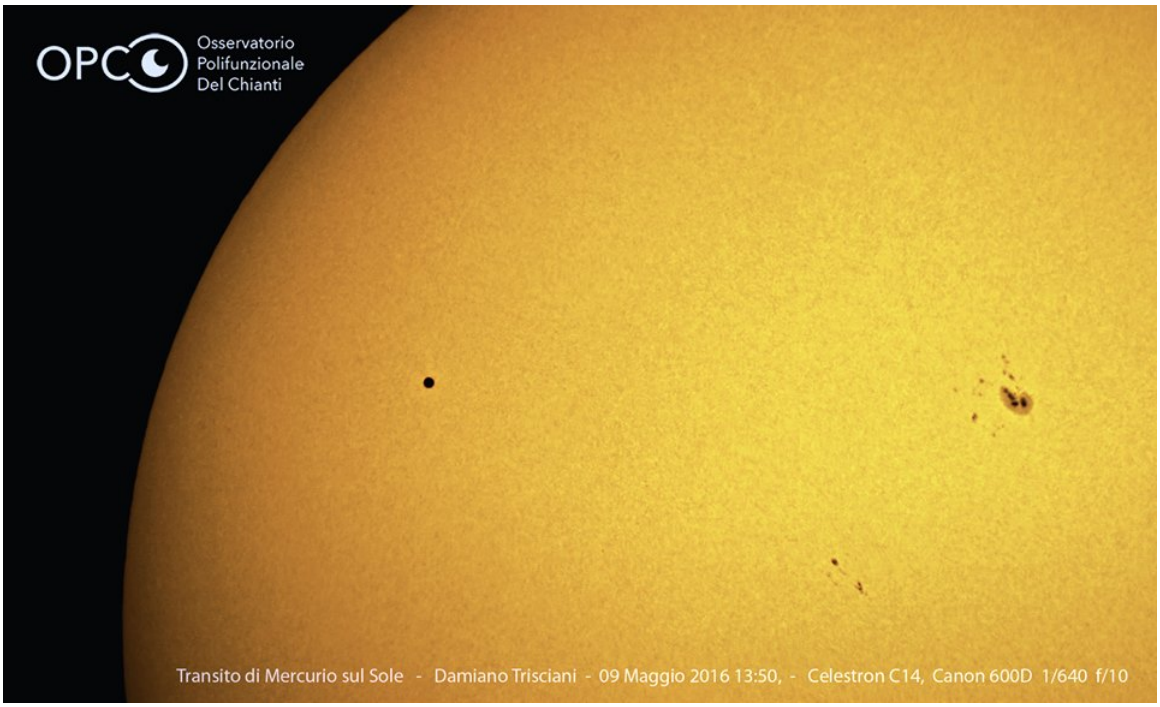

Figure 1.4: Image of the transit of Mercury observed by OPC, where a sunspot is visible near the planet. It is clear that Mercury and the sunspot have comparable size.

despite the presence of sunspots, i.e. overcompensating their lower emission with respect to the quiet surface, so they must be considered in stellar activity studies. On the Sun, single faculae do not live as long as sunspots, but faculae regions as a whole usually live three times longer than spots (Ash et al. 2020). Usually, faculae are not a relevant source of noise in exoplanets observations because their difference of temperature with respect to the quiet photosphere is small (Giuseppina Micela 2015). However, it is possible to model them as bright spots, at least for photometric and spectral low resolution analysis.

1.4.5 Spots

Stellar spots are regions of the stellar surface with a lower temperature with respect to the quiet stellar surface because the local magnetic field configuration halts the convection process, leading to a local cooling of the stellar plasma together with a change in local gravity (Berdyugina 2005; Ballerini et al. 2012). In particular, in this thesis we will consider only the change in temperature in the spots, with the hypothesis that local gravity and magnetic field changes have much more little effects on stellar observations.

Spots can last few days or for a timescale related to the period of rotation of the star, but there are also some cases of spots that lasted decades (Berdyugina 2005). In many cases what is observed is a complex region with many spots and not a unique large stable spot (Berdyugina 2005). On the Sun, spots number changes during a cycle 11 years long, but till now there is debate about the detection of similar cycles on other stars (Pizzolato et al. 2003). Their origin is strictly related to the stellar dynamo and consequently to the rotation of the star that affects the magnetic field lines in its plasma (Berdyugina 2005)

Effect of spots on transits observations

Due to their lower temperature with respect to the stellar surface, the spots' emission curve differs from that of the quiet photosphere, thereby altering the photometric signal, with an effect that decreases with wavelength, or distorting the spectral lines of the star and leading to incorrect radial velocity measurements (Berdyugina 2005). For instance, during a photometric observation, the presence of a spot occulted by a transiting planet can produce bumps in the observed light-curve. This occurs because the planet obscures a region with a lower flux compared to the unspotted surface, increasing the observed average intensity coming from the star (Czesla et al. 2009; Sing, Pont, et al. 2011). This effect cannot be ignored even for relatively quiet stars because spots and planets may have similar size. As an example, Figure 1.4 shows the image of the Sun during a Mercury transit, taken at Osservatorio Polifunzionale del Chianti (OPC) on May 9th, 2016. The image shows clearly that the spot's complex on the right of the image is larger than the size of the projected disk of the planet (on the left).

Furthermore, also an unocculted spot can affect the measurement of the transit depth (Czesla et al. 2009) without clear signs of its presence, leading to incorrect estimations of the exoplanets parameters. In particular, the chromaticity of these effects leads to inaccurate measures of the planetary radius. In a first approximation, ignoring faculae and limb darkening contribution, the spots chromatic contamination leads to spectral change factors ϵ_λ as follows:

$$\epsilon_\lambda = \frac{1}{1 - ff_{spot}\left(1 - \frac{S_{\lambda,spot}}{S_{\lambda,phot}}\right)} \tag{1.4.1}$$

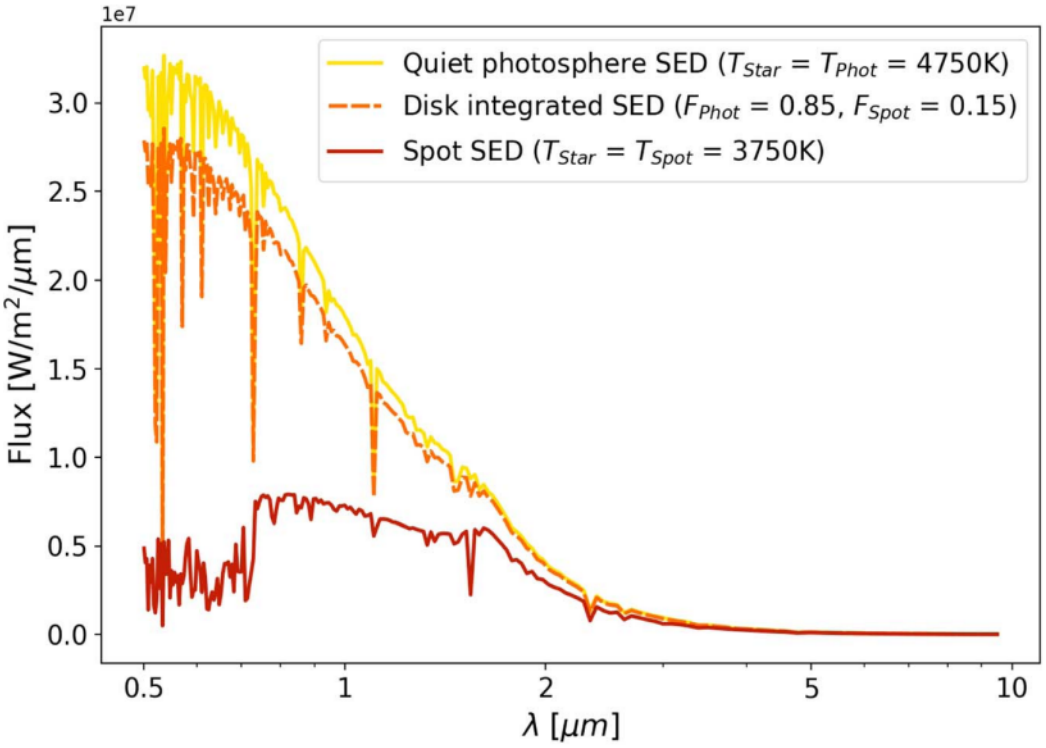

Figure 1.5: The two solid line spectral emission densities (SEDs) correspond to the two temperature of the components that make up the surface of an active, heterogeneous star with T_{phot} = 4750 K (yellow) for the photosphere, and the cooler starspot with a T_{spot} = 3750 K (red). The orange-dashed line SED represents the average, disk-integrated SED that would be observed in accordance with Eq. 1.4.1 due to the weighted contributions of the quiet photosphere and the spot, assuming a spot filling factor of ff_{spot} = 0.15 (Thompson et al. 2024).

where ff_{spot} is the spot filling factor (the ratio between the visible spots surface and the total visible surface of the star) and $S_{\lambda,phot}$ and $S_{\lambda,spot}$ are the photosphere and spots averaged spectra respectively (see Figure 1.5).

Finally, in the unocculted spot case, the measured atmospheric spectrum in each wavelength λ will be $R_\lambda = \epsilon_\lambda * R_{0,\lambda}$, where $R_{0,\lambda}$ is the real spectrum of planetary atmosphere. This chromatic distortion can also heavily affect one-photometric band observations, leading to different measurements of the planetary radius in observations performed using different photometric filters.

The presence of a spot can also mimic a transit and, as a consequence, more than multiple observations are needed to confirm the presence of a transiting planet, taking advantage of

the stability of the planetary signal with respect to the evolving stellar activity-related signal.
A number of methods to extract the planetary spectrum taking into account the stellar activity have been proposed in literature (Czesla et al. 2009; Sing, Désert, Fortney, et al. 2011; Ballerini et al. 2012; Giuseppina Micela 2015; Cracchiolo, G. Micela, and Peres 2021; Cracchiolo, G. Micela, Morello, et al. 2021; Thompson et al. 2023).

1.5 Activity Indicators

The level of activity of a star can be derived by many indicators. First, we can use photometric observations to verify if there is any modulation of the light-curve of a star. In case of relevant flux variations of the star, it is possible through a periodogramm to retrieve the presence of periodicities of its fluctuations. During this procedure it is very important to distinguish the modulation due to the period of rotation of the star (that indicates the presence of spots or faculae on its surface) from flares signals, eclipses due to another star or contaminant of the system or any planetary transits. Then spectral indicators are fundamental. The most used are CaII H-K and H alpha lines that are tracers of magnetic active regions on the stellar surface. CaII H-K and H alpha emission occur in the chromosphere of the star as is evident from solar observations where their emission tracks with great precision the active regions of the surface (Ash et al. 2020). It has been found that usually there is a correlation between CaII H-K and H alpha emissions, but with a great scatter, and an anticorrelation between the timing of their emission and the photometric light-curve of the star (Xu, Gu, and Ioannidis 2021).

1.6 Thesis structure

Observations' methods and the instruments are described in Chapter 2. In Chapter 3 we describe our multiband photometric analysis of V1298 Tau, an active young star. In Chapter 4 we describe our new spectral simulation and retrieval code, STARPA, and its applications to M dwarves spectra. In Chapter 5 we describe the study of the activity and composition of a specific M dwarf, LHS1140, and of the atmosphere of its exoplanet b and in chapter

6 it is shown a short list of the papers part of this PhD work. Conclusion are discussed in Chapter 7. Finally, other products of this PhD work will be listed in Appendix A.

Chapter 2

Instruments and data reduction

2.1 Small-Medium Telescopes

Large ground-based and spatial telescopes are fundamental to study stars and other astronomical objects with extreme precision, but their use is strictly regulated and it is very difficult to obtain enough observing time. When an extreme data precision is not necessary (for example in some photometric observations) and instead it is fundamental to have a flexible schedule for observations, little and medium-sized telescopes (with a diameter between 30 cm and 1.5 m) can be very useful. This is the case for transient and variable objects observations, like near earth-objects (NEO), young stars, transits and also the optical counterparts of gamma ray bursts or gravitational waves, especially as part of extended follow-up projects of important scientific missions. Here we will show three small-medium telescopes used in this PhD work.

2.1.1 OPC Telescope

The Osservatorio Polifunzionale del Chianti (OPC, Figure 2.1) is an astronomical observatory near Florence, Italy, with the following coordinates:

- latitude: 43 11 24 N
- longitude: 11 14 44 E
- altitude: 455 m

It is specialized in the photometric observations of exoplanetary transits and in young stars observations and is part of the follow-up of TESS mission, GAPS (Global Architecture

Figure 2.1: Photo of Osservatorio Polifunzionale del Chianti

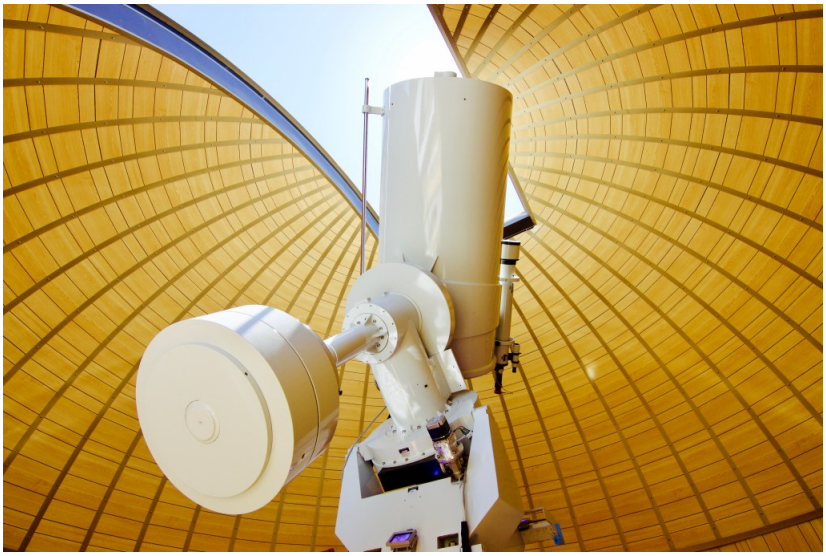

Figure 2.2: OPC Telescope.

of Planetary Systems, Covino et al. 2013) programme and ExoClock Project (part of the follow-up of Ariel mission). Moreover, it was also part of the KELT-FUN (or KFUN K. A. Collins, K. I. Collins, et al. 2018) follow up too, until the end of the project.
OPC is equipped with a Ritchey-Chretien telescope (Figure 2.2), an F/8 telescope with a diameter of 800 mm and a german mount type.

Parameter	Typical Value
Architecture	Full Frame CCD
Total Number of Pixels	1552 (H) x 1032 (V)
Number of Active Pixels	1536 (H) x 1024 (V) = approx. 1.6 M
Pixel Size	9.0 µm (H) x 9.0 µm (V)
Active Image Size	13.8 mm (H) x 9.2 mm (V)
Die Size	15.5 mm (H) x 10 mm (V)
Aspect Ratio	3:2
Saturation Signal	100,000 electrons
Output Sensitivity	10 µV/e^-
Quantum Efficiency (with microlens)	Peak: 77% 400 nm: 45%
Quantum Efficiency (no microlens)	Peak: 65% 400 nm: 30%
Read Noise	15 electrons
Dark Current (T = 25 °C)	<10 pA/cm^2
Dark Current Doubling Temperature	6.3 °C
Dynamic Range	74 dB
Charge Transfer Efficiency	>0.99999
Blooming Suppression	None
Maximum Data Rate	10 MHz
Package	CERDIP Package (sidebrazed)
Cover Glass	Clear or AR coated, 2sides

Figure 2.3: Scientific camera properties. Parameters above are specified at 25 °C, unless otherwise noted. [2]

Cameras

The scientific camera of OPC is a Moravian KAF-09000 [1], with the properties shown in Figures 2.3 and 2.4, that observes a wide field of view (FoV) of 19.7' x 19.7'. This large field allows us to have enough check stars to confront the target star luminosity with. The scientific camera has a filter wheel with Johnson U, B, V, R and I filters. Their transmission curves are shown in Figure 2.5.

The pointing camera is a QHY5II model with a MT9M001 sensor, pixel size of 5.6 micron, a resolution of 1280 x 1024 and a QE of 56%.

In order to control the telescope OPC uses OnStep software [4], while to track the objects during observations OPC uses Homer, a software developed by OPC research group, that analyzes the scientific images to calculate the RA and DEC shifts of the telescope and

[1] `https://www.onsemi.com/download/data-sheet/pdf/kaf-09000-d.pdf`
[2] `https://www.onsemi.com/download/data-sheet/pdf/kaf-09000-d.pdf`
[3] `https://www.onsemi.com/download/data-sheet/pdf/kaf-09000-d.pdf`
[4] `https://github.com/hjd1964/OnStep`

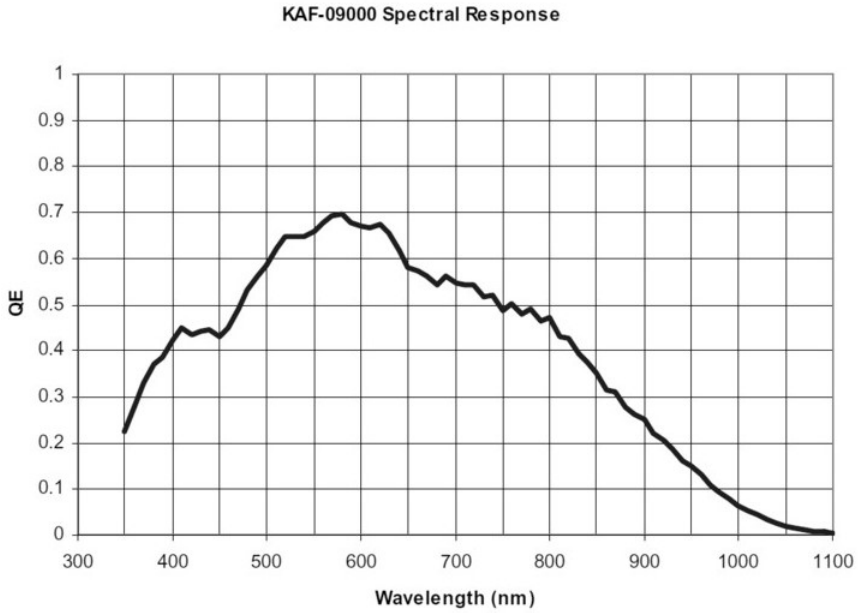

Figure 2.4: Quantum efficiency (QE) of the scientific camera detector. [3]

correct them with little movements of the telescope stepped motors.

2.1.2 Gal-Hassin Telescope

Gal-Hassin is an astronomical observatory near Isnello, in Madonie National Park (Palermo), at about 600 m above the sea level. It has a telescope, called GRT1 (Figure 2.6), with the following characteristics:

- Type: Ritchey-Chretien
- Diameter: 400 mm
- F/3.8
- GM3000-HPS mount that assures a 1"/15 min accuracy during tracking and a pointing velocity of 10°/sec

The scientific camera of Gal-Hassin is a CCD KAF-16803, 36.9mm x 36.9mm and 4096x4096 pixel for a resolution of 1.22"/pixel. Combining the camera dimensions with the focal length of the telescope, the total resulting FoV is 83' x 83' corrected through a field leveler. This wide FoV is very useful in order to have as many reference stars as possible to study the

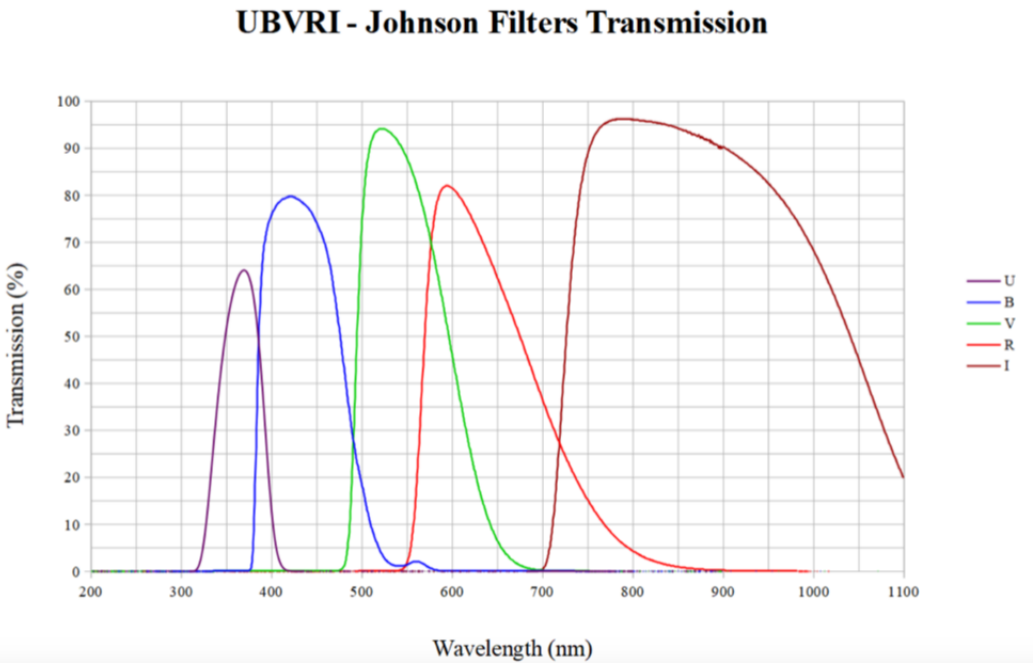

Figure 2.5: Transmission curves of scientific camera filters, Johnson U, B, V, R and I at OPC.

variability of the observed target. The available filters are SLOAN u', g', r', i', z' and two narrow band filters OIII and H alpha. Gal-Hassin observatory research focus is the observation of NEO (Near Earth Objects), exoplanetary transits and young objects.

2.1.3 REM Telescope

REM (Rapid Eye Movement) is a telescope located at ESO Chilean Observatory, La Silla, Chile (E. Molinari et al. 2004). It is a fast Ritchey-Chretien telescope (see Figure 2.7) with a diameter of 60 cm that can be used for simultaneous photometric observations in optical and infrared bands thanks to a dichroic that splits the light and sends it to two different instruments: ROS2, for the optical band, and REMIR for the IR bands. ROS2 is an optical camera (400-950 nm) with Sloan filters g', r', z' and i' and a FoV of 9.1'x9.1' that leads to a pixel scale of 0.58 arcsec/pixel (Emilio Molinari et al. 2014). The transmission functions of ROS2 filters are shown in Figure 2.8. REMIR is an IR camera (1-2.3 micron, Conconi et al. 2004) that observes through a Sloan z filter and standard J, H and Ks filters (whose

[5] http://www.rem.inaf.it/
[6] http://www.rem.inaf.it/?p=instruments
[7] http://www.rem.inaf.it/remir.html

Figure 2.6: GRT1 telescope at Gal-Hassin observatory

transmission functions are shown in Figure 2.9). It also has a low resolution grism (R $\sim$ 60) and a narrow filter at 2.2 micron for H_2 transition observations. The camera is mounted on a wheel in order to dither, i.e. shift the images to subtract sky background. REMIR temperature is kept at $\sim$ 77 K thanks to a Stirling cryocooler.

Figure 2.7: REM telescope.[5]

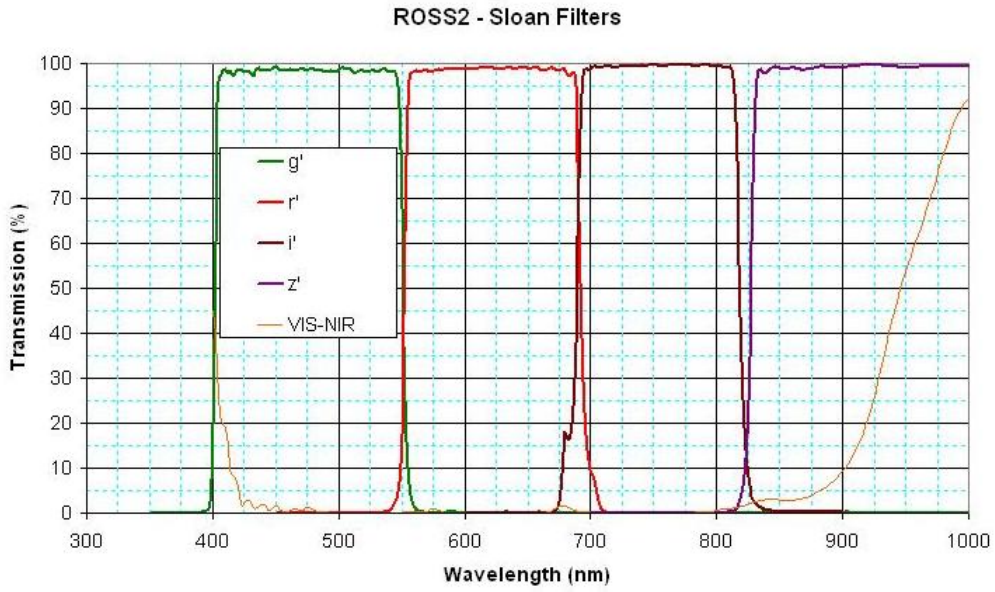

Figure 2.8: Transmission functions of Sloan filter of ROS2 detector. [6]

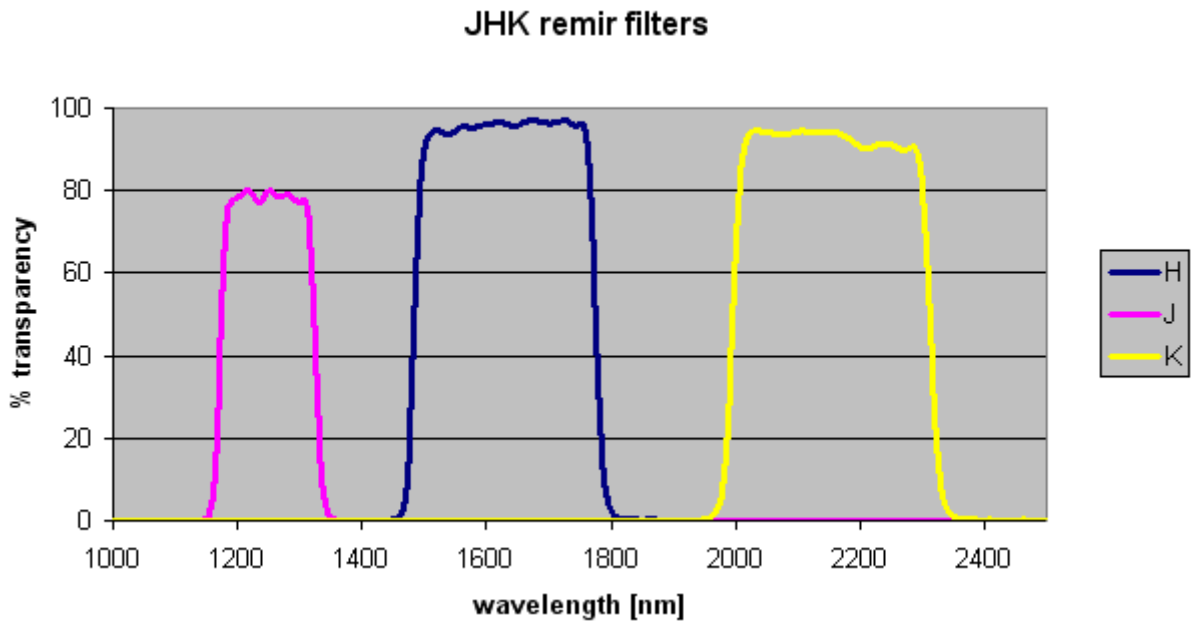

Figure 2.9: Transmission functions of J, H and K filters of REMIR detector[7].

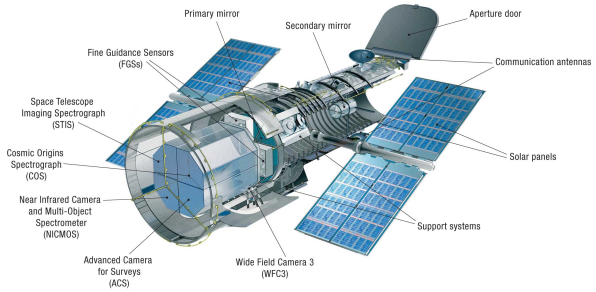

Figure 2.10: Scheme of Hubble instruments location, from [8]

2.2 Space Missions

Earth's atmosphere is the main obstacle in astronomical observations. It absorbs some wavelengths like X-rays, water molecule lines and UV, dulls and scatters the light from stars through Rayleigh scattering and the weather can prevent observations for weeks, especially during winter. Moreover, scattered light from Sun and Moon totally prevents observations during daytime and almost totally during full Moon nights.
Observing from Space is the main way to acquire high quality data without these limitations, but there are some technological and financial constraints. An instrument for space-based astronomy has to resist to an incredible amount of mechanical solicitations during the launch and the travel through Earth's atmosphere to Space and, during its operational lifetime, to an adverse environment with strong temperature gradients, very low external pressure, free residual oxygen of external atmosphere (for low orbit instruments), solar wind and cosmic rays. Till now, space satellites have a very high cost and are limited by technology and in the dimensions. Here is a list of the three main scientific space missions relevant for this PhD work.

2.2.1 Hubble Space Telescope

Hubble Space Telescope (HST) (Figure 2.10) is a space telescope active since 1990. It has a Ritchey-Chretien Cassegrain telescope with a primary mirror diameter of 2.4 meters and a secondary mirror of 0.3 meters, both in ultra-low expansion glass coated in aluminum and protected by a thin layer of magnesium fluoride that also enhances the mirror reflectivity in

[8] `https://hubblesite.org/mission-and-telescope/the-telescope`

the UV range. The mirrors' temperature is kept at 21 °C to avoid warping [9]. Its electronics are powered by the Sun thanks to two solar panels. It orbits around Earth in 95 minutes at an altitude of 540 Km, leading to a temporal discontinuity and some systematics during the observations that must be considered during analysis. HST can observe in the UV-NIR range, from 115 and 1700 nm, thanks to its six scientific instruments available today [10]:

- Wide Field Camera 3 (WFC3), for high resolution spectral and photometrical observations in UV, optical and IR ranges.
- Cosmic Origins Spectrograph (COS), that performs cosmological observations of stars and galaxies in UV range.
- Advanced Camera for Surveys (ACS) for astronomical surveys
- Space Telescope Imaging Spectrograph (STIS), a camera that observes in the UV-NIR range together with a spectrometer
- Fine Guidance Sensors (FGS) for accurate pointing and tracking.

Hubble was repaired by astronauts a few times and some of its instruments have been replaced. This was possible also because of its low orbit position. For example, in 1993 astronauts had to install some corrective devices to compensate the spherical aberration of the telescope, that was miscalculated during the mission realization.

HST mission is one of the most successful space missions ever launched and achieved fundamental contributions in a large variety of different astronomical fields: cosmology, stellar activity, exoplanets, gamma ray burst and galaxy studies.

WFC3 Camera

This advanced camera is one of the most important improvements during HST operating life and replaced WFC2 on May 14th 2009 [11]. The camera can observe between 200 and 1700 nm thanks to two optical/UV CCDs (UVIS) and a HgCdTe array for NIR observations. It can be used both for high resolution images and, thanks to specific grisms, for spectroscopic observations. UVIS Channel CCDs operates at a temperature of 190 K, with a rhomboidal

[9] `https://hubblesite.org/mission-and-telescope/the-telescope`
[10] `https://hubblesite.org/mission-and-telescope/the-telescope`
[11] `https://www.stsci.edu/hst/instrumentation/wfc3`

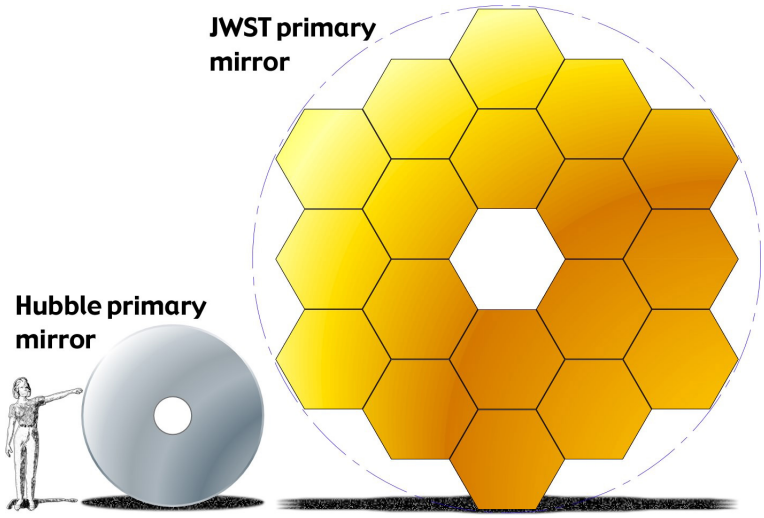

Figure 2.11: Comparison between the JWST and HST primary mirrors [15].

FoV of 162" x 162" and has two filter wheels and a grism for spectroscopic observation between 200 and 800 nm [12].

The IR detector has an operating temperature of 145 K and a rectangular FoV of 136" x 123". Only the central area of 1024 x 1024 pixel is active during observations, while the external non-light sensitive pixels are used as a reference. It operates between 800 and 1700 nm and is equipped with a filter wheel with 15 filters and 2 grisms for both images acquisition and spectroscopic observations [13].

A particular mode of observations, both for UVIS and the IR detector, is the spatial scanning mode (both in forward and reverse mode) in which the stellar spectrum is spread on the detector surface in the direction perpendicular to that of dispersion [14]. This technique helps in achieving higher SNR allowing to obtain much more photons avoiding saturation and reducing the effect of any spatial-related source of noise. This method of observations is fit for high precision observations of very bright objects, especially stars hosting planets. Spatial scanning requires a specific calibration analysis, performed in this work through Iraclis, a software presented in Tsiaras, Waldmann, Rocchetto, et al. 2016.

2.2.2 JWST

[12] https://hst-docs.stsci.edu/wfc3ihb
[13] https://hst-docs.stsci.edu/wfc3ihb
[14] https://hst-docs.stsci.edu/wfc3ihb
[15] https://webb.nasa.gov/content/observatory/ote/mirrors/index.html

James Webb Space Telescope (JWST) is a space NASA satellite specific for near infrared (NIR) and mid-infrared (MIR) observations, launched by ESA's spaceport of Kourou, in French Guyana, on December 25th, 2021. One of its most innovative features is its beryllium primary mirror, made of 18 hexagonal segments, each with a diameter of 1.32 m, for a total diameter of 6.5 m. This mirror is the biggest ever launched in space (a comparison with HST is shown in Figure 2.11) and its beryllium structure makes it 10 times lighter for surface unity than HST mirror, while their hexagonal shape was chosen to minimize the gaps in the total primary mirror and achieve a six-fold symmetry that simplifies the optical adjustments. There are also a secondary mirror with a diameter of 1.4 m and a third mirror to remove astigmatism (JWST is a three mirror anastigmat telescope). Each mirror segment and the secondary mirror are moved by three actuators, plus one to slightly change the mirrors' curvature.

JWST hosts the following four instruments:

- Mid-Infrared Instrument (MIRI). It has both a wide-field camera (FoV of 74" x 113") to acquire images in the 5.6-25.5 μm range and a medium resolution spectrograph to observe between 4.9 and 27.9 μm with a FoV of 6.6' x 7.7' [16]. Its operating temperature is 7 K.

- Near Infrared Spectrograph (NIRSPEC). It observes between 0.6 and 5.3 μm with a FoV of 3.4' x 3.6' [17]. It can acquire spectra of till 100 different objects at the same time thanks to a specific innovative microshutter array (Kutyrev et al. 2008), consisting of four quadrants, each made of 365 x 171 little cells that can each be closed or opened to observe or block the light from single sky sources. Each cell covers a sky area of 0.20" x 0.46".

- Near Infrared Camera (NIRCAM) that observes between 0.6 and 5 μm. It is used for imaging with 28 filters and a total FoV of 9.7 arcmin^2, slitless spectroscopy between 2.4 and 5 μm, grism spectroscopic time monitoring (both with R $\sim$ 1600), photometric observations and coronography thanks to a built-in coronograph [18].

[16] `https://jwst-docs.stsci.edu/jwst-mid-infrared-instrument`
[17] `https://jwst-docs.stsci.edu/jwst-near-infrared-spectrograph`
[18] `https://jwst-docs.stsci.edu/jwst-near-infrared-camera`

- Near Infrared Imager and Slitless Spectrograph (NIRISS) that observes through imaging, slitless spectroscopy and interferometry between 0.6 and 5.0 μm with a FoV of 2.2' x 2.2' [19].

2.2.3 ARIEL

Ariel (Atmospheric Remote-sensing Infrared Exoplanet Large-surveyG. Tinetti et al. 2016) is an ESA's space telescope to be launched in 2029. Its main scientific goal is to analyze the chemical composition and thermal structure of the atmospheres of a large sample ($\sim$ 1000 exoplanets around A-M stars) of transiting and eclipsing exoplanets to study planetary systems' evolution (Edwards, L. Mugnai, et al. 2019). Ariel's telescope is an off-axis Cassegrain telescope (mirrors M1 and M2) with an innovative elliptical mirror (M1) 1.1 x 0.7 m wide, with a third recollimating off-axis parabolic mirror (M3) and other two mirrors to send light to the scientific instruments (M4 and M5). The mirrors are made of Aluminum, specifically EN AW 6061 T651 alloy. The telescope is planned to operate at 55 K. The optical system will send the light to two different instruments:

- Ariel Infrared Spectrometer (AIRS) is an IR low resolution spectrometer (R $\sim$ 30-200) with two observing channels: channel 0 (1.95-3.90 μm) and channel 1 (3.90-7.80 μm). Its operating temperature is below 42 K [20].

- Fine Guidance System (FGS) that has both a guiding/focusing function and a scientific purpose. FSG thanks to specific dichroic sends the light to 4 observing channels: three photometers, FGS-1 (0.6-0.8 μm), FGS-2 (0.8-1.1 μm), VISPhot (0.5-0.6 μm), and a low resolution (R $\geq$ 15) spectrometer, NIRSpec, in the 1.10-1.95 μm range [21]. The guiding observations are planned to occur with a rate of 10 Hz. FGS-1 and FGS-2 are also going to be used as high precision photometers. The total error estimated for all the photometers is less than 50 ppm per hour, allowing high precision measurements of stellar variability also for quiet stars, allowing to model and correct stellar activity in exoplanetary observations [22].

[19] https://jwst-docs.stsci.edu/jwst-near-infrared-imager-and-slitless-spectrograph
[20] https://www.cosmos.esa.int/documents/1783156/3267291/Ariel_RedBook_Nov2020.pdf
[21] https://www.cosmos.esa.int/documents/1783156/3267291/Ariel_RedBook_Nov2020.pdf
[22] https://www.cosmos.esa.int/documents/1783156/3267291/Ariel_RedBook_Nov2020.pdf

Using both AIRS and FSG will allow us to have simultaneous multiband optical-NIR photometry and IR low resolution spectra of the observed targets, enhancing our possibilities of modeling and correcting stellar variability to extract planetary signals with high precision.

2.3 Images Analysis

Astronomical raw images are usually affected by systematics due to the following effects:

- atmospheric seeing
- thermal and electronic noise of the detector
- non uniformity of the light diffusion inside the telescope that usually leads to an inefficient illumination of the detector edges
- shot noise

Shot noise is the poissonian noise of stellar and sky background signals and, if the images are well calibrated, it is the main source of error in astronomical observations. In order to reduce its impact in the measure, it is necessary to achieve high SNR with as long exposures as possible, compatibly with the stability of the telescope tracking, the risk of saturating the detector and the necessary time resolution of the observations.

2.3.1 Atmospheric seeing

Atmospheric seeing is an external constraint for photometric observations quality. It is caused by the alterations that affect stellar light as it passes through our atmosphere. In our case we have three fundamental effects to consider: atmospheric scintillation, blue light reduction and the increase of the detector area corresponding to a specific star image. Atmospheric scintillation is due to air turbulence, because the mixing of air layers with different temperatures and densities lead to a change in velocity and focus of the incoming stellar light (Osborn et al. 2015). This effect is particularly important for small telescopes like the ones used in this work. Another important effect of our atmosphere is the dispersion of light through Rayleigh scattering. This effect is wavelength dependent and much stronger at shorter wavelength, so the blue part of the stellar spectrum is dimmed with respect to the longer wavelengths. If we are interested in studying the chromatic signals of a star,

this effect can have a huge impact in our observations. Rayleigh scattering can affect our observations also spreading around the sky the light of other sources, mainly the artificial lights and the light of the Moon, causing an increase of the background noise of our images and a reduction of SNR of our data. Artificial lights have stronger effect in yellow and red bands, while the moonlight affects especially the blue band. Finally, our atmosphere causes an increase of the size of the image of a star (point spread function or PSF) in our detector that can reduce the SNR of faint stars light and mix the signals from different objects with small angular separation in the sky. The noise due to these mechanisms can be reduced choosing telescopes in places with a very dark sky, far from cities, and choosing, if possible, to observe when the moonlight is low and the weather conditions are stable, with obviously no clouds, but also low humidity and low winds in high atmosphere.

2.3.2 Images calibration

In order to correct the instrumental systematics, we need to acquire not only the images of the stellar targets, but also specific calibration frames: dark and flatfield images. Dark images collect all the information about the electronic noise (bias noise) and the thermal noise due to the poissonian fluctuation of the detector dark current, due to thermal electrons that are collected and mistook as signal. Dark images are acquired measuring the signal from the detector with the camera shutter closed and with the same integration time as scientific images. Flatfield images instead measure the illumination difference between the sensor edges and center due to the geometry of the optical system. In order to acquire flatfield images, it is necessary to observe a uniform light (the sky background at dawn or dusk or uniform diffused light on a white screen) to measure the non uniformity of the effective observed signal. In order to calibrate the raw images, we use the median dark and flatfield images, obtained calculating the median signal for each pixel both for dark frames and flatfield frames. We use the median signal and not the mean one to avoid non-statistical contribution, like that of cosmic rays. Flatfield images $\mathrm{Ff_i}$ are affected by thermal and electronic noise too, so we must calibrate them, subtracting from them the dark images signal $\mathrm{D_i}$. The final equation to calibrate the raw images $\mathrm{S_{0i}}$ and obtain the calibrated ones $\mathrm{S_i}$ is then:

$$S_i = (S_{0i} - D_i)/(Ff_i - D_i) \tag{2.3.1}$$

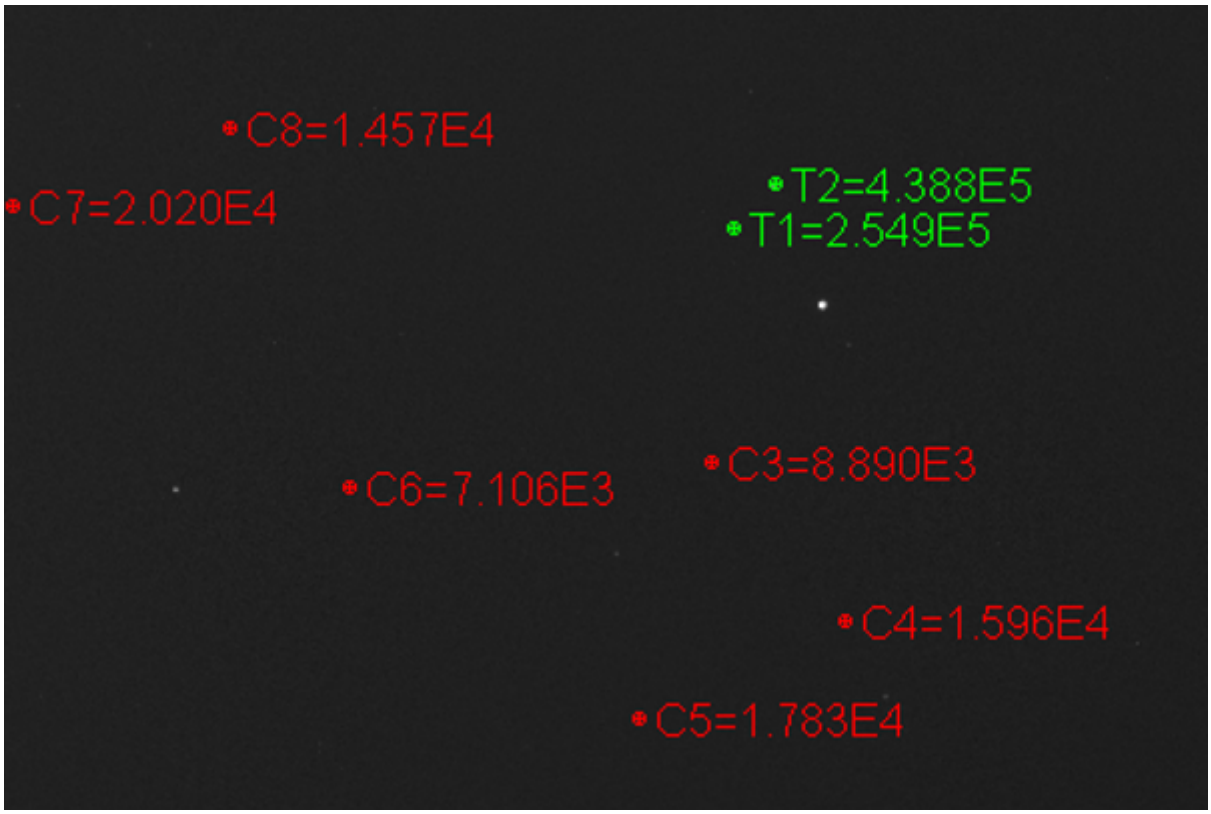

Figure 2.12: FoV of V1298 Tau as seen from OPC telescope. The image shows V1298 Tau, the target star T1 (green) and the reference stars (red circles) used in the observations of this target. T2 star (green) is a discarded reference star, not used in the analysis because it was variable.

In this analysis this calibration procedure is performed using a photometric analysis software, AstroImageJ, developed by TESS collaboration (K. A. Collins, Kielkopf, et al. 2017).

2.3.3 Differential Photometry

During transits or stellar variability observations, it is not required to measure the stellar flux, because we are only interested in the occurring changes with respect to its "normal" condition. This allows us to use a method called "differential photometry" in which we measure how the flux of the target star changes with respect to some carefully chosen reference stars (see for example Figure 2.12). This method greatly reduces the effect on our measures of the atmospheric seeing as the star move across the sky, because it affects the stellar light in almost the same amount for every object in the FoV and so it is removed when we analyze the relative differences between the stars. Given a set of N reference stars,

it is possible to measure the relative flux light-curve F_{rel} of the target star using:

$$F_{rel} = \frac{F_*}{\sum_{i=1}^{N} F_i} \tag{2.3.2}$$

where F_* is the absolute flux of the target star and F_i is the absolute flux of the reference star i.

Choosing the reference stars is a critical point of the procedure, because, in order to minimize the error, we must find a difficult balance between the number of reference stars, their photometrical stability in every band observed and their SNR. We must also avoid choosing stars with a large difference of spectral class and magnitude in any observed photometrical band with respect to the target because this can lead both to risk of saturation or low SNR (and major impact of the sky shot noise) for either the target or the reference stars. Furthermore, it is also important to avoid choosing stars far from the target because residual flatfield effects can become relevant, because the slight difference in the sky path of the stars can lead to a chromatic difference in the measured fluxes (important for large FoV) and finally because we risk not to have always all the star images on the detector if the telescope tracking is not stable enough during the observations. In order to evaluate the stability of the reference stars, we can apply differential photometry to each of them with respect to the others using:

$$F_{rel} = \frac{F_j}{\sum_{i=1, i\neq j}^{N} F_i} \tag{2.3.3}$$

where j is the candidate reference star that we want to compare with the others. In this work, we applied this method using AstroImageJ, a software specific for differential photometry analysis (K. A. Collins, Kielkopf, et al. 2017).

Chapter 3

V1298 Tau: Multiband Photometry analysis

3.1 Introduction

In order to remove the effects of the spots on our data, we need to know their properties, positions and temperature. For this reason, in the following, we will develop a method to model the spot configuration in active stars based on a multiband photometry analysis.
Using the photometric light curve to model the spots leads to the so-called inverse light curve inversion problem (Luger et al. 2021): we can't see directly the spots, so we have many geometrical degeneracies in our models. For example, it is difficult to distinguish spots on each specific hemisphere of the star and we have a degeneracy between temperature, radius and latitude of the spots. For isolated observations, we have also a degeneracy between the latitude and longitude of the spots that can be broken by observing the star multiple times during its rotation. We aim to break these degeneracies by monitoring the star for a few days through different photometric bands at the same time. We chose to use multiband photometrical observations because we want to take advantage of the chromaticity of the spot contribution to the stellar observation: we expect in fact to have a different ratio between spots flux and stellar flux at different wavelengths because they correspond in first approximation to two blackbodies with different temperatures. The difference between the spots and stellar flux should decrease at longer wavelengths, as far as in the IR band: for example, a star with $T_\odot$ and a spot with a filling factor of 1% and a ΔT of 1250 K will present variations of $\frac{\Delta FU}{FU} = 9 \times 10^{-3}$ in the optical band U and $\frac{\Delta FK}{FK} = 3 \times 10^{-3}$ in the IR band K, respectively (Ballerini et al. 2012).

Table 3.1: V1298 Tau properties (David, Cody, et al. 2019; David, Petigura, et al. 2019).

Parameter	**Value**
$M_*(M_\odot)$	1.101 ± 0.005
$R_*(R_\odot)$	1.34 ± 0.06
Age (Myr)	23 ± 4
P_{rot} (d)	2.87 ± 0.02
T (K)	4970 ± 120
v sin i ($km\,s^{-1}$)	23 ± 2
Distance (pc)	108.5 ± 0.7
Spectral Type	$K0 - K1.5$
V mag	10.12

Through simultaneous multi-band photometric observations, we aim to constrain the temperature difference between the stellar surface (whose temperature is known from literature) and the spots. In this chapter, we used multiband photometric ground-based observations to model the spots of a very interesting young stellar object (YSO), V1298 Tau, that we will describe in Section 2. In Section 3 we will describe the methodology of our observations and in Section 4 our retrieval method, while in Section 5 we will discuss the validation of our model using solar data. Our final results about V1298 Tau photometric analysis will be discussed in Section 6.

3.2 Stellar target: V1298 Tau

V1298 Tau is a K0-K1.5 young star (∼20 Myr) with a mass about $1.1M_\odot$ located at ∼ 108 pc from Earth. It is an ultra-fast rotator with a rotational period of less than 3 days (David, Cody, et al. 2019). In Table 3.1 we show the properties of V1298 Tau from the literature.

V1298 Tau is one of the youngest stars known to host more than one transiting planet (Suárez Mascareño et al. 2021), not a very common occurrence (Latham et al. 2011): three of them are confirmed (V1298 Tau b, c and d) and another one is yet to be confirmed (V1298 Tau e). Confirming the presence of planet e and the properties of this planetary system

is extremely difficult because of the long period of this planet and because of the strong activity of the star that interferes with our observations (Blunt et al. 2023), so it is needed to model this activity of V1298 Tau in order to correct its related noise.

The star and its planets have already been studied both through photometry (for example by TESS, Feinstein et al. 2022) and spectroscopic observations (through radial velocities, for example by HARPS-N, Suárez Mascareño et al. 2021).

We know also from previous studies, such as the spectral cross-correlation function (CCF) analysis from Di Maio, Petralia, et al. 2023, that the star shows large spots at high latitudes (> 60 deg) and smaller spots at low latitudes (> 40 deg), but the relation between the spectral distortion due to stellar activity and the photometric flux variations of the star is not clear and the spectral analysis of the spots has been based on the hypothesis of not emitting spots (i.e. black spots, surface regions with temperature of 0 K) that is not physically correct. In this chapter, we are interested in modelling the activity of the star due to spots on the stellar surface using multiband photometric data to better constrain their temperature and geometric parameters.

Table 3.2: Journal of observation for V1298 Tau.

Time	**Bands**	
21-25/02/2021	OPC	B-V-R
23-25/02/2021	GAL	r'-H alpha
11-15/12/2021	OPC	B-V-R
13-15/12/2021	REM	J
21-23/02/2022	OPC	B-V-R-I
28/02/2022-01-02/03/2022	OPC	B-V-R-I
01-04/09/2022	GAL	g'-r'-z'-H alpha
27/08/2022-03/09/2002	REM	g'-r'-i'-z'-J

3.3 Observations and data analysis

We have organized multiband photometric observing campaigns from three different observatories:

- Osservatorio Polifunzionale del Chianti (OPC) with a Ritchey-Chretien telescope with the following characteristics: 80 cm diameter, f/8, field of view (FoV) of $\sim$ 20' x 20' and Johnson filters B-V-R-I.
- Gal-Hassin Observatory with a Ritchey-Chretien telescope with a diameter of 40 cm and Sloan filters u', g', r', i' and z'.
- REM telescope at La Silla Observatory (Chile), a Ritchey-Chretien telescope with a diameter of 60 cm, capable of simultaneous observations in optical bands, through ROS2 detector (Sloan filters g', r', z' and i'), and in IR bands thanks to REMIR detector (Sloan z filter and standard J, H and Ks filters).

Each observatory campaign spanned between 3 and 5 days, i.e. between 1 and slightly less than 2 rotational periods (about 2.8 days) of the star (see Table 3.2). The star's location near the ecliptic during the period from October to March poses challenges in coordinating observations from different telescopes for this target. Thus, in addition to the usual constraints arising from potential bad weather conditions, we also had to account for the lunar interference by avoiding days when the Moon passed near the target within a 60 deg range to avoid the noise due to the moonlight scattering. Finally, to model the stellar photosphere, we avoided all the days with planetary transits for this target. In conclusion, we observed the star in the following different periods: in February 2021, December 2021 and February 2022 from OPC, in December 2021 and September 2022 from REM and in February 2021 and September 2022 from Gal-Hassin. We evaluated the best observing runs, selecting only observed data sets with SNR $>$ 20. This criterion leads to the selection of only OPC data, because these are the observations with the best SNR thanks to the telescope large diameter and FoV. Data from REM and Gal-Hassin observatories are shown in APPENDIX B. Finally, to avoid problems due to possible spot evolution we limited our analysis to maximum 3 days (see Section 4), obtaining these final datasets:

- 21-22-23, 22-23-24 and 23-24-25 (February 2021) from with B, V and R bands, between 40 and 50 images per night in each filter
- 12-13-14 and 13-14-15 (December 2021) with B, V and R bands, between 50 and 70 images per night in each filter
- 11-12-13 (December 2021) with V and R bands, about 50 images per night in each filter
- 21-22-23 (February 2022) with V, R and I bands, between 45 and 70 images per night in each filter

Table 3.3: Flux variations amplitudes measured analyzing V1298 Tau data in different photometric bands, obtained fitting the data with a sinusoidal function and an offset.

Observing Run	Filter	Flux Variation
02/2021	B	$0.0515^{+0.0018}_{-0.0017}$
02/2021	V	$0.0425^{+0.0013}_{-0.0013}$
02/2021	R	$0.0356^{+0.0013}_{-0.0012}$
12/2021	B	$0.084^{+0.002}_{-0.002}$
12/2021	V	$0.066^{+0.002}_{-0.002}$
12/2021	R	$0.0600^{+0.0018}_{-0.0019}$
02/2022	V	$0.096^{+0.002}_{-0.003}$
02/2022	R	$0.1194^{+0.0019}_{-0.0019}$
02/2022	I	$0.061^{+0.0018}_{-0.0019}$

We calibrated and analyzed the images using AstroImageJ (a software developed by TESS collaboration, K. A. Collins, Kielkopf, et al. 2017) and we applied the so-called differential photometry method: we did not measure the absolute photometry of the target star, but its variability with respect to some carefully chosen stable check stars in the same field of view of V1298 Tau, used as reference. The choice of these check stars required a delicate compromise between the necessity of the highest number of them and the requirement of stability and comparable magnitude with respect to the target. In the FoV of the telescope

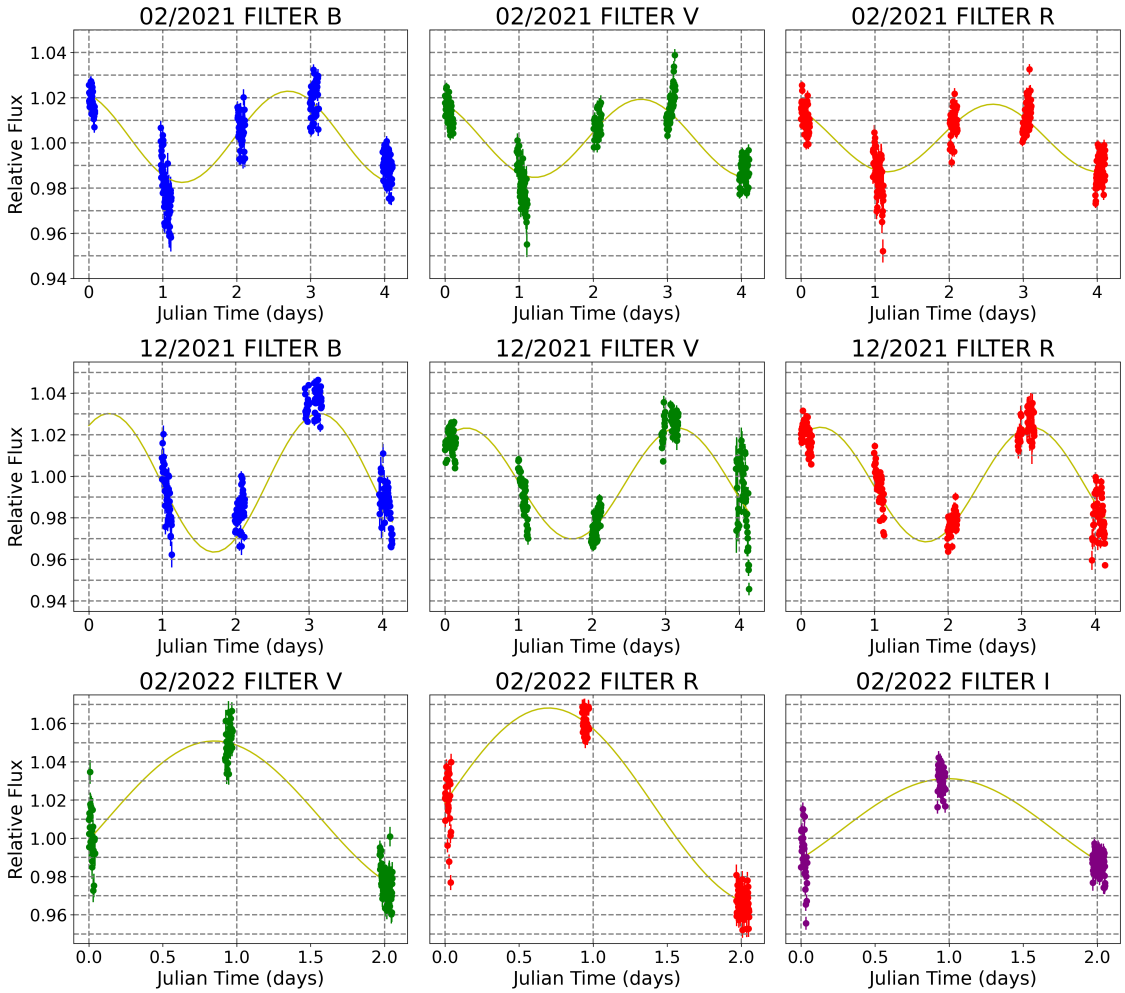

Figure 3.1: Data observed from OPC in B, V, R bands in February 2021 and December 2021 and in V, R and I bands in February 2022. The plotted line is an estimation of the flux variation of the star obtained by fitting the data by using a sinusoidal function with an offset. For the observations of February 2022 and for the first day of observation of December 2021, B band data were discarded because they had a signal-to-noise ratio (SNR) < 20.

(20' x 20') around the star there are only a few stars and most of them were saturated, very faint or variable, so in the end we found only 6 stable reference stars, shown in Figure 2.12 in Chapter 2. It should be noted that we used the same reference stars for all the datasets. Using this procedure we obtained the light-curve of V1298 Tau in the selected photometric bands shown in Figure 3.1. To retrieve the flux variation amplitude of the star, we employed a sinusoidal function to fit the data, fixing the rotational period to 2.87 days (David, Cody, et al. 2019), also incorporating an offset in observations (see Fig. 3.1). This function

Table 3.4: Priors on spot parameters of MultiNest for our retrieval procedure to model V1298 activity. Spot temperature's prior is set with a maximum temperature exceeding the unspotted surface one to include the possibility of retrieving a facula instead of a spot.

Parameter	**Priors**
Jitter	1e-4,1e-1
Scale Factor	0.5-5
Temperature	3000-5500 K
Latitude	0-90 deg
Longitude	-180-180 deg
Radius	0-1.0 $R_\star$

feeds the bayesian framework *Multinest v3.10* (Feroz, Hobson, and Bridges 2009) to derive parameters best-fit values and errors throughout the python package *PyMultiNest v2.12* (Buchner et al. 2014) and with the following likelihood:

$$\ln p(y_n, t_n, \sigma, \theta) = -1/2 \sum_n \left[(y_n - F(t_n, \theta))^2 / \sigma^2 + \ln 2\pi\sigma^2 \right] \tag{3.3.1}$$

where y_n and t_n are, respectively, data fluxes and times, $\sigma = \sqrt{\sigma_n^2 + \sigma_j^2}$ with σ_n as data errors and σ_j as white noise jitter term, introduced to account for unknown source of errors. The algorithm was set to use 1000 live points, leaving all other parameters to their default values.

This analysis allowed to estimate the flux variations (see Table 3.3) of the star and verify the coherence in each observation.

Therefore, from Figures 3.1 we observed variability in the amplitude of the sinusoidal fit, which diminishes at longer wavelengths, consistent with the assumption of a spot-dominated star. The results of this analysis are summarized in Table 3.3.

3.4 Forward Model and Retrieval

We modelled the spot properties (latitude, longitude, radius and the temperature of the spots) following the approach of Cracchiolo, G. Micela, Morello, et al. 2021 and Cracchiolo, G. Micela, and Peres 2021 and we imposed some assumptions:

- Spots corotating with the stellar surface
- Not evolving spots during a rotational period of the star
- Approximation of circular spots projected on the stellar surface
- Same temperature for all the spots

With these hypotheses, we aimed to analyze flux variations of the star as generated by the luminosity contrast between the spots and the photosphere. Since the star has an inclination of nearly 90 deg, as we can see by combining the v sin i value of the star with its rotational period (see table 3.1), we had a degeneracy in latitude because we could not distinguish the hemisphere in which the specific spot was located. We removed instead the degeneracy in longitude for the spots thanks to the rotation of the star, so we could retrieve their longitude from the time variations of the stellar flux. We chose to analyze datasets of 3 consecutive days (about a rotational period of the star) in order to avoid relevant contributions from spots evolution. In order to build our forward model for the retrieval procedure, we divided the star into concentric rings, with a finer division near the limb of the stellar disk to better account for the effect of limb darkening. We also took into account the limb-darkening effect of the star with a linear approximation. We derived the limb darkening coefficients for each possible temperature of the stellar surface (and spots) and different wavelengths using ExoTETHyS package (Morello et al. 2020).

To retrieve the spots properties from our data we used the minimization algorithm MultiNest whose priors are shown in Table 3.4, setting 3000 live points to achieve high precision in the retrieval. It should be noted that spot temperature's prior is set with a maximum temperature exceeding that estimated for the unspotted surface to include the possibility of retrieving a facula instead of a spot.

In order to fit the data, our forward model simulates the light curve of the star for each spot configuration tested, calculating at each temporal step the portion of the spotted and unspotted stellar surface visible from Earth. Using these informations it estimates the contributions to the total stellar flux of the spotted and of the unspotted visible surface of the star using the method developed in Cracchiolo, G. Micela, and Peres 2021, then it rotates the star of a given time step and uses this loop to calculate the light-curve of the star. To estimate the fluxes of spots and stellar surface in the chosen range of temperatures

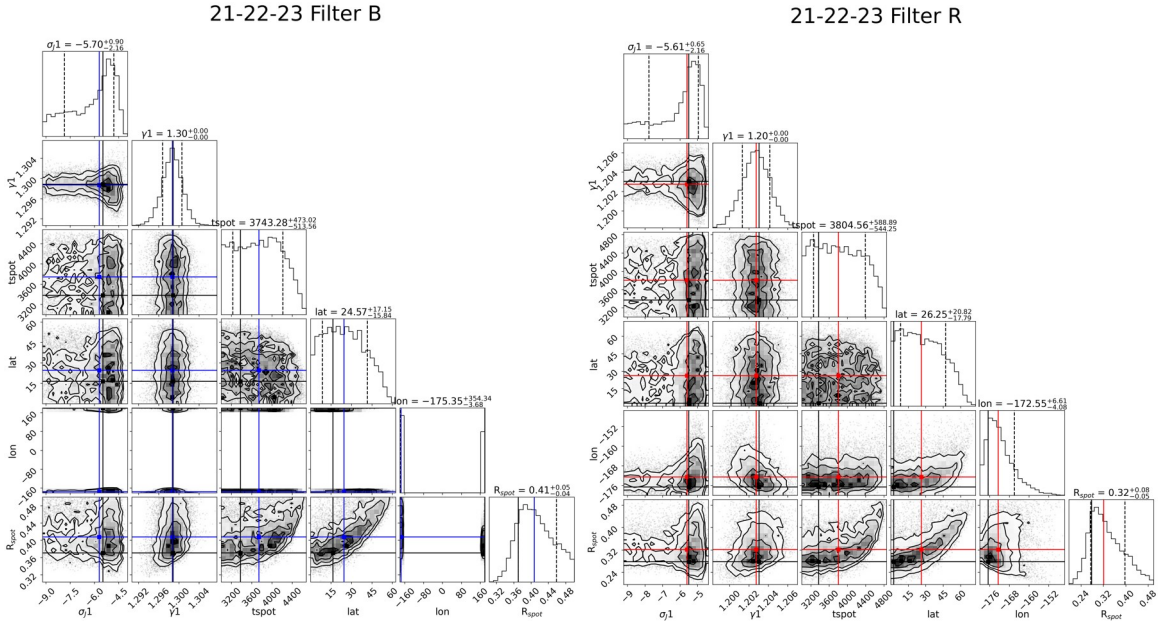

Figure 3.2: Comparison of the retrieval posteriors of spots for V1298 Tau, obtained by OPC observations on 21-22-23/02/2021 through a separate analysis for data in B (left) and R (right) photometric bands. Blue lines (for right image) and red lines (for left image) mark median values, while black lines mark maximum probability (MAP) values for both images.

(see Table 3.4) we used Phoenix models (Claret, Hauschildt, and Witte 2012; Husser et al. 2013) and we applied the limb darkening coefficients derived by ExoTETHyS (Morello et al. 2020). Finally, MultiNest calculates the fit and Bayesian evidence to estimate the goodness of the fit and in the end the parameters of our model.

3.5 Results and discussion

3.5.1 One band vs Multiband approach

Figure 3.2 shows some examples of results obtained from the analysis of single photometric band. It is clear that a degeneracy exists among the latitude of the spots, their radius, and their temperature, as we observe only the emission contrast between the spots and the stellar surface. These degeneracies lead to high uncertainties in spots parameters: in particular, we found a temperature error bar of several hundreds of K, while the latitude spans between 9 and 40-45 deg. By assuming that the stellar spots and the photosphere emit as star surfaces at different temperatures, the emission contrast should change at different wavelengths, producing a different flux variation across different spectral bands.

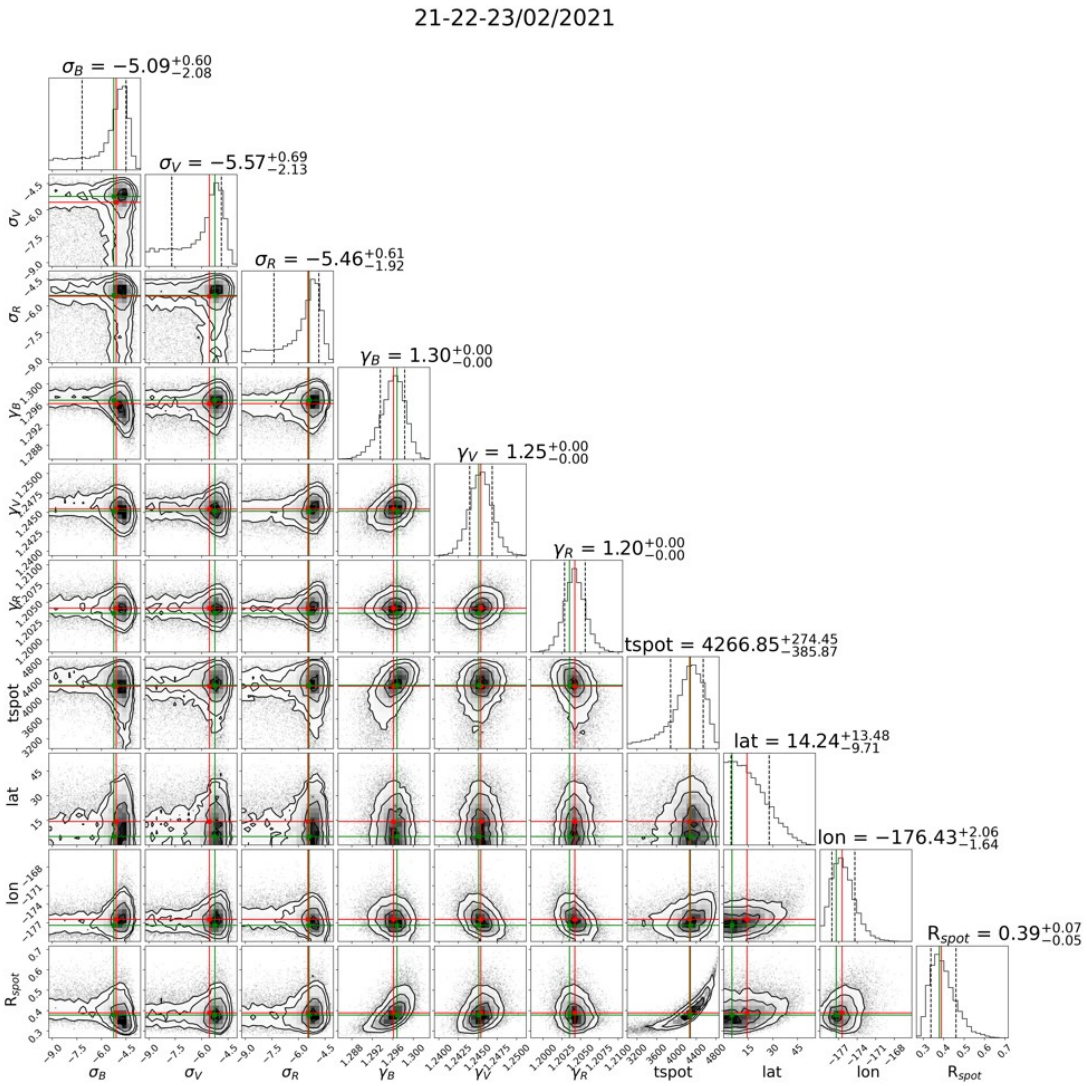

Figure 3.3: Corner plot obtained by the retrieval procedure for the multiband photometric data acquired by OPC in the first run of observation, specifically on February 23-25th, 2021. $\sigma_{\rm i}$ are the jitter parameters and $\gamma_{\rm i}$ are the offsets of the forward model used in the retrieval for each band observed (B, V and R). Red lines mark median values, while green lines mark MAP values.

Consequently, through the analysis of simultaneous multiband photometric observations, we could be able to constrain the spots' temperature, thereby breaking the degeneracy between the radius, temperature and latitude of the spots. Therefore, we performed a new retrieval procedure imposing for each 3 days sequence that all the bands share the same spot parameters, but different flux scales. We applied our model assuming the simultaneous presence of one, two, three, or four spots on the entire stellar surface. However, due to our

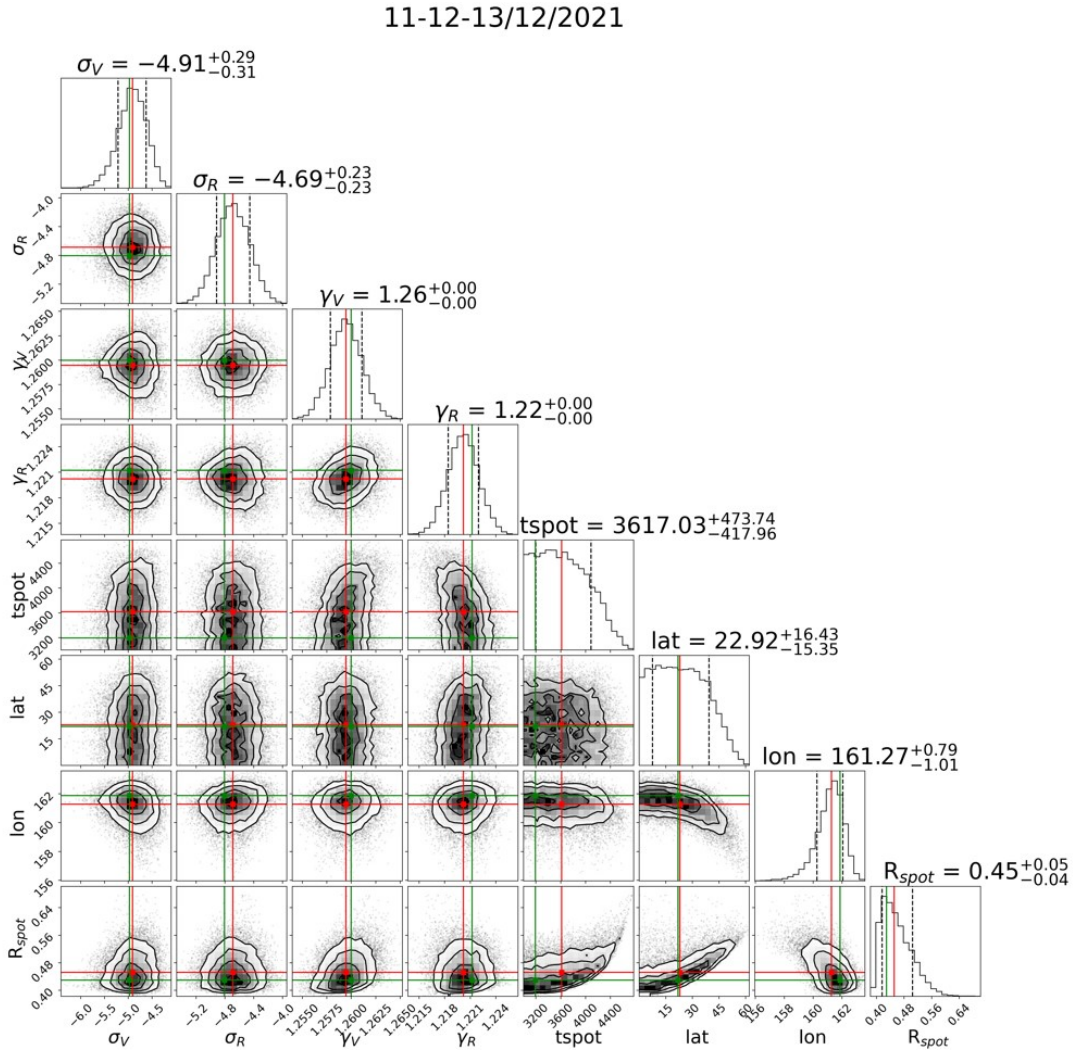

Figure 3.4: Same ad for Figure 3.3, but in the case of V and R bands on December 11-12-13rd, 2021.

temporal coverage and sampling, each model with more than one spot resulted in overfitting of our data, so we chose to model only one spot per dataset. Examples of the resulting corner plots are shown in Figure 3.3, 3.4 and 3.5 and the retrieved spot temperatures are shown in Table 3.5. In comparison to the single band analysis, we found a tighter interval for spots temperature, with a decrease of the spot temperature uncertainty by a factor of two and a strong reduction of latitude uncertainties to only few degrees. We also obtained a reduction of the radii uncertainties of an order of magnitude. It should be noted that with multiband analysis the degeneracy between latitude and radius is removed, while the

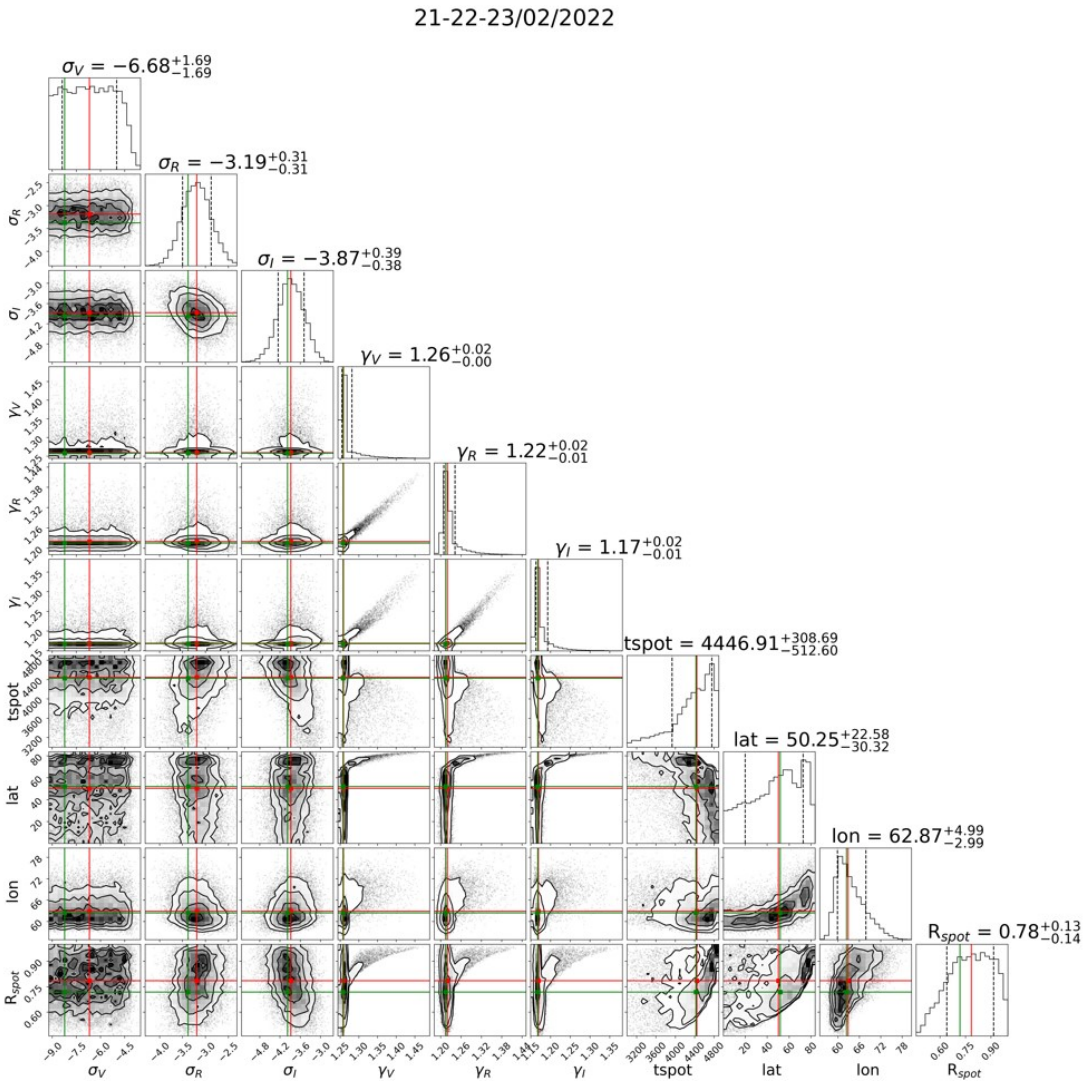

Figure 3.5: Same ad for Figure 3.3, but in the case of V, R and I bands on February 21-22-23rd, 2021.

degeneracy between latitude and spot's temperature is greatly reduced.

Finally, we checked for the consistency of the spot positions and geometry along each observing run, plotting all the configurations of the spots with weights (of MultiNest algorithm) over the 0.85 quantiles. The above selection guarantees that only high likelihood values are selected and, consequently, shown.

For each observing run, we found a good compatibility of the radius and position of the retrieved spot, even if with some hints of evolution on a timescale similar to the rotational period of the star as we can see comparing the retrieved spots in different 3 days sequences:

in each one we had imposed the absence of evolution for the spot, but we can see how the same spot changes between different sequences of days in the same observing run. An example is shown in Fig. 3.6 for the best observing run (February 2021) results. The spot configurations here shown correspond to the same time of the star rotation as obtained using data by each 3 days-sequence of this observing run. We found also compatible spot temperature values within a given period, but only a small compatibility between different observing periods with a slight overlapping between 4079 and 4090 K, as shown in Table 3.6. It is quite evident a decrease of the retrieved spots temperature between the first period of observations and the other two. A possible scenario is that in our approach we are measuring an effective temperature of the inhomogeneities of the stellar surface, which are more complex than simple spots and what we retrieve is in fact the whole active region of the star with properties that result from the average effect of little surface features (like spots and faculae). Then our effective temperature should be sensitive, for example, to a change in the ratio between the filling factor of faculae and spots on the star.

Table 3.5: Spot temperature range estimates for each independent set of observations in the hypothesis of one spot. For the set marked with "*" we used only V and R data because B data had a low SNR, while for the same reason we used V, R and I data for the last set (marked with "**").

Dates	**Bands**	**Tspot (K)**
21-22-23/02/2021	B-R-V	4267^{+274}_{-386}
22-23-24/02/2021	B-R-V	4428^{+247}_{-349}
23-24-25/02/2021	B-R-V	4079^{+463}_{-593}
11-12-13/12/2021*	R-V	3617^{+473}_{-417}
12-13-14/12/2021	B-R-V	4167^{+272}_{-327}
13-14-15/12/2021	B-R-V	3854^{+287}_{-451}
21-22-23/02/2022**	R-V-I	4447^{+308}_{-512}

Table 3.6: Spot temperature range estimates for each observing run in the 1 spot hypothesis. For observing runs longer than 3 days, we took the common range of the various 3 days-sequences of that run.

Periods	**Tspot (K)**
21-25/02/2021	4079-4541 K
11-15/12/2021	3840-4090 K
21-23/02/2022	3935-4755 K

3.5.2 Interpretation of "spot temperature"

In order to verify the hypothesis that our analysis retrieves the properties of the complex dominant active region, we analyzed the spectroscopic activity indicators of V1298 Tau to get some clues about a possible change of the stellar activity. In particular, we analyzed HARPS-N (Cosentino et al. 2012) data acquired in a span of 4 years (2018-2023) using the method described in Di Maio, Argiroffi, et al. 2020, looking for temporal variability of activity indicators such as CaII H and CaII K (Figure 3.7) and Hα (Figure 3.8). Vertical lines in the plots mark the periods of our observations. In Figure 3.8 we can see how the measured intensity increases leading this line from absorption to emission, while in Figure 3.7 we can see an increase in the scatter of CaII H and K line intensities along the time. These effects point towards a change in activity between the first and the second period of observations, with an increase of the ratio between Hα and CaII H + CaII K line intensities (Fig. 3.9). Our photometric observations support that the reason for this evolution could be a change in the ratio of stellar surface covered by spots and faculae.

3.5.3 Validation of the model: solar case

For further validation, we tested the model using Sun observations, where photometric data can be directly compared with spatially resolved active regions present on its surface. We used the multiband photometric data from VIRGO-SPM (Chaplin and Appourchaux 1999), the three channels sun photometer (SPM) of the experiment VIRGO (Fröhlich et al. 1997, Variability of solar IRradiance and Gravity Oscillations), an experiment of the space mission SOHO (Domingo, Fleck, and Poland 1995, Solar and Heliospheric Observatory). VIRGO-SPM observed the Sun from April 11th 1996 until March 30th 2014 with an image every 60

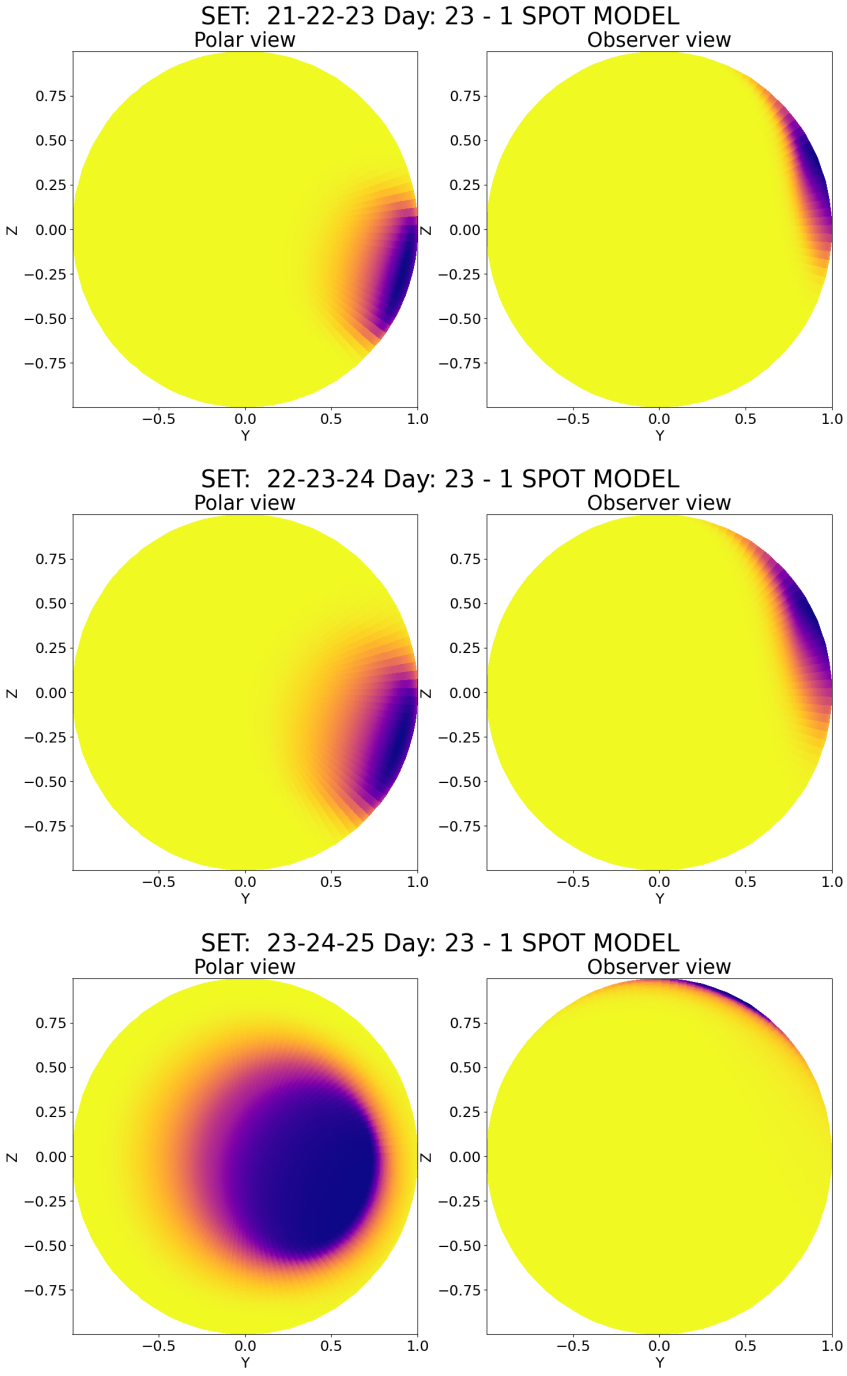

Figure 3.6: V1298 Tau spots positions of the 3 observing sets of February 2021, given by the distribution of solutions of MultiNest retrieval. Each image shows the star as seen on the same day, February 23rd, 2021. The spots are shown both from a polar view (on the right) and from the equator, i.e. from Earth (on the left).

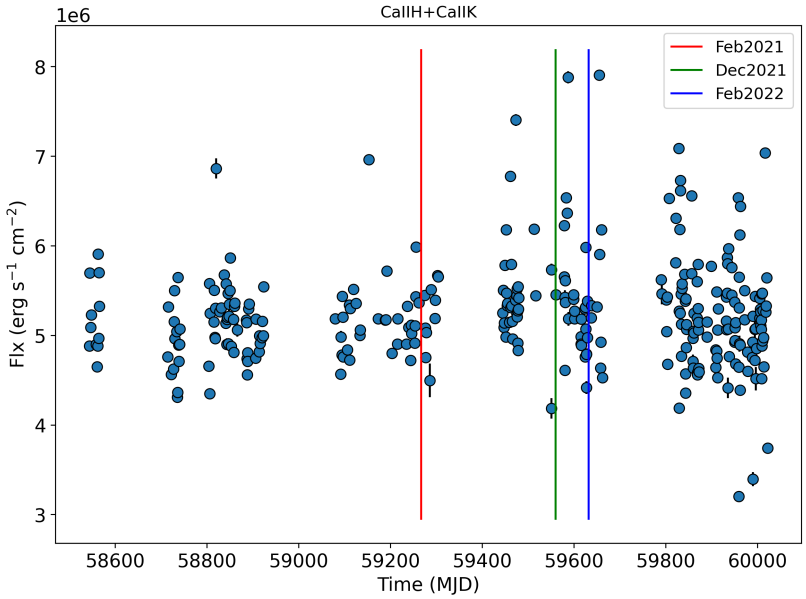

Figure 3.7: CaIIH + CaIIK values obtained by HARPS-N for V1298 Tau. The colored lines correspond to our periods of observations: February 2021, December 2021 and February 2022.

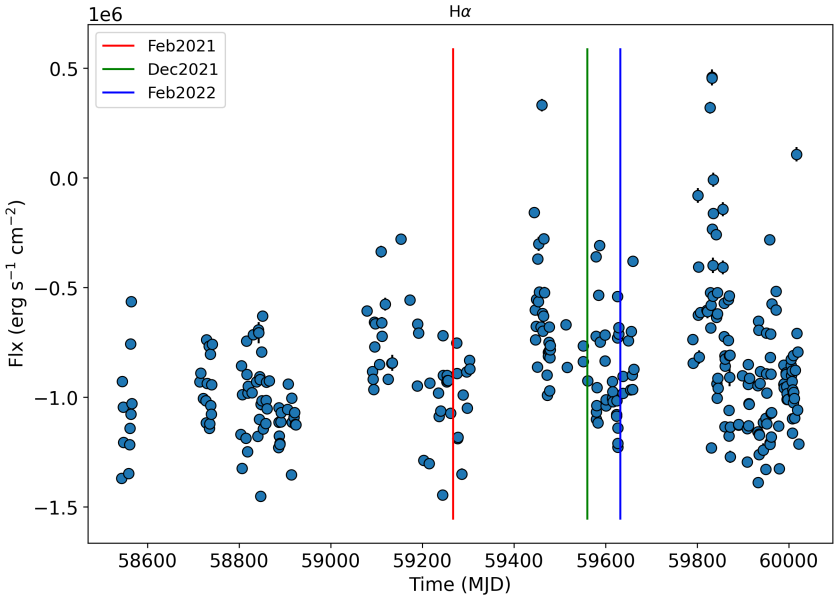

Figure 3.8: H alpha values obtained by HARPS-N for V1298 Tau. The colored lines correspond to our periods of observations: February 2021, December 2021 and February 2022.

seconds in three narrow bands at 402, 500, and 862 nm with a bandwidth of about 5 nm.

In particular, we focused on the rotational period starting from 12/30/2013, during which

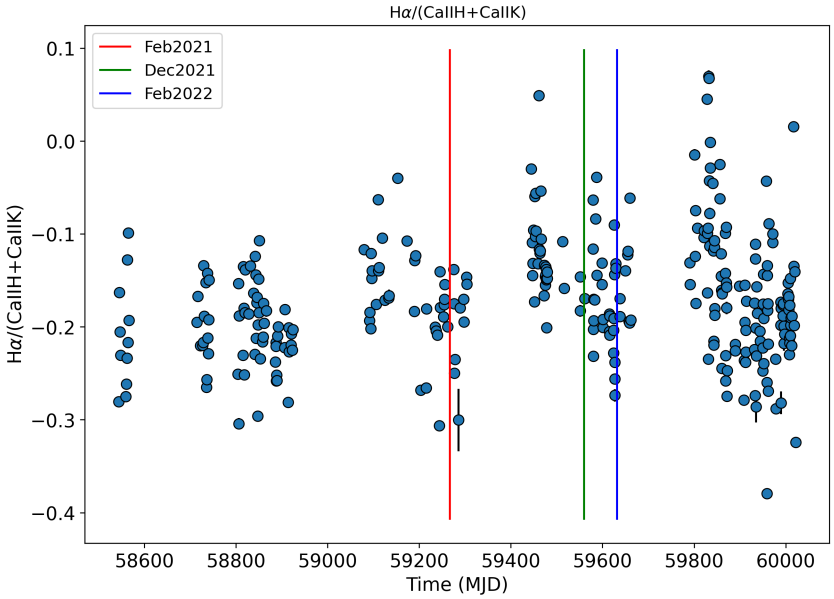

Figure 3.9: Ratio of Hα/(CaIIH + CaIIK) values obtained by HARPS-N spectrometer for V1298 Tau. The colored lines correspond to our periods of observations: February 2021, December 2021 and February 2022.

the Sun exhibited a higher level of activity. This was evident through the presence of two large active regions separated by approximately 180 degrees in longitude. We analyzed the most active one fitting half period. Subsequently, we rebinned the data to obtain two data points per day (which is reasonable for observations of a long-period star like our Sun), and then applied our method to all three bands simultaneously, assuming one dominant spot. As prior for the retrieval model we imposed a spot radius between 0 and 0.25 and a spot temperature between 3800 and 5900 K to allow also the possibility of retrieval of faculae instead of spots. The fit results for the first half-period analyzed are shown in Figure 3.10. Figure 3.11 shows the comparison between the simulation of the retrieved solar active region (left panel) and the actual contemporary image of the Sun (right panel), with its real spots, taken from Helioseismic and Magnetic Imager (Schou et al. 2012, HMI), while the bottom panel of the figure shows how our model fit the observed solar data in the three photometric bands.

The comparison between the two upper panels of Figure 3.11 shows that we were able to constrain with great precision the position of the active regions of the Sun breaking the degeneracy between their latitude and radius, while Figure 3.10 shows that the degeneracy

between active region's latitude and temperature is also small and confined to a narrow parameters range. Moreover, we found that the retrieved radius encloses not only the main big spot but also all the smaller spots, penumbra areas, faculae and some of the photosphere inside and around them, leading to very little contrast between the retrieved active region's temperature and the photospheric temperature, confirming our initial hypothesis that our procedure retrieves not the real spots' temperature, but the average temperature of the entire active region of the star.

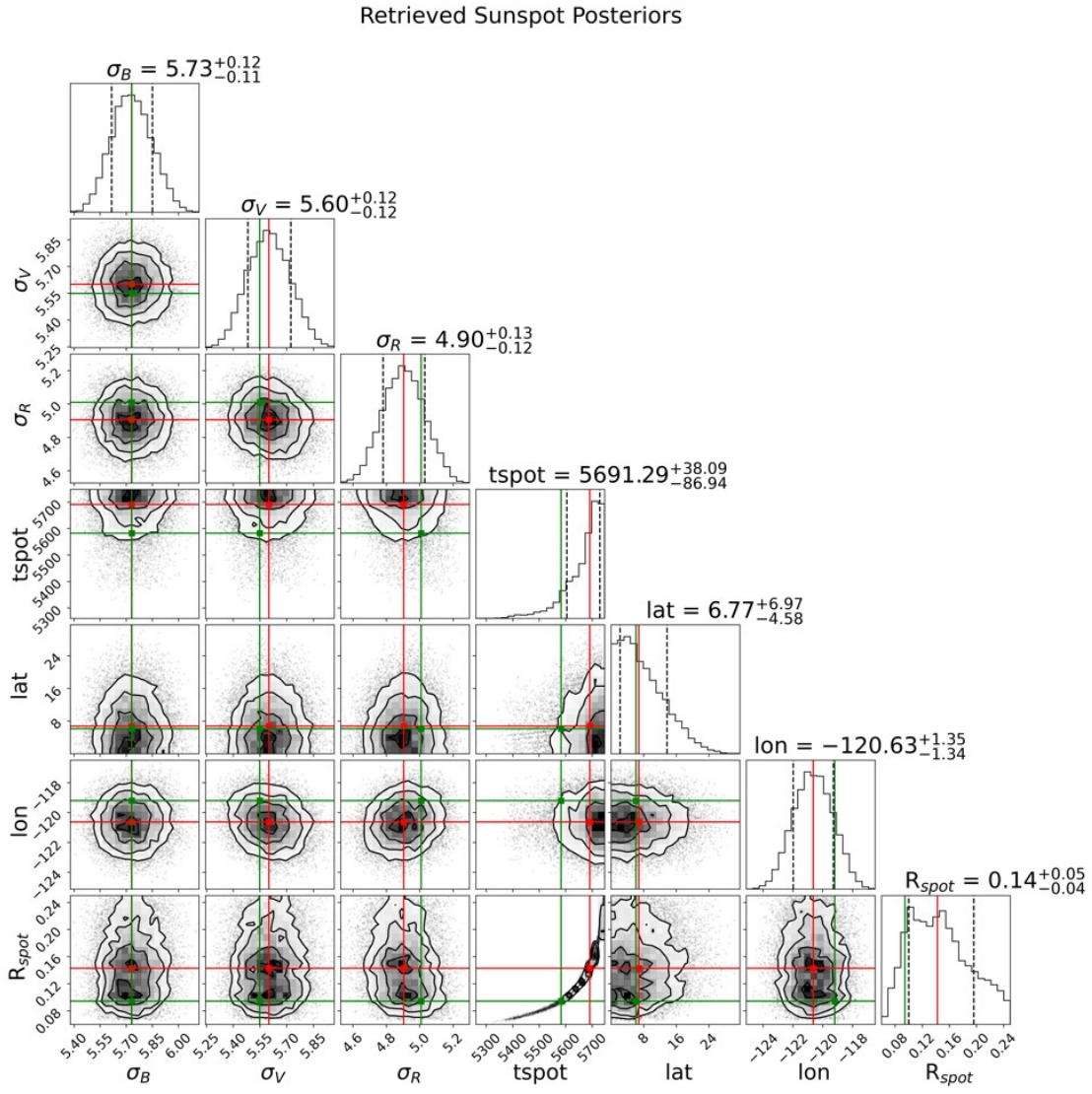

Figure 3.10: Posteriors of the retrieval procedure for the analysis of the active region properties on the Sun during the first half of the rotational period starting on 12/30/2013. Green lines mark MAP values, while red lines mark median values.

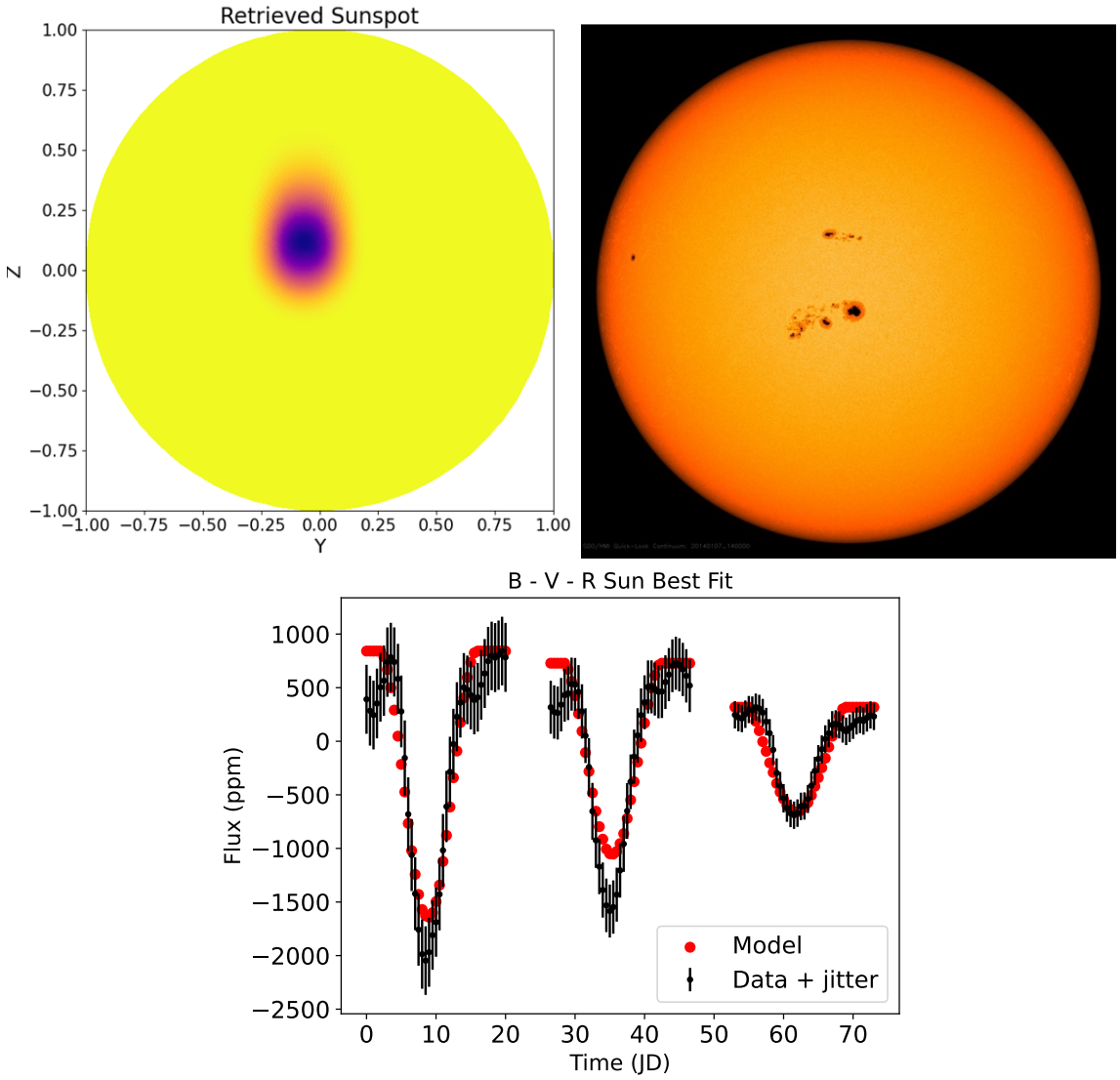

Figure 3.11: Left: simulated sunspot according to our model results, shown in Figure 3.10. Right: a real image of the Sun during the period studied, from HMI. Bottom: best fit of our model compared to the observed data for the Sun in all the three bands, from left to right, B, V and R filter. The data are shifted in time for clarity purpose.

3.6 Summary and Conclusions

In conclusion, modelling multiband photometry and assuming a single spot-dominated surface, we measured an effective temperature of the active regions of V1298 Tau which is probably a weighted average of the temperature of the spots, faculae and photosphere around them. Multiband photometry allows us to constrain this property, with the bluest photo-

metric bands that provide the strongest constraint. We may break the degeneracy between radius, latitude and temperature of the active region of the star, thanks to simultaneous multiband data, especially retrieving correctly its geometric properties, as we verified testing our code on the solar case. More bands, especially bluer bands, and a denser temporal coverage, likely, would help in reducing the temperature uncertainties and in distinguishing spots and other features of the surface and better constraining their positions. Finally, we developed a method to characterize surface inhomogeneities of quite active and young stars that has the advantage of using little and medium-size telescopes for few days. In conclusion, we suggest that this method, together with ground-based high-resolution spectroscopy and photometric observations from space, could improve our comprehension of active stars. For the future we hope to manage to organize further observations from Gal-Hassin and OPC in the incoming winter season, using the results of this work to optimize the time-coverage, the filters and observations strategy in order to acquire higher SNR data and better characterize stellar activity. We are also going to analyze REM and TNG data from AOT45 and AOT48 periods of observations to apply our activity retrieval method on other active stellar targets: DS Tuc A, TOI-179, HD 70573, AD Leonis and TYC 5909-319-1.

Chapter 4

Planetary transmission spectrum extraction in presence of stellar activity

4.1 Introduction

As discussed in chapter 1, stellar contamination is the dominant source of noise in the exoplanetary spectroscopic observations, so for accurate studies it will be essential to account for stellar activity, ideally in a homogeneous way to allow meaningful comparisons.

Usually, stellar activity is particularly strong for late type K-M dwarfs (e.g. Goulding et al. 2012; Jackson and Jeffries 2013; McQuillan, Mazeh, and Aigrain 2014; Newton, Irwin, et al. 2016) and for fast rotating, or young stellar objects (YSOs) (e.g. Gully-Santiago et al. 2017; Järvinen et al. 2018; Klein et al. 2022). These objects are important targets of present and future astronomical observations because late-type stars are frequently observed to host transiting planets i.e. sub-Neptunes and super-Earths (e.g. Dressing and Charbonneau 2015), fundamental targets for answering questions surrounding potential habitability. Unfortunately, the small atmospheric scale heights expected for these planets will result in weak diagnostic absorption features, which are much more susceptible to being obscured or altered by stellar contamination (Rackham, Apai, and Giampapa 2018; Zhang et al. 2018). Despite their high level of activity, recently the interest towards young stars hosting planets increased because they are fundamental to understand planetary systems formation and early evolution, but they require a method to correct the effects of stellar activity in the observed spectra.

Spectroscopic transmission observations of exoplanetary transits usually are in the interval from NIR-optical to near UV bands. Observing in these bands implies observing the signal from the stellar photosphere, where stellar activity produces spots and faculae (e.g. Solanki 2003; Berdyugina 2005). Their effect (together with flares, that are very fast and easy to recognize as explained in section 1) is the dominant source of noise in these planetary observations. Spots and faculae are regions of the photosphere with a temperature lower (spots) or higher (faculae) than the surrounding photosphere, then their presence can in fact create bumps or deepening in the transit light-curve if the planet occults these regions of the star during its passage, but their most subtle effect (e.g. Sing, Pont, et al. 2011; Ballerini et al. 2012; Pont, Sing, et al. 2013; Oshagh et al. 2014; Giuseppina Micela 2015; Rackham, Apai, and Giampapa 2018) is a change of the observed transit depth when spots and faculae are not occulted. The presence of unocculted spots/faculae, in fact, reduces/increases the average flux that originates by the star surface not crossed by the planet, deepening/reducing the transit light-curve and leading to an overestimation/underestimation of the planet radius. This effect is also strongly chromatic, being stronger at shorter wavelength (Ballerini et al. 2012; Pont, Sing, et al. 2013; Rackham, Apai, and Giampapa 2018). In particular, faculae can hide absorption features in the transit spectrum, while spots can mimic or strengthen them. Furthermore, because the evolution of spots and faculae has a timescale compatible with the stellar rotation or magnetic cycle of the star (Pont, Sing, et al. 2013), each planetary observation must be corrected independently by others, when different transits data are summed up together to improve the SNR of the spectrum or different observations are compared.

In order to correct the effect of spots and faculae we need to model their contribution to the stellar signal, balancing the complexity of our models with the related computational cost and with the quality expected from real spectral observations. Our aim is not to create a model able to retrieve from observational data the detailed properties of the active areas on the stellar surface, but to be able to retrieve the average effect of spots and faculae to correct the stellar spectrum with a sufficient precision, to correctly extract the planetary spectrum given by the data uncertainties.

The approach we adopted consists of two separated steps: simulations created by a forward model for the spots and faculae on the stellar surface and the application of bayesian

retrieval procedures to simulated data to test if simpler models than those used to simulate the observations could correct the simulated data at an acceptable level of precision. The results of this work will provide us useful informations on the level of complexity of the methods that should be accounted for when we will analyze real data, as those that will be obtained by Ariel. Indeed, part of the following analysis is focused on the observations that will be obtained by Ariel.

4.2 Forward Model

The forward model is made by two elements: the star and the planet. To simulate the planet we have to choose its fundamental parameters, mass, radius, and equilibrium temperature, and assume its atmospheric properties. The forward model requires the choice of its composition, pressure levels and also the presence of Rayleigh scattering and collision induced absorption (CIA). The transmission spectrum is simulated through TauREx3 (Al-Refaie et al. 2021) that requires the planetary parameters above. In case of realistic simulations of ARIEL observations, the errors associated to the spectrum are estimated with ArielRad (L. Mugnai et al. 2019), a tool able to simulate and estimate the different expected sources of noise expected in ARIEL observations. In this case, the simulation requires also the stellar magnitude that is used by ArielRad to estimate the errors.

The relevant properties of the host star for calculating the transmission spectrum are the stellar mass, radius, composition and temperature. The final step was the simulation of the activity of the star with our stellar forward model, called STARPA, an expansion of the model developed by Cracchiolo, G. Micela, and Peres 2021 and Cracchiolo, G. Micela, Morello, et al. 2021.

4.2.1 The active star modelling: STARPA

In order to simulate the spectrum of an active star, we used the known properties of the star, such as temperature, mass, local gravity, age and metallicity, to generate the spectrum of a quiet star using ExoTETHyS package (Morello et al. 2020). Then we added the contribution from the spots and faculae to calculate the appropriate spectrum expected from the star. These spectra are calculated with the hypothesis that spots and faculae can be modelled as portions of stellar atmospheres at different temperatures, at least for low spectral resolution

observations. Using this procedure, it is possible to generate a grid of forward models for various spots and faculae combinations. In our implementation, we also take into account the limb darkening effect for both the photosphere and the active regions of the star. The 4-th order limb darkening coefficients (Claret 2000) were estimated through ExoTETHyS package (Morello et al. 2020). The relevant properties of simulated spots and faculae in this model are their temperature, filling factor, and their position on the stellar surface. The method is an extension of the work of (Cracchiolo, G. Micela, and Peres 2021; Cracchiolo, G. Micela, Morello, et al. 2021), which discusses also the impact of the uncertainties in the knowledge of fundamental stellar parameters.

In order to proceed, we calculated spectral emission of the photosphere of the simulated star and of spots and faculae, modelling them as cooler and hotter stellar atmospheres respectively. Specifically, we used the BT-Settl (Claret, Hauschildt, and Witte 2012) stellar spectral model grids from the PHOENIX library to calculate the spectra. It should be noted that, due to limitations of available PHOENIX models, we are only able to model spots with temperatures greater than 1500 K, but to have an efficient retrieval we should avoid choosing a temperature below 2000 K to leave some free parameter space for the temperature exploration during the retrieval procedure. Finally, we apply the method to stars later than mid-F since earlier type stars are not expected to have dynamo that can generate spots (Berdyugina 2005), so our forward model is not expected to be used for photospheric temperatures above 6500 K.

In our simulations the metallicity and gravity are fixed at [M/H]=0 (solar) and log g=4.5, respectively and kept constant for photosphere, spots and faculae in order to isolate the effect of the temperature contrast of the active regions of the star, expected to be dominant with respect to other possible effects like alterations of local gravity and composition.

Once calculated the spectral emission of the three components of the stellar surface ($S_{Spot,\lambda}$ for spots, $S_{Fac,\lambda}$ for faculae and $S_{Star,\lambda}$ for photosphere) are combined, accordingly to their related filling factors (F_{Spot}, F_{Fac}, 1-F_{Spot}-F_{Fac}):

$$S_{Star,\lambda} = [(1 - F_{Spot} - F_{Fac}) \times S_{Phot,\lambda}] + (F_{Spot} \times S_{Spot,\lambda}) + (F_{Fac} \times S_{Fac,\lambda}) \quad (4.2.1)$$

Here, we expanded the procedure developed by (Cracchiolo, G. Micela, and Peres 2021;

Cracchiolo, G. Micela, Morello, et al. 2021) using circular spots with 2D elliptical projection when the spot is not at the center of the disk. In the new version, our code can simulate the faculae both as bright isolated regions and as circular rings around the spots (with the same kind of projection). In the following, we will use only the second option for practical reasons.

The star disk was divided in one thousand concentric annuli and for each of them we calculated the fraction of the annulus covered by the projected spots and faculae and the fraction covered by quiet photosphere. Each annulus was characterized by its radius r_i and ring thickness d_r and for each of them we calculated the emission $I_\lambda(r_i)$ given by a linear combination of the intensity contribution of spots, faculae and photosphere according to their covered fraction for each annulus.
The out-of-transit flux F_λ^{out} will be obtained by summing up the intensities from all the annuli:

$$F_\lambda^{out} = \sum_{i=1}^{N} I_\lambda(r_i) 2\pi r_i d_r$$

$$I_\lambda(r_i) = ff_{spot,i} \times I_\lambda(T_{spot}, r_i) + ff_{fac,i} \times I_\lambda(T_{fac}, r_i) + (1 - ff_{spot,i} - ff_{fac,i}) \times I_\lambda(T_\star, r_i) \quad (4.2.2)$$

where $ff_{spot,i}$ and $ff_{fac,i}$ are the fraction of the i^{th} annulus covered by the spot and facula respectively. $I_\lambda(T_{spot}, r_i)$, $I_\lambda(T_{fac}, r_i)$ and $I_\lambda(T_\star, r_i)$ are the intensity profiles emitted from the faculae, the spots and the photosphere, respectively, for each annulus. Each intensity profile is obtained with a 4-coefficients limb darkening law (Claret, Hauschildt, and Witte 2012):

$$\frac{I_\lambda(\mu_i)}{I_\lambda(1)} = 1 - \sum_{i=1}^{4} a_{n,\lambda}(1 - \mu_i^{n/2}) \quad (4.2.3)$$

where $\mu_i = \cos\theta$ for each annulus (where θ is the angle between the line of sight and the normal to the stellar surface) and $a_{n,\lambda}$ are the limb darkening coefficients. Finally, the integration of total flux of the stellar disk at each wavelength bin gives us the out-of-transit spectrum of the star. Once simulated the out-of-transit stellar disk, we repeat the procedure for each temporal step of the transit with the new equation, assuming that the planet does not cross spots or faculae:

$$I_\lambda(r_i) = ff_{spot,i} \times I_\lambda(T_{spot}, r_i) + ff_{fac,i} \times I_\lambda(T_{fac}, r_i) + (1 - ff_{spot,i} - ff_{fac,i} - ff_{p,i,j}) \times I_\lambda(T_\star, r_i)$$

(4.2.4)

where $ff_{p,i,j}$ is the fraction of annulus i^{th} covered by a planet at time j, calculated as $2 * \pi * (R_{p,i}/R_\star)^2$ where $R_{p,i}/R_\star$ is the in-transit original simulated spectrum. The integration on the annuli generates the transit light-curve (see Figure 4.1) at each spectral bin and the array of the depth of the transit light-curve at each wavelength is the planetary transit affected by stellar activity.

The code allows us also to include stellar rotation, but for most cases the rotational period of the star is much longer than the transit length, then, in the present application, we chose to keep the star fixed to reduce the total computational cost. With these hypotheses, there is a degeneracy between latitude and longitude for both spots and faculae that allows a simplification of our analysis. In conclusion, the forward model produces two relevant outcomes: an out-of-transit spectrum of the star and in-transit spectrum of the planet affected by the presence of spots and faculae on the stellar surface. It should be noted that in this study we are interested only in cases when the planet doesn't cover the spots/faculae. The case of occulted spots is much more complicated to study during the retrieval procedure and, however, its occurrence is in general evident in the observed transit light-curve showing clear bumps in the signal in correspondence with the crossing. As a first option, in absence of specific correction procedure, the time segment, corresponding to the bumps can be removed by the analysis. We will work on this topic in the near future.

4.3 Retrieval procedure

4.3.1 Planet spectrum extraction with the ASteRA method

The first application of the forward model described above has been in Thompson et al. 2024. ASTeRA is a new plugin of TauREx3 that include the possibility to retrieve the stellar spots contamination directly from the in-transit spectrum, together with the parameters of the planetary atmosphere in one single retrieval procedure. It does not resolve the stellar spots configuration and does not take into account limb darkening effects, but it is very fast and has the advantage of not requiring precise out-of transit observations, because it uses only in-transit data.

To test the capability of the ASTeRA retrieval procedure, the STARPA forward model

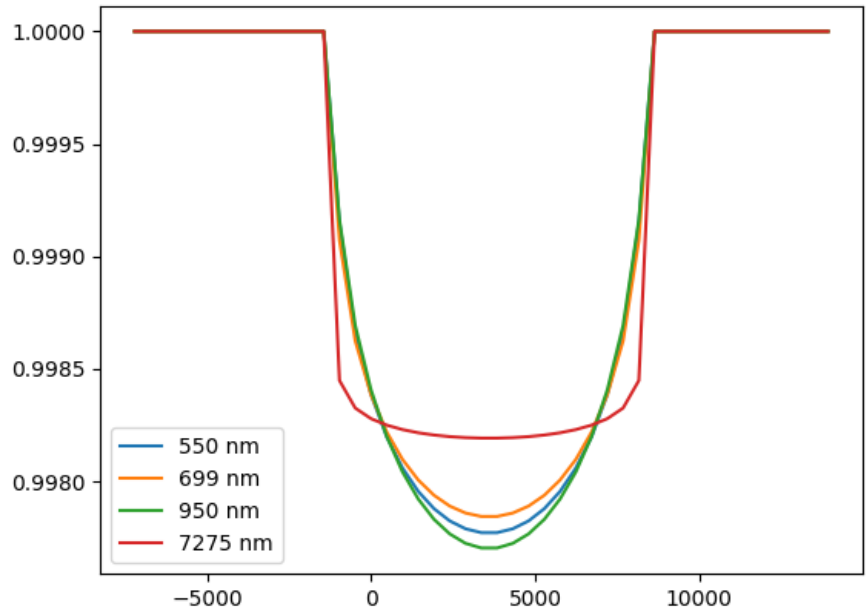

Figure 4.1: An example of the ideal transit light-curve simulated by STARPA forward model at each photometric band and for the last spectral bin of ARIEL. The transit light-curve was simulated in the ideal case of a quiet star without spots and faculae, to show how the transit depth changes at different wavelength. For the simulation, we used the M0 star and the planet described in subsection 1.3.2.

has been used. In practice, a "complex" forward model has been adopted, while a simpler retrieval model has been applied. If a simplified model can be used to retrieve the atmospheric parameters, it could be used in a standard pipeline for data analysis with a significant decrease of computer time, compared with a negligible loss of scientific content.

For this application we simulated a K dwarf star (T_{eff} = 4750 K, $R_\star$ = 0.8 $R_\odot$, $M_\star$ = 0.8 $M_\odot$) with a sub-Neptune transiting planet ($R_P = 3R_\oplus$ = 0.273 R_{Jup}, M_P= 5 $M_\oplus$ = 0.0157 M_J and T_{eq} = 400K) with a primary atmosphere containing water (logH_2O = -3) with H and He present as fill gases with a ratio of 0.172. We also included Rayleigh scattering and collision induced absorption (CIA) in the model atmosphere. The transit spectrum was simulated with a resolution of 200 spectral bins between 0.5 and 9.5 μm. Since we are interested in understanding the impact of the stellar activity independently on the statistics and on the instrument used for the observations, we assume no errors in the measurements.

We chose to simulate stars with one-spot configurations, exploring spots at different distances from the stellar disk center and with various radii and temperatures. We chose to simulate only one spot to have a simple starting point to test the ASTeRA retrieval method and to examine some extreme contamination cases with giant spots.

With the STARPA forward model we generated a grid of 27 active star cases changing the one spot parameters as shown in Table 4.1 to analyze them trough ASteRA. For each of them, we generated a transit spectrum affected by the spot contribution, carefully choosing the inclination of the planet orbit to avoid spot crossing during the transit. The retrieved spots filling factors are shown in Figure 4.2, compared with the input simulated spot filling factor. Discrepant cases correspond to low contrast spots or high latitude spots.

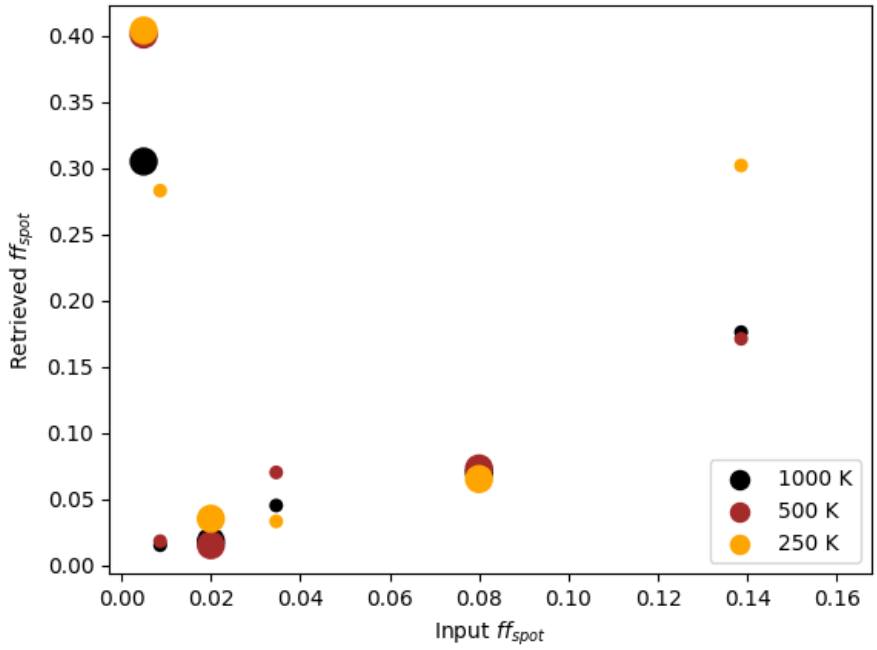

Figure 4.2: Comparison of the retrieved spot filling factor for 27 cases analyzed through ASTeRA procedure and the input simulated spot filling factor. The size of the markers are proportional to the latitude of the input spot.

The retrieval procedure with ASTeRA was applied assuming a star both with and without spot to verify if stellar activity was always relevant for transit analysis, and the bayesian evidence confirms that in most cases a model with activity is preferred with respect to a model of a quiet star (see Figure 6 from Thompson et al. 2024). The only exceptions are

Table 4.1: Grid of the 27 single spot cases simulated with STARPA, each characterized by a unique combination of three spot parameters: the temperature contrast with respect to the photosphere (ΔT_{Spot}), the spot radius normalized to the stellar radius (R_{Spot}) and the latitude of the spot center (ϕ_{Spot}). The spot filling factor (ff_{Spot}) is calculated assuming an elliptical projection onto the surface when the spot center is at non-zero latitudes. The table was adapted from Thompson et al. 2024

Case No.	ΔT_{Spot} (K)	R_{Spot} (R_*)	ϕ_{Spot} (°)	ff_{Spot} (%)
1	1000	0.1	0	1
2	1000	0.1	30	0.867
3	1000	0.1	60	0.498
4	1000	0.2	0	4
5	1000	0.2	30	3.462
6	1000	0.2	60	2.001
7	1000	0.4	0	16
8	1000	0.4	30	13.858
9	1000	0.4	60	7.997
10	500	0.1	0	1
11	500	0.1	30	0.867
12	500	0.1	60	0.498
13	500	0.2	0	4
14	500	0.2	30	3.462
15	500	0.2	60	2.001
16	500	0.4	0	16
17	500	0.4	30	13.858
18	500	0.4	60	7.997
19	250	0.1	0	1
20	250	0.1	30	0.867
21	250	0.1	60	0.498
22	250	0.2	0	4
23	250	0.2	30	3.462
24	250	0.2	60	2.001
25	250	0.4	0	16
26	250	0.4	30	13.858
27	250	0.4	60	7.997

the cases with small spot radius and a few cases with low temperature contrast.

The results of the retrieval of atmospheric parameters through ASTeRA show, as expected, that the results are more uncertain in the most contaminated cases and that the spot filling factor is poorly constrained in cases with a small spot either at high distance from the center or low temperature contrast. However, the resulting uncertainties are still small enough to allow a reliable characterization of the planetary atmosphere, as shown in Figure 4.3, that shows the comparison between the atmospheric parameters obtained from the retrieval accounting for the presence of a single spot and in the quiet star case hypothesis. It is clear that in most cases the quiet star retrieval can't reproduce the correct atmospheric and planetary properties, leading for example to an underestimation of H_2O mixing ratio of more than two orders of magnitude in strong contaminated cases with a bigger and colder spot. In many cases the activity correction works quite well in reproducing the input parameters, except for the most active stars.

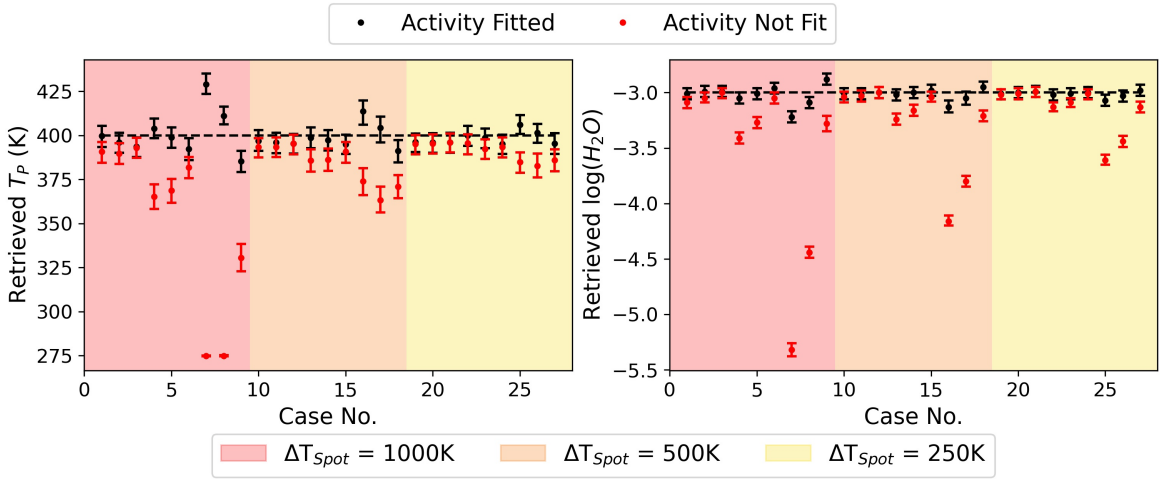

Figure 4.3: The retrieved planet temperature (left) and H_2O mixing ratio (right) obtained for each spot case when the spot parameters are fit for (black data points) vs when activity is not accounted for (red data points). The plot background colors correspond to the temperature contrasts of the spot considered for each case. The ground truth for each parameter is indicated by the dashed black line. From Thompson et al. 2024.

4.4 Planet spectrum extraction with the STARPA

As a further step, we chose to apply the STARPA modeling also to the retrieval procedure on a more complex forward model and to later types of stars, that in general, are more

difficult than solar-type stars to analyze. Furthermore, we adopted the method developed by Cracchiolo, G. Micela, and Peres 2021 and Cracchiolo, G. Micela, Morello, et al. 2021 performing the retrieval of the planetary atmosphere in three steps: first we model the out-of-transit stellar spectra, then, we use the out-of-transit stellar model to correct the spectrum during the transit and finally we perform the atmospheric retrieval using the corrected spectra to test the quality of our stellar correction and its impact in atmospheric analysis. The advantage of such approach is to avoid degeneracy between the chromatic effect of stellar activity and that of the planet spectrum, that with this method are clearly disentangled. In our retrieval procedure we also include the limb darkening effect.

We chose to simulate two different stars: a M0 dwarf (T_{eff} = 4000 K, $R_\star$ = 0.7 $R_\odot$, $M_\star$ = 0.45 $M_\odot$) and a M4 dwarf (T_{eff} = 3200 K, $R_\star$ = 0.21 $R_\odot$, $M_\star$ = 0.18 $M_\odot$[1]). For both stars we chose to simulate configurations with 2 spots with a hot ring (faculae) around each of them. For the faculae we chose a ΔT_{fac} = +300 K over the photosphere temperature, while for spots we assume a ΔT_{Spot} = -1200 K below the stellar temperature. We considered the case with a sub-Neptune planet with R_P = 0.273 R_{Jup}, M_P = 0.0157 M_J and T_{eq} = 1000 K. The planet-star distance has been calculated as 0.02 AU for the M0 dwarf star and as 0.0142 AU for the M4 star to achieve the required planet equilibrium temperature. This is the value of the temperature expected for a planet in thermal equilibrium with its star radiation thanks to its blackbody emission and its albedo and, with the approximation of an even distribution of heat between day side and night side of the planet, and it can be calculated through the following equation (Catling and Kasting 2017; Méndez and Rivera-Valentín 2017):

$$T_{eq} = \left[\frac{L(1-Ab)}{16\pi\sigma a^2}\right]\frac{1}{4} \tag{4.4.1}$$

where a is the major semi-axis of the planet orbit, Ab=0.3 is the Bond albedo coefficient of its surface, L is the luminosity of the star and σ is the Stefan-Boltzmann coefficient.

We used, as in the previous section, a primary atmosphere containing water ($\log H_2O$ = -3) with H and He present as fill gases with a ratio of 0.172. We also included Rayleigh scattering and collision induced absorption (CIA) in the model atmosphere. We generated then for each star a grid of 243 configurations, combining the following ranges of spot-faculae

[1] same stellar parameters of LHS 1140 star, that will be analyzed in the following chapter

parameters:

- latitude (degenerate with longitude, since we are neglecting the stellar rotation during the transit duration) of 0, 30 and 60 deg for the first spot and of 10, 40 and 70 deg for the second one;
- spot radius (normalized to the stellar radius) of 0.01, 0.15 and 0.3 for each spot;
- thickness of faculae ring around spot of 0.001, 0.01 and 0.05, normalized to the stellar radius.

It should be noted that in some of these cases faculae's filling factor results greater than the spot's one, leading to a facula-dominated scenario. There are also configurations where two spots/faculae are partially or totally merged.

Finally, we used STARPA forward model to produce for each of these cases the transit light-curve at each spectral bin of tier 2 Ariel mission, estimated through ArielRad code (L. V. Mugnai et al. 2020), from which we derived the corresponding out-of transit and in-transit spectra. We assumed minimum SNRs of 10 for each spectral bin that is of the same order of the uncertainty expected for a number of realistic Ariel targets. We chose to use the expected spectral bins and uncertainties of ARIEL to better explore its capability to obtain good exoplanetary atmospheric observations in case of active stars.

In particular, STARPA simulated out-of-transit spectra feed the bayesian framework *Multinest v3.10* (Feroz, Hobson, and Bridges 2009), explained in Chapter 3, to retrieve the best-fit values of parameters and their associated errors, i.e. the spots/faculae parameters. The priors used in this retrieval procedure are the same for the two stars and are shown in Table 4.2 and we chose to use 500 live points to achieve sufficient precision. For the retrieval procedure we chose to work with a model simpler than that used for the forward model and in particular with a single spot to model the activity produced by the two spots with faculae ring of the input forward model and to retrieve from them the realistic observable properties of the resulting average active region. Our goal was to test if a simple retrieval of an average effective spot (realistic due to the expected observing uncertainties) could still lead to a good correction of the planetary in-transit spectrum even in the presence of more (usually unknown) complex active regions on the star.

Table 4.2: Priors of Multinest v3.10 retrieval used to analyze out-of-transit spectra of the simulated data.

Parameter	**Prior Bounds**	**Scale**
T_{spot}(K)	1500-4500	linear
$R_{spot}(R_*)$	0.05-0.5	linear
lat(deg)	0-90	linear
jitter	$10^{-3} - 10^{6}$	logarithmic

4.4.1 Stellar Results

As a first step, we analyzed the quality of the retrieval of stellar properties. In Figures 4.4 and 4.5 we show examples of the retrieved spots corner plots in low and high activity cases for the M0 and M4 dwarf stars, respectively. In both figures we report a case with two small spots ($R_{spot} = 0.01R_*$) at high latitudes, 60 and 70 deg respectively, and thin facula ring (thickness of 0.05 R_*) with a case with large spots at lower latitudes ($R_{spot} = 0.03$ and $0.15R_*$ at 0 and 40 deg latitude, respectively) with a faculae ring thickness of 0.05 R_*. In both figures there is an anticorrelation between latitudes and retrieved spots radius in high activity case, due to the degeneration of spots parameters discussed in Chapter 3. Furthermore, Figure 4.6 shows the correlation between the average filling factor retrieved by MultiNest and the actual simulated total filling factor of spots for M0 (top) and M4 (bottom) star. As expected, we can see clearly a linear correlation between these two parameters in both cases. Finally, in Figures 4.7 we show the correlation between the retrieved spot temperature and the weighted mean temperature of the total active region of the input forward models resulting from the contributions of the simulated faculae and spots. It should be noted that in most cases the retrieved temperature is close to the input, except for a number of cases faculae-dominated or with very low filling factors.

4.4.2 Planet Spectrum Extraction

After the modeling of the stellar activity discussed above, the retrieved properties of the star are used to calculate the chromatic coefficients (see Eq. 1.4.1 in Chapter 1) to correct the in-transit spectrum of the planet. An example of the obtained corrected spectrum is

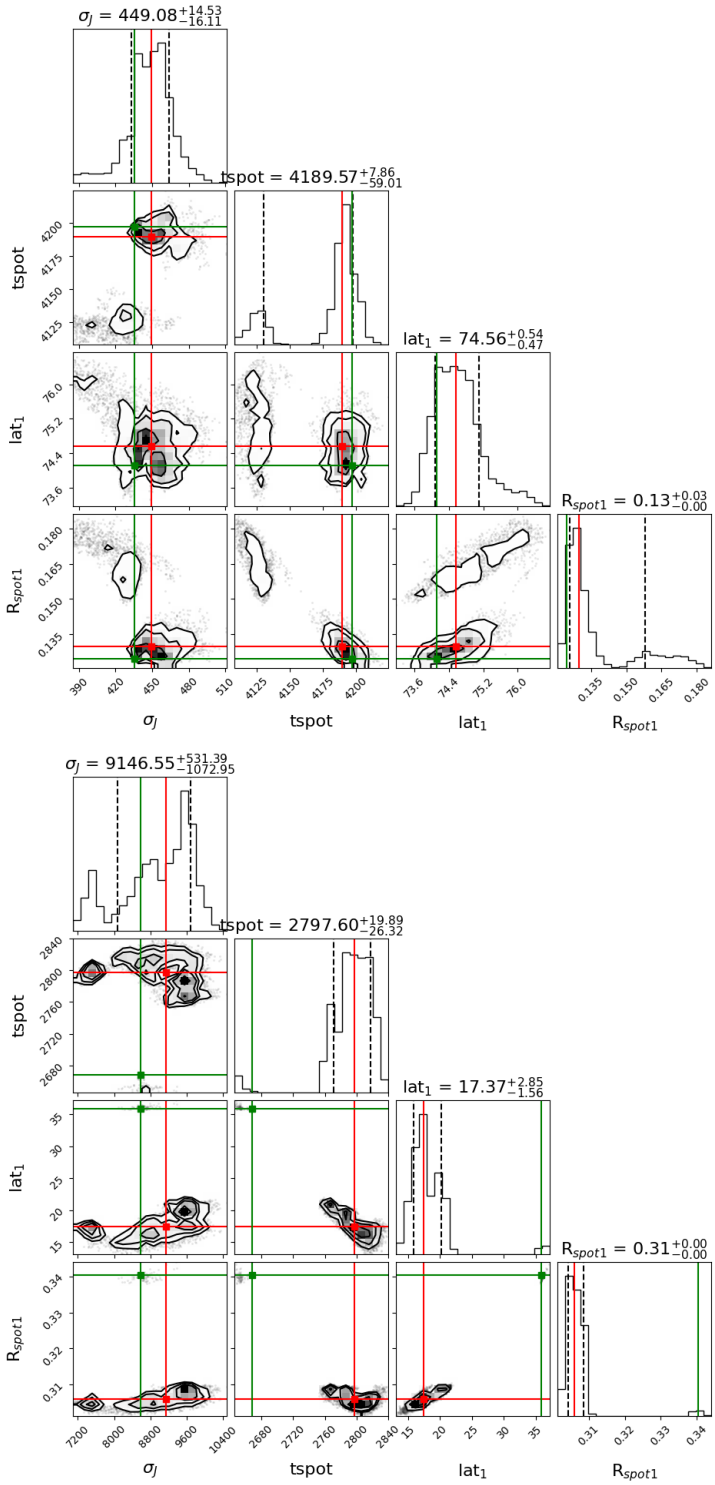

Figure 4.4: Examples of corner plot of the retrieved spot properties for the M0 dwarf star in a low (top) and high (bottom) activity case.

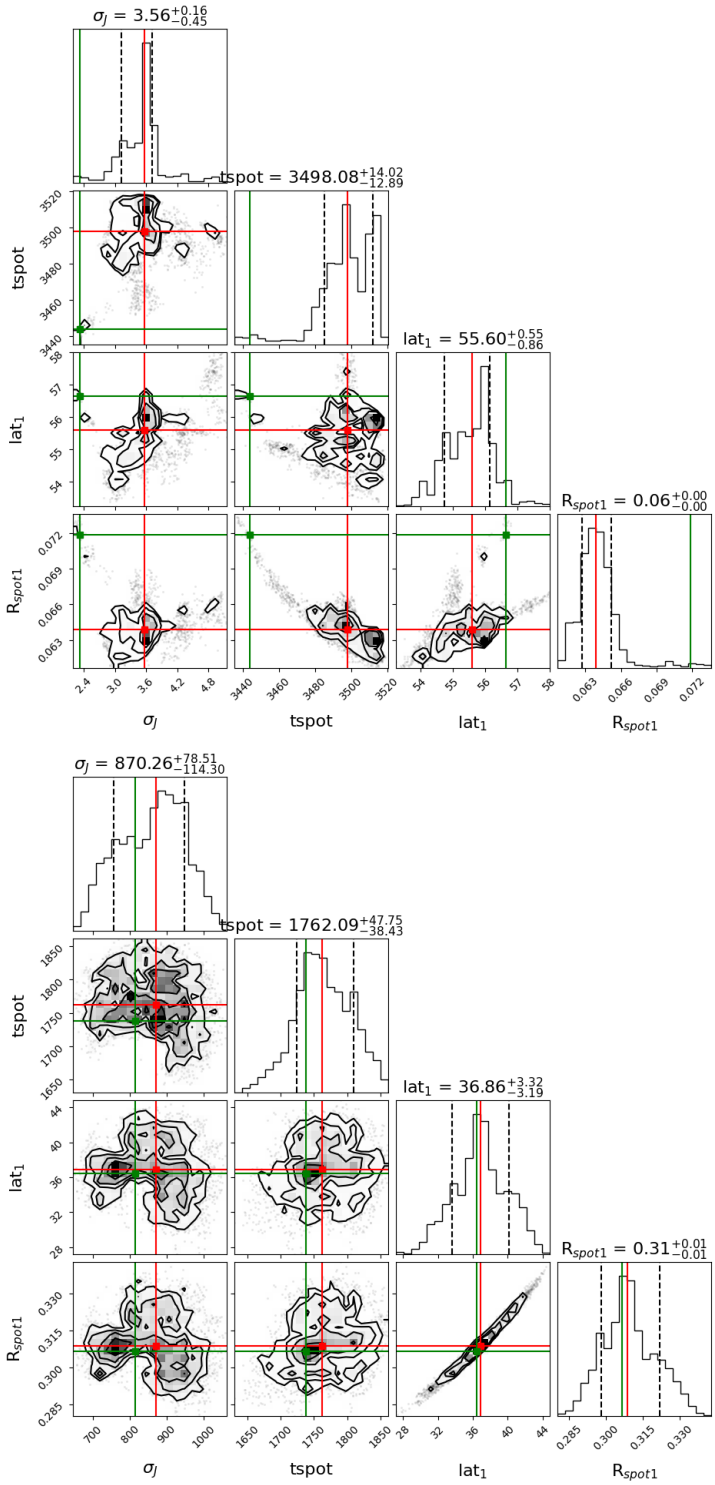

Figure 4.5: Examples of corner plot of the retrieved spot properties for the M4 dwarf star in a low (top) and high (bottom) activity case.

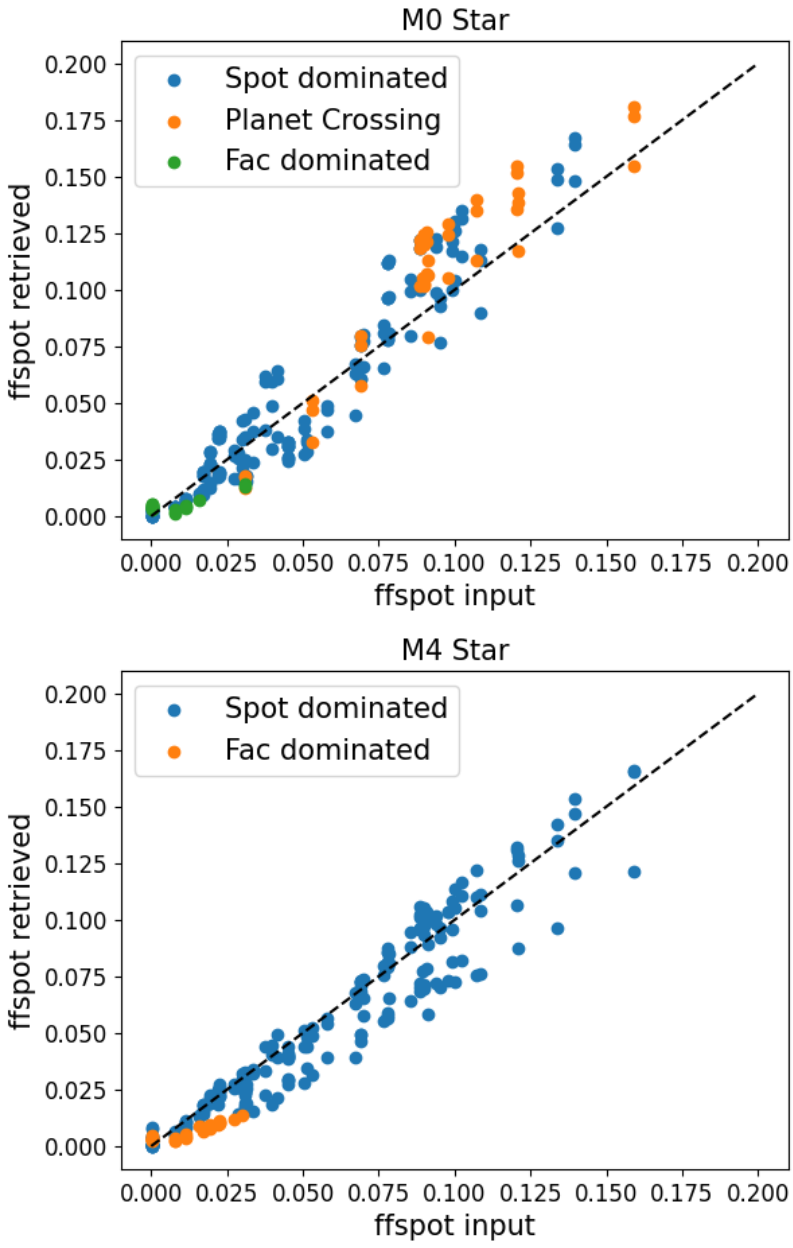

Figure 4.6: Correlation between the retrieved filling factor of the average spot found by MultiNest and the actual filling factor of the spots simulated by the forward model in each of the cases studied for the M0 (top) and M4 stars (bottom).

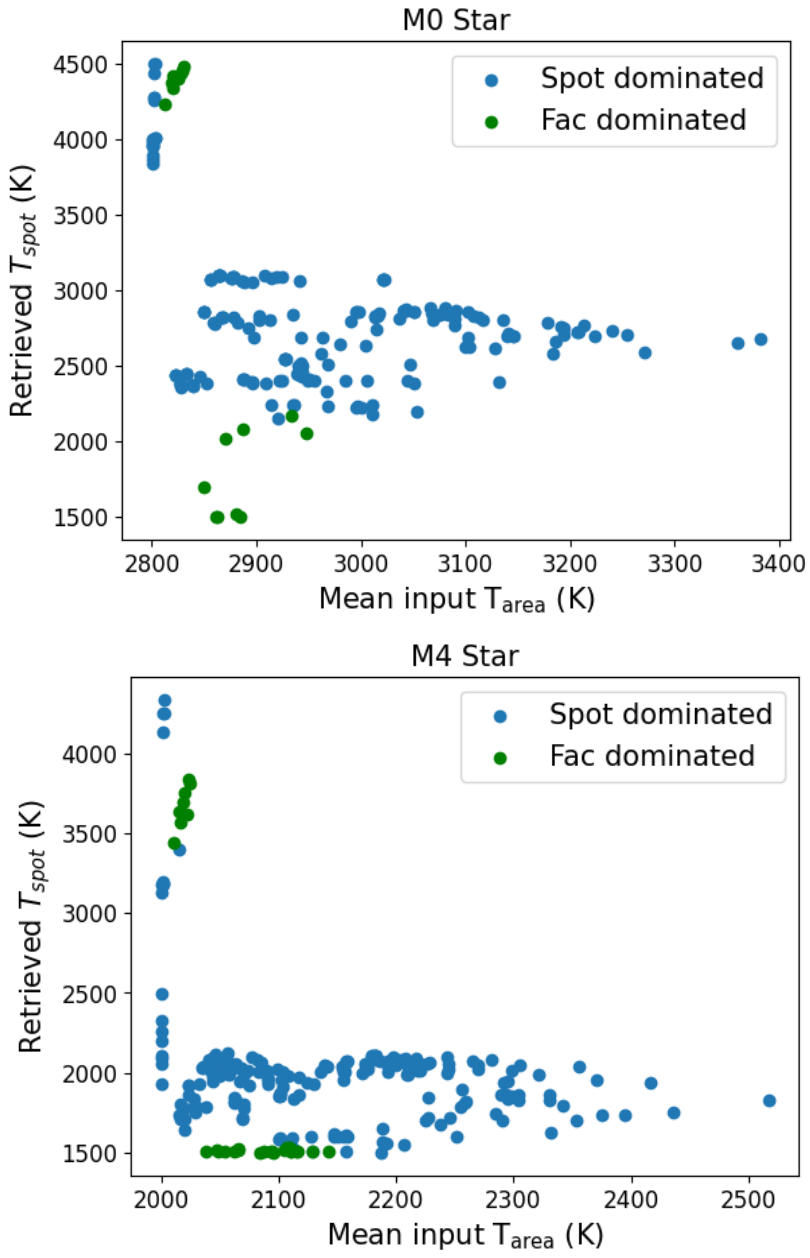

Figure 4.7: Correlation between the mean temperature of the retrieved spot found by MultiNest and the mean weighted temperature due to the combinations of the spots and faculae simulated by the forward model in each of the cases studied for the M0 (top) and M4 (bottom) stars.

shown in Figure 4.8 for one of the studied cases for the M4 star. When the planet does not cross the spots or the faculae during the transit (the planet-spot crossing cases are 45 for M0 dwarf), our method can correct the in-transit spectrum with great precision, with a difference between the corrected transit spectra and the original one often smaller than the typical error bars expected from Ariel tier 2 single observations. We can evaluate the quality of the correction computing the χ^2 using the following equation:

$$\chi^2 = \sum_{i=1}^{N} \frac{(S_{retr,i} - S_{input,i})^2}{err_i^2} \tag{4.4.2}$$

where $S_{input,i}$ is the input planetary spectrum, $S_{retr,i}$ is the retrieved spectrum and err_i is the simulated observing uncertainty expected from Ariel, calculated using ArielRad. The resulting distributions are shown for both the M4 and M0 stars in Figure 4.9. Most of the cases fall in the first bin. The cases at high χ^2 are mainly found for high input filling factor (see Figure 4.10). Likely, these high activity cases require more complex models in the retrieval procedure. Furthermore, in 45 cases for the M0 star, the planet projection crosses the spot or the faculae. In these cases, the spectrum correction is not sufficient, leading to a large difference with the original one, sometimes comparable or even greater than that between the original simulated spectrum and the uncorrected one affected by spots and faculae contribution. This is expected since the modeling is based on no-crossing spot planets. We will analyze spot crossing transit in future works, but for now we must notice that usually these situations are evident in the data because of the typical bumps in the light-curve produced during the spot crossing event.

4.4.3 Atmospheric Retrievals

After correcting the transit spectra, we used TauREx3 atmospheric retrieval framework to retrieve from them the corrected radius, temperature and water mixing ratio of the planet, using the priors shown in Table 4.3. For the retrieval we chose to use 500 live points to achieve sufficient precision and we included CIA and Rayleigh scattering to obtain a more realistic retrieval. Figure 4.11 show the histograms of the distribution of the retrieved planetary equilibrium temperatures in every case studied for the M0 (top image) and M4 (bottom image) star, while Figure 4.12 shows the histogram of the distribution of the retrieved H_2O mixing ratio for both the M0 (top image) and M4 (bottom image) stars. For M0 stars,

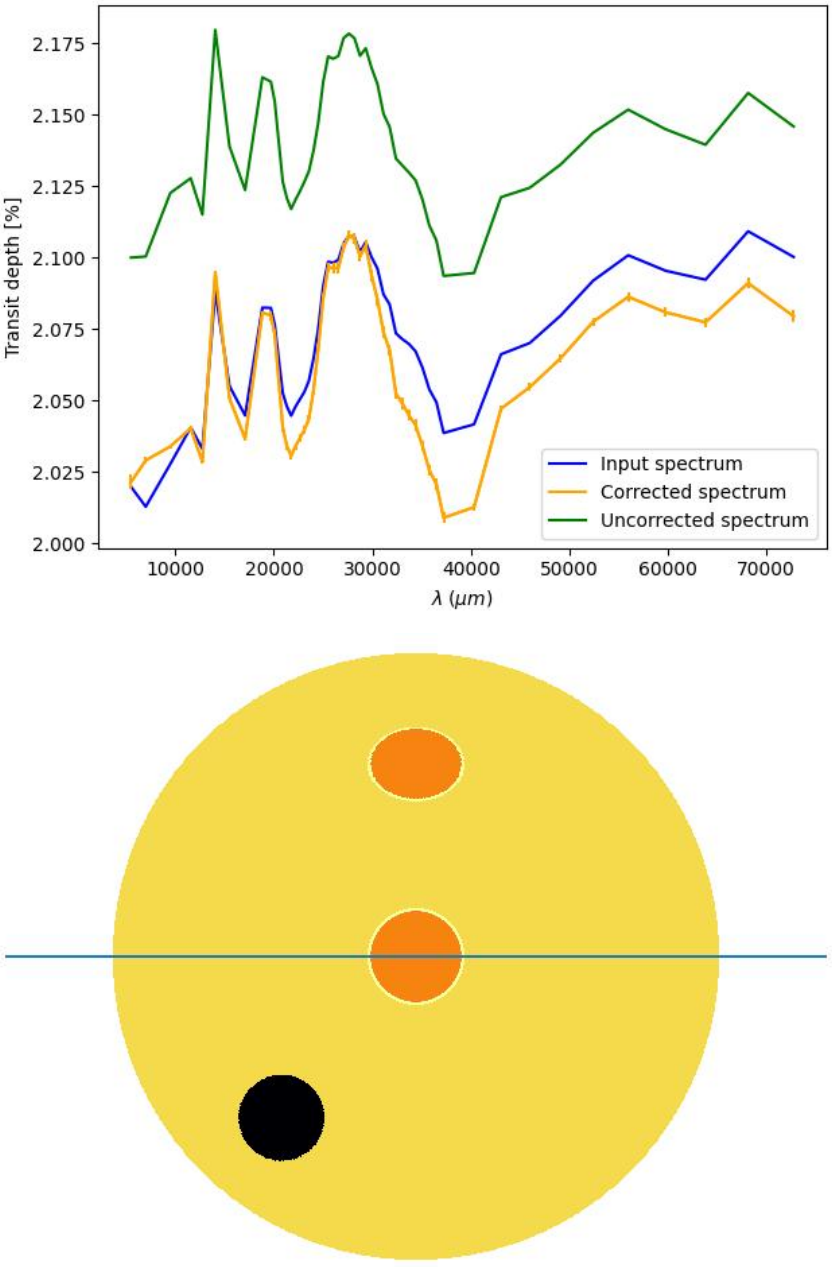

Figure 4.8: Top:A comparison of the original simulated spectrum (blue) and the uncorrected (green) and corrected one (orange) in one of the cases studied (with a realistic filling factor) for the M4 star. Bottom: the corresponding simulated M4 star with its spots and faculae.

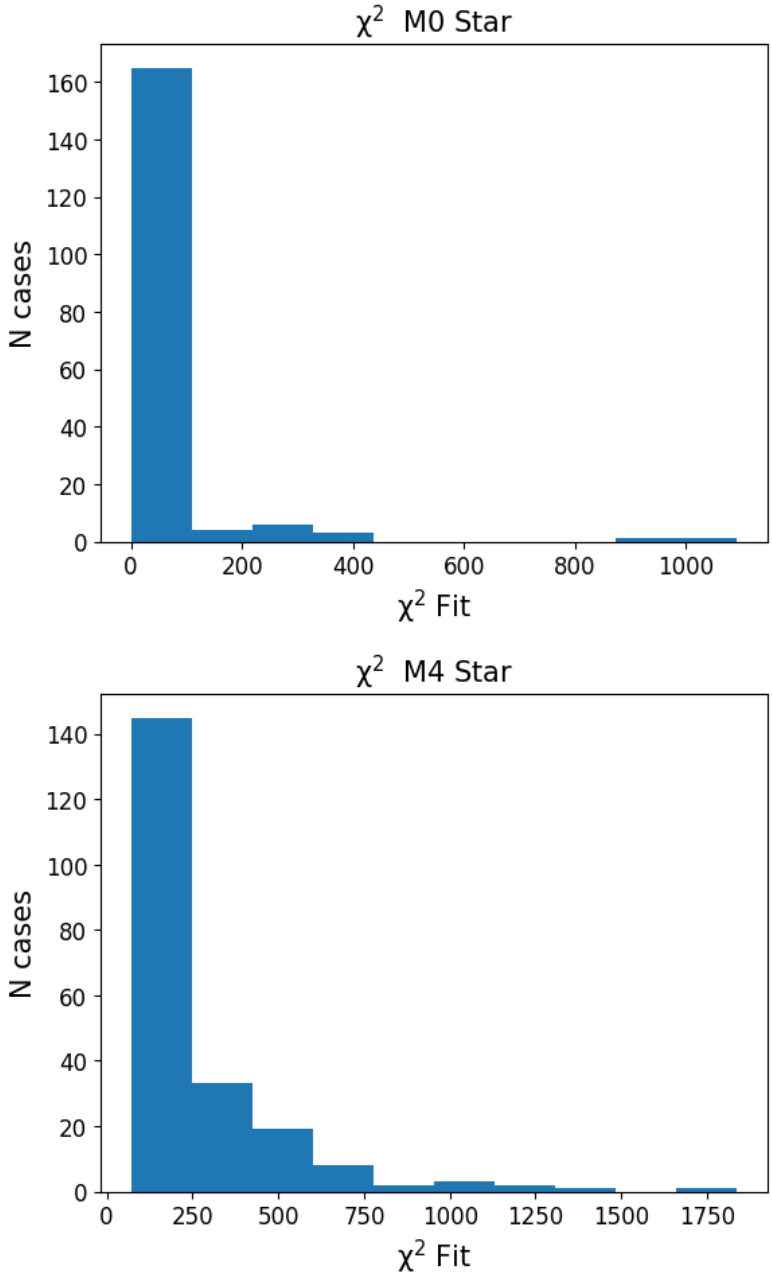

Figure 4.9: χ^2 distribution of the corrected spectrum in respect to the input one for the simulated M0 (top) and M4 (bottom) stars.

the equilibrium temperature is well retrieved, with most of the values between 900 and 1150 K. The most discrepant values correspond to the spot-crossing cases. For M4 stars, the histogram is larger, with the majority of cases close to the input values, but with a significant fraction (about 40%) with temperature lower than 900 K. In every case analyzed

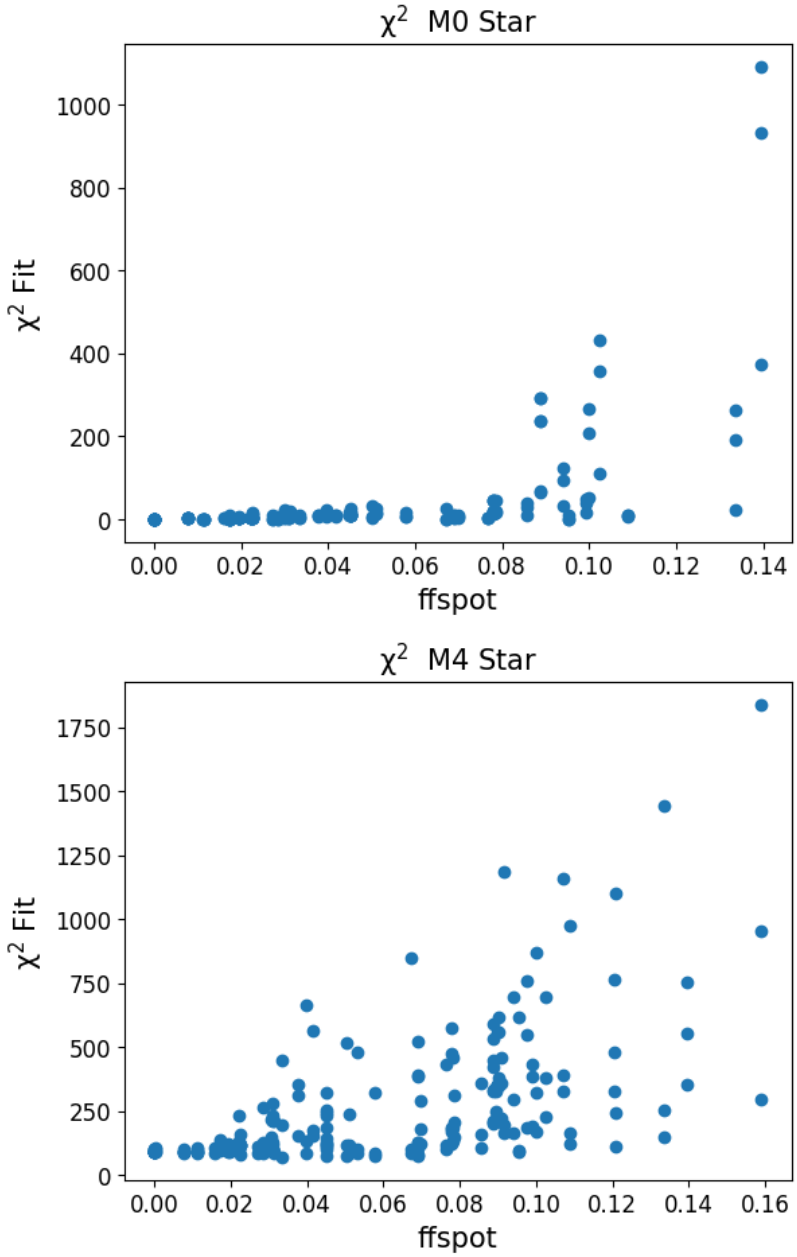

Figure 4.10: Relation between χ^2 distribution of the simulated M0 (top) and M4 (bottom) stars and the input simulated spot filling factor.

we are able to retrieve the presence of water. For M0 stars, except for the crossing spot planets, the derived abundance is within half an order of magnitude of the input value, while, for M4 dwarf cases, there is a wider scatter of the retrieved parameters, leading in many cases to an overestimate of the H_2O mixing ratio. In Figure 4.13 we show the relation

Table 4.3: Priors of TauREx3 atmospheric retrieval framework used in our work. "V_{H_2O}" is the volume mixing ratio of H_2O in the planet atmosphere.

Parameter	**Prior Bounds**	**Scale**
V_{H_2O}	-12, 0	$\log_{10}$
T_{eq}(K)	100, 1500	linear
$R_p(R_{jup})$	0.050, 0.500	linear
He/H_2	0.172	fixed

between the retrieved atmospheric H_2O mixing ratio and planetary temperature for M0 (top image) and M4 (bottom image) stars, showing a clear linear anticorrelation between the two values, maybe due to a degeneracy in atmospheric retrieval. It's quite clear the effect of planet-spot crossing in M0 dwarf case as a leading error source in the atmospheric retrieval. Finally, in Figure 4.14 and we show how the total spot filling factor affects the retrieval of the planetary temperatures in both M0 and M4 case respectively, showing how the uncertainties in temperature increase with a linear relation in presence of greater spot filling ratios, as expected. It should be finally noted that the atmospheric retrieval is still able to find water in the planet atmosphere also in spot crossing cases of the M0 dwarf star, though with greater uncertainties and with a wider scatter in temperature retrieval. The results for all models are reported in APPENDIX C.

The analysis of the results of this chapter, indicates that the adopted approach provides reliable results for planets non-crossing the spots and in the cases of non-extreme activity regime. The first case requires the development of a specific procedure, while the case of high stellar activity (and probably for very late stars) requires the adoption of a more realistic model in the retrieval framework.

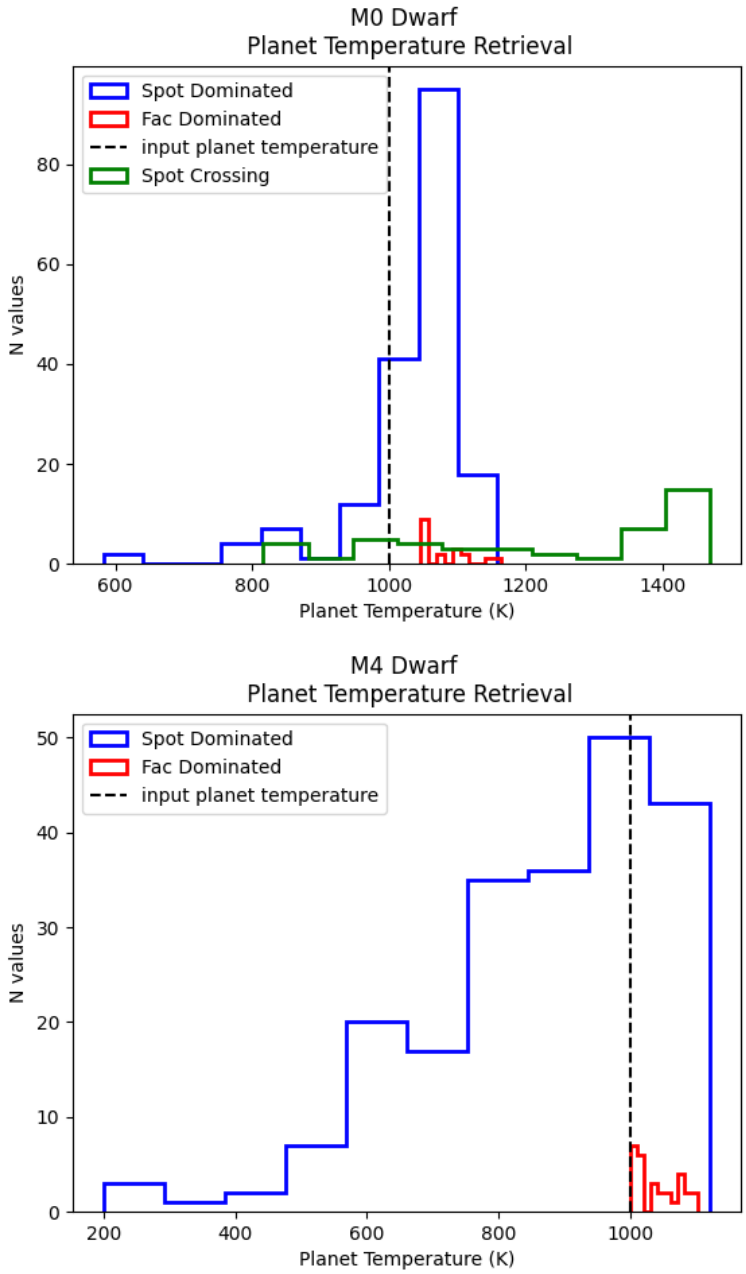

Figure 4.11: Histogram of the atmospheric temperature of the simulated planet around the M0 (top) and M4 (bottom) stars retrieved applying the TauREx3 retrieval procedure to the simulated transit spectra corrected by stellar activity effects.

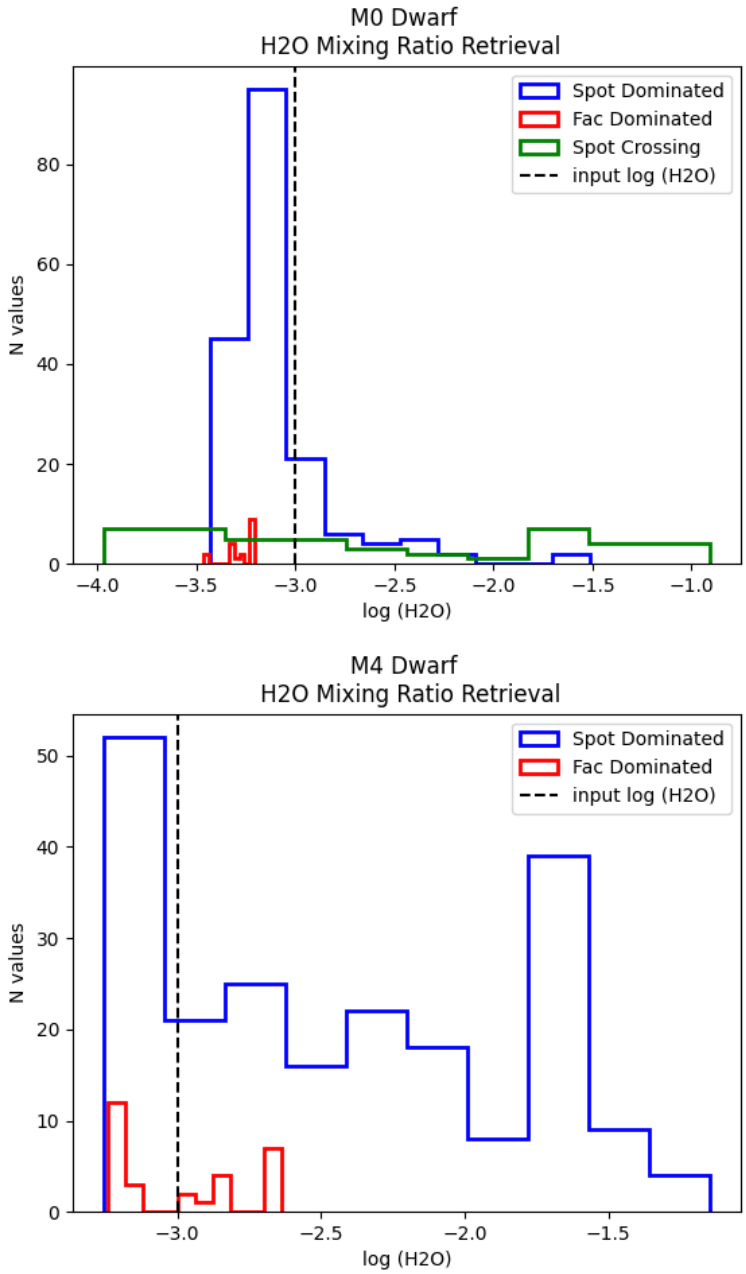

Figure 4.12: Histogram of the atmospheric H_2O mixing ratio of the simulated planet around the M0 (top) and M4 (bottom) stars retrieved applying the TauREx3 retrieval procedure to the simulated transit spectra corrected by stellar activity effects.

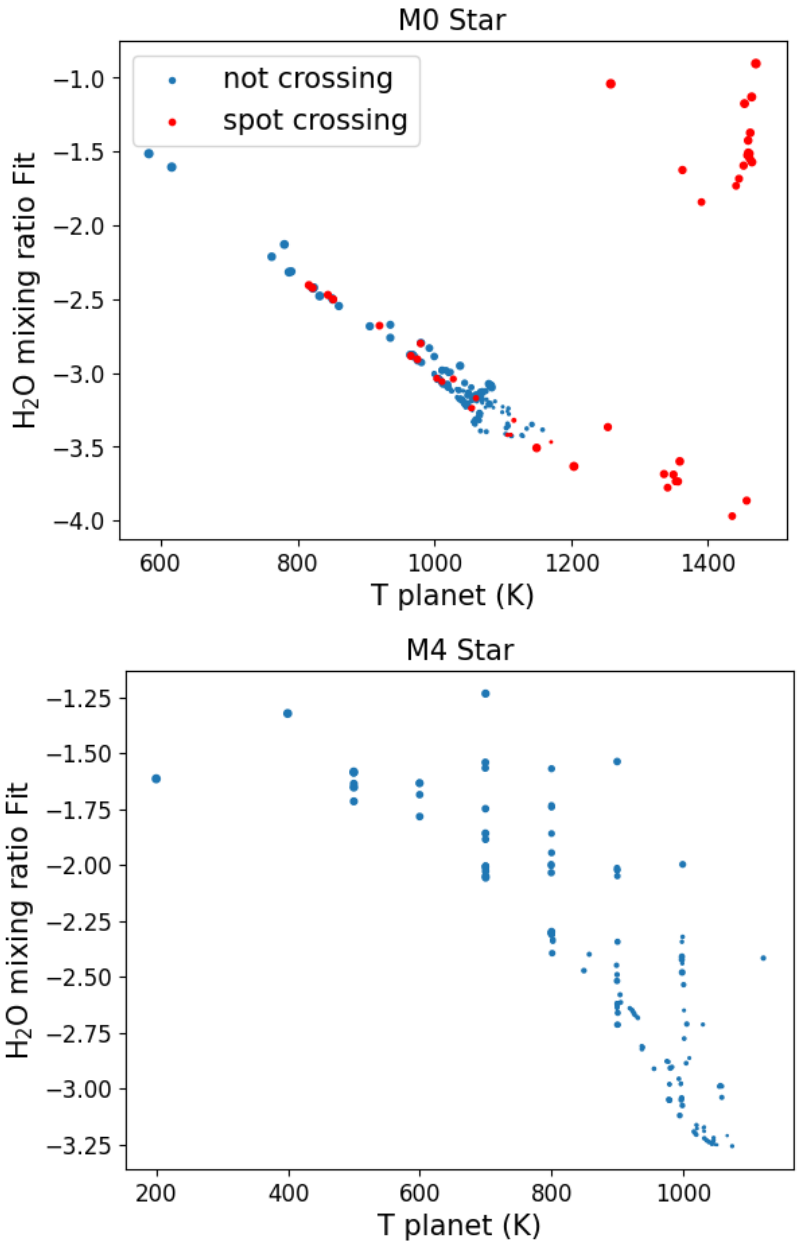

Figure 4.13: Relation between the retrieved planet temperature and the retrieved H_2O mixing ratio for M0 (top) and M4 (bottom) stars. Marker's size is proportional to the total filling factor of each studied case.

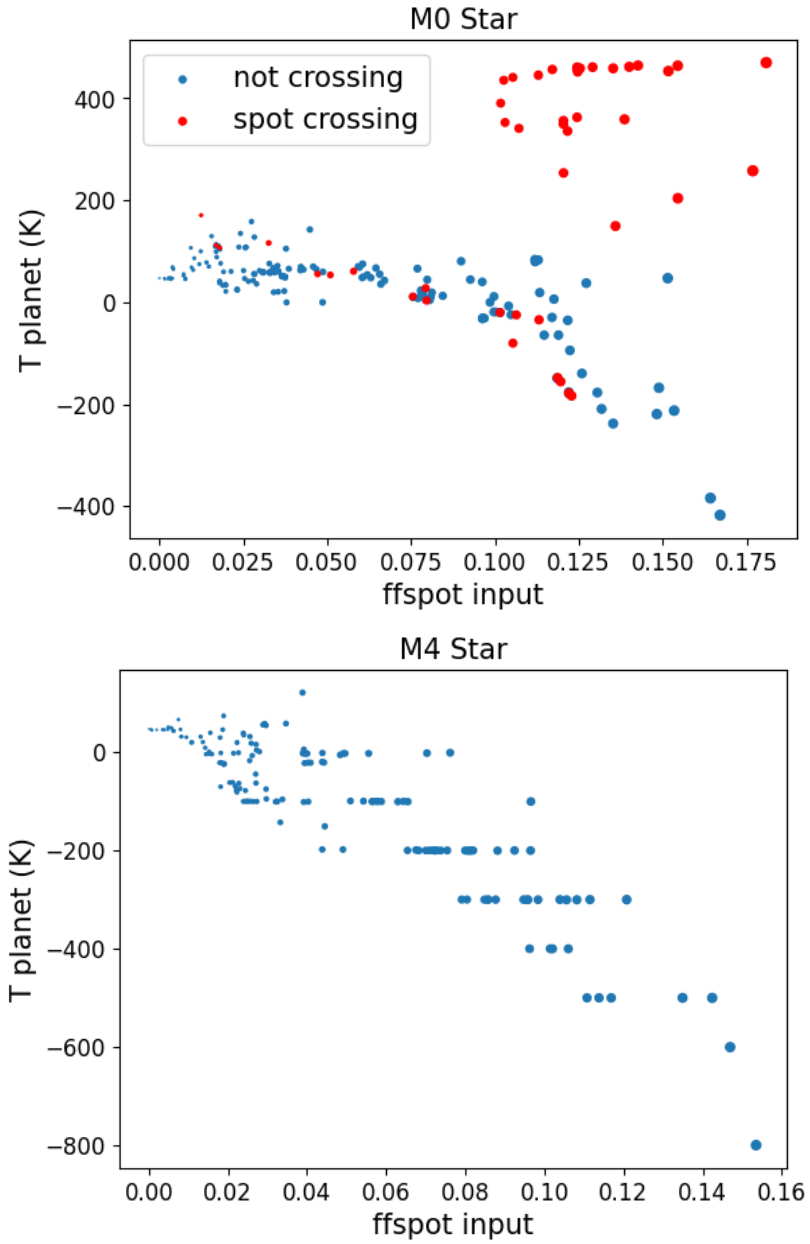

Figure 4.14: Relation between the retrieved planet temperature error and the total spot filling factor, in M0 (top) and M4 (bottom) dwarf cases. Marker's size is proportional to the total filling factor of each studied case. It's clear the strong effect of spot-planet crossing in the retrieval in the M0 star case.

Chapter 5

LHS 1140 b

5.1 LHS 1140 b

LHS 1140 is a M4.5-type star, $m_V = 14.5$ (Zacharias et al. 2013), located in the constellation of the Whale, at a distance of at (12.47 ± 0.42) pc (Dittmann et al. 2017; Gaia Collaboration et al. 2023) from the solar system. It has a surface temperature of 3096 ± 48 K (Cadieux et al. 2023) while Ment et al. 2019 estimated a value of 3216 ± 39 K. The star has a mass of $0.184 \pm 0.005\,M\odot$ and a radius of $0.216 \pm 0.003\,R\odot$ (Cadieux et al. 2023).
In April 2017, the exoplanet LHS 1140 b was discovered, orbiting at 0.0946 ± 0.0017 AU from its star with a period of 24.73723 ± 0.00002 days (Gomes and Ferraz-Mello 2020; Cadieux et al. 2023). Its radius is $1.730 \pm 0.025\,R_\oplus$, as derived by Ment et al. 2019; Cadieux et al. 2023, and references therein from photometric transit observations of Spitzer (Werner et al. 2004) and MEarth-South (Berta, Irwin, et al. 2012) survey. Using radial velocity measurements from the high-resolution HARPS spectrograph (M. Mayor et al. 2003), Cadieux et al. 2023 estimated a planetary mass $M_p = 5.60 \pm 0.19\,M_\oplus$, resulting in a density of 5.9 ± 0.3 g cm^{-3}, very similar to the Earth density. Its equilibrium temperature is evaluated as 226 ± 4 K (Cadieux et al. 2023). We analyzed HST data from two transit observations of LHS 1140 b that were acquired for proposal 14888 (PI: Jason Dittmann) with the WFC3/HST G141 grism and were taken in January and December 2017. Our analysis starts from the raw spatially scanned spectroscopic images collected with Hubble WFC3 and obtained from the Mikulski Archive for Space Telescopes (MAST)[1]. Both visits utilized the GRISM256 aperture, and 256 x 256 subarray, with an exposure time of 103.13 s which consisted of 16

[1] `https://mast.stsci.edu/portal/Mashup/Clients/Mast/Portal.html`

up-the-ramp non-destructive reads using the SPARS10 sequence. The visits had different scan rates with 0.10"/s and 0.14"/s used for January and December respectively, resulting in scan lengths of 10.9" and 15.9". In 2018, a second terrestrial planet orbiting LHS 1140 was discovered with the primary transit technique: LHS 1140 c (Ment et al. 2019), orbiting at 0.0270 ± 0.0005 AU from its star, with an orbital period of 3.777940 ± 0.000002 days and an equilibrium temperature of 438 ± 9 K (Cadieux et al. 2023). Its radius is $1.272 \pm 0.026\,R_{\odot}$ while its mass is 1.91 ± 0.06, with a mean density of 5.1 ± 0.4 g cm^{-3} (Cadieux et al. 2023).

LHS 1140 b and c are ideal targets for atmospheric characterization with the JWST and the upcoming Ariel mission: they are both super-Earths orbiting an M dwarf star and the planet b is potentially in its habitable zone (HZ). Moreover Wunderlich et al. 2019 showed through simulations that H_2O, CH_4 and also CO_2 should be detectable in the case of LHS 1140 b.

5.2 Reduction and analysis of WFC3/HST data

Before we proceed further in the analysis of the HST data, it is mandatory to briefly summarize the main steps involved in the reduction of the data. Although two transits of LHS 1140 b were obtained using WFC3, the January visit was discarded from our analysis since it was affected by large shifts in the location of the spectrum on the detector (see also Edwards, Quentin Changeat, et al. 2021). For this reason we focus only on the December observation, which uses both forward and reverse scanning modes of the instrument. In the following, Iraclis[2] (Tsiaras, Waldmann, Zingales, et al. 2018), a specialized open-source software for the analysis of WFC3 scanning observations, was used. The reduction process includes the following steps: zero-read subtraction, reference pixels correction, non-linearity correction, dark current subtraction, gain conversion, sky background subtraction, flat-field correction, and corrections for bad pixels and cosmic rays (for a detailed description of these steps, see the original Iraclis paper, Tsiaras, Waldmann, Zingales, et al. 2018) and this reduction pipeline is common for both out-of-transit and in-transit spectra. For the December observation, the reduced spatially scanned spectroscopic images were used to extract the white (in the range $1.1 - 1.7\,\mu$m) and spectral light curves. The spectral light curves bands were selected as in Edwards, Quentin Changeat, et al. 2021, that is in such a way that the

[2] `https://github.com/ucl-exoplanets/Iraclis`

signal-to-noise ratio (SNR) is approximately uniform across the planetary spectrum. The first orbit of each visit was discarded as it presents stronger wavelength-dependent ramps, and also the first exposure in each HST orbit after each buffer dump was removed since it contains significantly lower counts than subsequent exposures, e.g. (Deming et al. 2013; Tsiaras, Waldmann, Rocchetto, et al. 2016). The light curves were fitted by using the transit model package PyLightcurve (Tsiaras, Waldmann, Rocchetto, et al. 2016) which utilizes the MCMC (Markov Chain Monte Carlo) code emcee (Foreman-Mackey et al. 2013). The only free parameters for the fitting of the white light curve were the mid-transit time and the planet-to-star radius ratio. The other planet parameters were fixed to the values from Cadieux et al. 2023 ($a/R_\star = 94.47, i = 89.86°$) while we used the same limb darkening coefficients (LDCs) of Edwards, Quentin Changeat, et al. 2021. The stellar parameters used to download the LDCs were taken from Edwards, Quentin Changeat, et al. 2021 and the selected database was PHOENIX-2012-13[3] (Claret, Hauschildt, and Witte 2012). The WFC3 exoplanet observations are usually affected by two kind of time-dependent systematics: the long-term and short-term "ramps" (Tsiaras, Waldmann, Zingales, et al. 2018). In Iraclis, these systematics in the white time series are fitted by using the following equation:

$$R_w(t) = n_w^{scan}[1 - r_a(t - T_0)](1 - r_{b_1}e^{-r_{b_2}(t-t_0)}) \tag{5.2.1}$$

where t is time, n_w^{scan} is a normalization factor, T_0 is the mid-transit time, t_0 is the time when each HST orbit starts, r_a is the slope of a linear systematic trend along each HST visit and r_{b_1}, r_{b_2} are the coefficients of an exponential systematic trend along each HST orbit. The normalization factor n_w^{scan} is the averaged out-of-transit flux in the white light curve. n_w^{scan} is adapted to n_w^{for} for forward scanning mode and to n_w^{rev} for reverse scanning mode. The reason for using different normalization factors is the slightly different effective exposure time due to the known upstream/downstream effect (McCullough and MacKenty 2012). Initially, the white light curve is fitted by using Eq. 5.2.1 with Iraclis. Next, the spectral light curves are fitted with a transit model where the only free parameter is the planet-to-star radius ratio along with a model for the systematics (R_λ) that included the white light curve (divide-white method, Kreidberg et al. 2014) and a wavelength-dependent,

[3] `https://phoenix.ens-lyon.fr/Grids/`

visit-long slope (Tsiaras, Waldmann, Zingales, et al. 2018) parameterized as follows:

$$R_\lambda(t) = n_w^{scan}(1 - \chi_\lambda(t - T_0))\frac{LC_w}{M_w} \tag{5.2.2}$$

where χ_λ is the slope of a wavelength-dependent linear systematic trend along each HST visit, LC_w is the white light curve and M_w is the best-fit model for the white light curve. The normalization factor n_w^{scan} is the averaged out-of-transit flux in each spectral bin centered at λ. Again, the normalization factor n_w^{scan} is changed to n_w^{for} for upward scanning directions (forward scanning) and to n_w^{rev} for downward scanning directions (reverse scanning). The white light curve fit is shown in Figure 5.1 and the subsequent spectral light-curve fits are shown in Figure 5.2. A full list of stellar and planet parameters used here for the fitting is given in Table 5.1. It should be noted that in this work we use the out-of-transit spectrum of the star to model its properties. In principle, there could be some chromatic time-dependent systematics in the absolute flux estimations that could affect the retrieval of the stellar properties based on the out-of-transit spectrum of the star. We verified that these systematics, if present, are negligible for our analysis as it is shown it in APPENDIX D. It should also be noted that Iraclis corrections does not correct possible residual wavelength-dependent systematics in the absolute flux.

5.3 Spectral Analysis

Edwards, Quentin Changeat, et al. 2021 suggested the possibility that some features of the spectrum of LHS1140 b could be due to stellar spots contamination and tried to simulate them. However, the X-ray luminosity value (L_x) of LHS 1140 b as reported by Riccardo Spinelli et al. 2023 put this star at the lower end of the X-ray distribution function ($L_x \sim 1.4 \times 10^{26}$ erg s^{-1}) pointing to a quiet old star. Moreover, the analysis of the TESS light-curves shows no significant signs of activity (Bonney and Kennefick 2022). LHS 1140 also has a long rotational period of about 131 days (Dittmann et al. 2017; Newton, Mondrik, et al. 2018), suggesting a low level of activity (Pizzolato et al. 2003). These observational evidences suggest that LHS 1140 is rather a quiet, inactive star. Therefore, it is rather unlikely that stellar spots might severely affect its stellar spectrum. In the following, we will test the alternative hypothesis that the star has a non-solar chemical composition.

Table 5.1: Stellar parameters of LHS 1140 and planetary parameters of LHS 1140 b taken from Cadieux et al. 2023. The value of the mid-transit time, T_{mid}, is derived in this work.

PARAMETER	**VALUE**
$R_\star[R_\odot]$	0.216 ± 0.003
$M_\star[M_\odot]$	0.184 ± 0.005
$T_\star$[K]	3096 ± 48
log(g)	5.041 ± 0.016
$M_p[M_\oplus]$	5.60 ± 0.19
$R_p[R_\oplus]$	1.730 ± 0.025
a[AU]	0.0946 ± 0.0017
i[deg]	89.86 ± 0.04
e	$< 0.043(95\%)$
P_{orb}[d]	24.73723 ± 0.00002
$T_{mid}[BJD_{TDB}]$	$2458103.08346 \pm 0.00005$

5.3.1 Stellar Composition

In order to do so, we evaluated various stellar atmospheric models to determine which one could best describe the observed out-of-transit spectrum. We generated a set of stellar spectra obtained from the PHOENIX-2012-2013 database to mimic the stellar photosphere. This involved selecting the models with log(g) = 5.0 and with stellar temperature within a wide range (2300-3500 K). We explored several stellar compositions by combining the metallicity [Fe/H] and the α value of the star. In particular, we tested the metallicity [Fe/H] within the range [-1.0,1.0] with a 0.5 step. Then, we also evaluate the α enrichment for the low metallicities cases: [Fe/H] = -0.5 dex with $\alpha = +0.2$ and [Fe/H] = -1.0 dex with $\alpha = +0.4$.

The resulting spectra were multiplied for the HST G141 grism sensitivity (calibrated by Kuntschner et al. 2011), accounting for the conversion from flux to electrons units. Two other chromatic components were taken into account: the dispersion of light from the star at the focal plane of the detector due to the grism and the dependence of the point spread

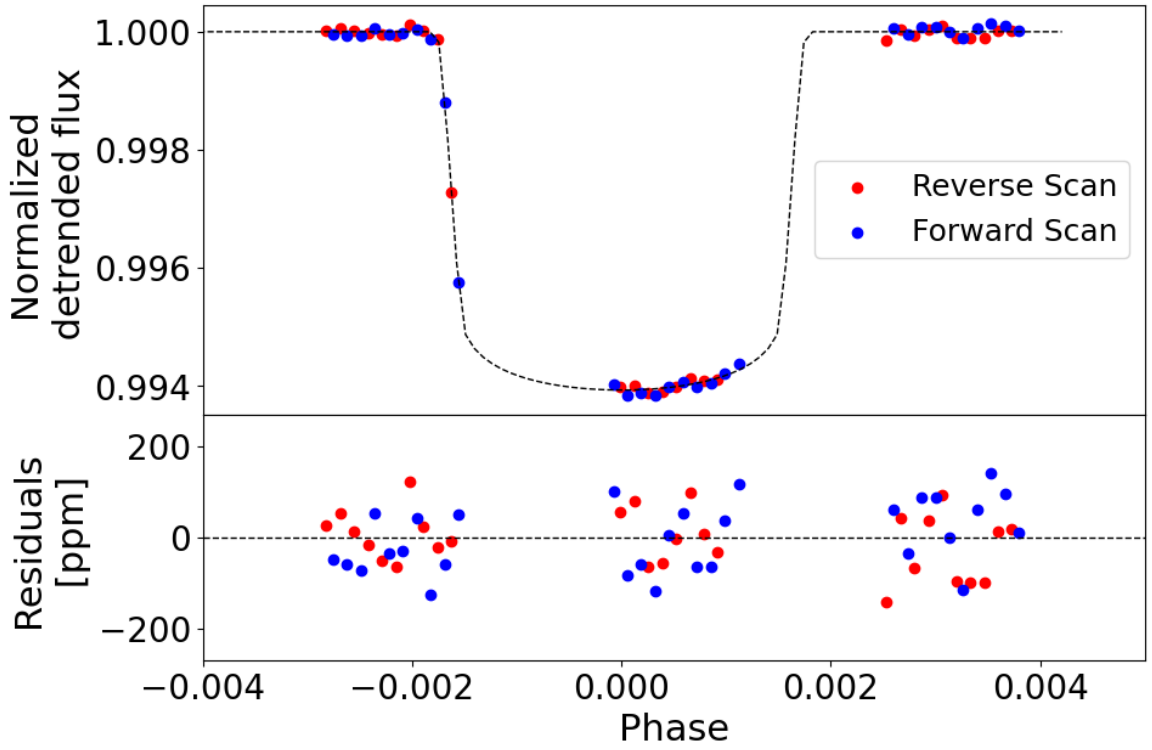

Figure 5.1: White light curve fit for December observation of LHS 1140 b. Top: detrended flux (points) and best-fit model (dashed line). Bottom: residuals from best-fit model.

function (PSF) on the wavelength observed. A detailed description of these two effects can be found in Varley, Tsiaras, and Karpouzas 2017. Finally, the spectra are binned by using the same binning used to fit the spectral light curves.

Figures 5.3 and 5.4 show a comparison between the data and the various tested models, highlighting how the parameters (temperature, metallicity [Fe/H] and α enrichment) impact the shape of the stellar spectrum. Specifically, we observe an increase in the amplitude of the features around ~ 1.3 μm at lower temperature, and the rise in flux in the red end of the spectrum at higher metallicity. The residuals between the observed data and the models are shown at the bottom of each plot. Finally, in Tab. 5.2 we show the χ^2 values of the models at 3100, 3200 and 3300 K, that better fit the observations. Each χ^2 value is obtained using:

$$\chi = \sum_{i=1}^{N} \frac{(obs_i - S_i)^2}{S_i} \tag{5.3.1}$$

where N is the number of spectral bin observed, "obs_i" are the observed spectral fluxes and S_i are the theoretical spectral fluxes predicted by the model for the specific stellar

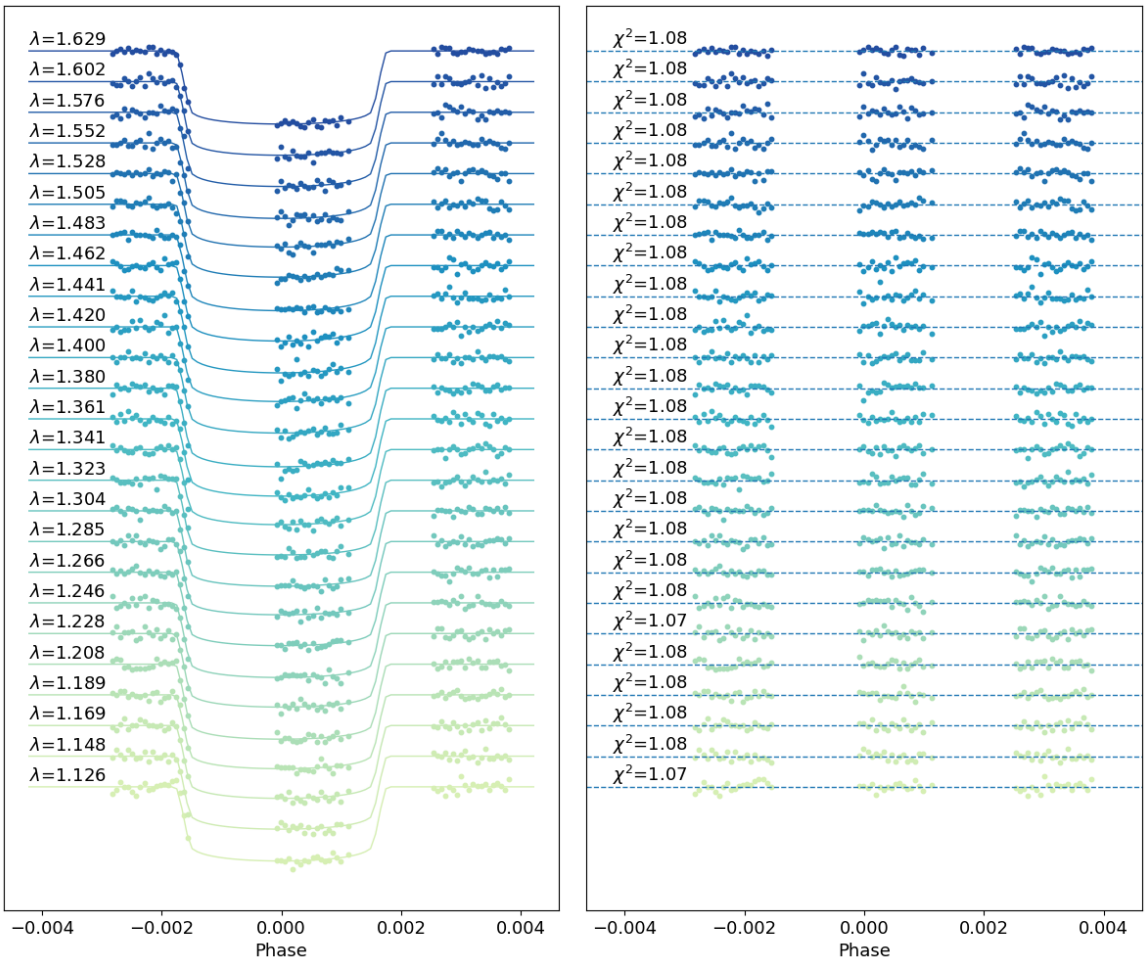

Figure 5.2: Normalized spectral light curve fits from Iraclis for the transmission spectrum of LHS 1140 b where, for clarity, an offset has been applied. Left panel: the detrended spectral light curves with the best-fit models plotted; right panel: residuals from the fitting to the reported values of the Chi-squared (χ^2).

composition tested.

Based on these tests, we identified a model of a quiet star with a combination of temperature, metallicity, and α ($\mathrm{T} = 3200\,\mathrm{K}, [\mathrm{Fe/H}] = -1.0\,\mathrm{dex}, \alpha = +0.4$) that provides a good representation of the observed out-of-transit spectrum without evidence of chromaticity effects in the residuals, as illustrated in Figure 5.5. Note that we are comparing the data with a grid of models and not fitting the best temperature. This result, together with other previous evidences of the low level of activity of the star both from XUV observations (see Riccardo Spinelli et al. 2023) and from TESS almost flat light curves analysis for this target

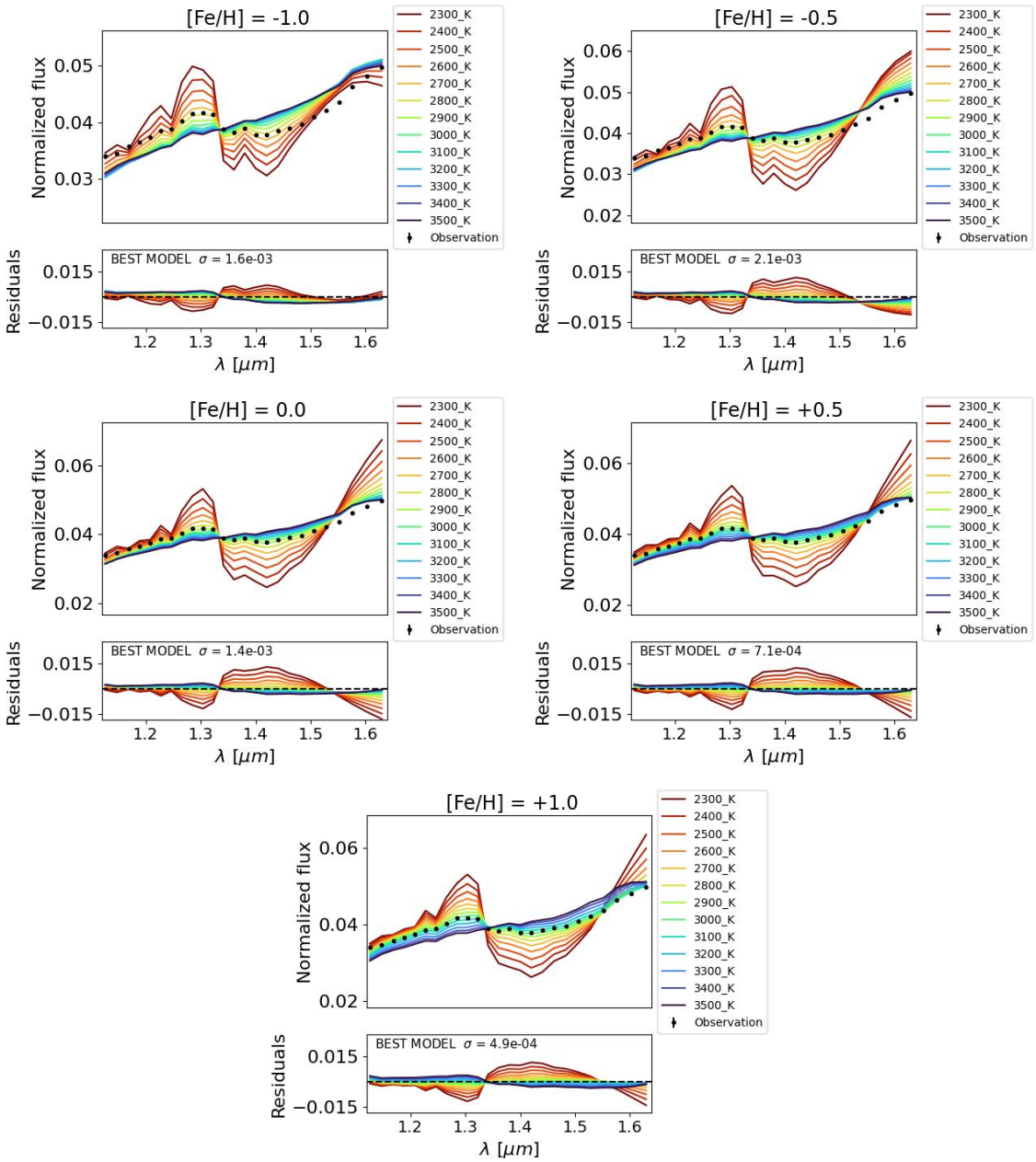

Figure 5.3: Comparison between the observed out-of-transit stellar spectrum (dots, uncertainties are within the symbol size) and the simulated Phoenix spectra at different temperatures (2300-3500 K, see legends) and at different compositions: [Fe/H] = -1.0 dex (top left), [Fe/H] = -0.5 dex (top right), [Fe/H] = 0.0 dex (center left), [Fe/H] = +0.5 dex (center right), [Fe/H] = +1.0 dex (bottom). In each graph we show the standard deviation of the best model for each given stellar metallicity.

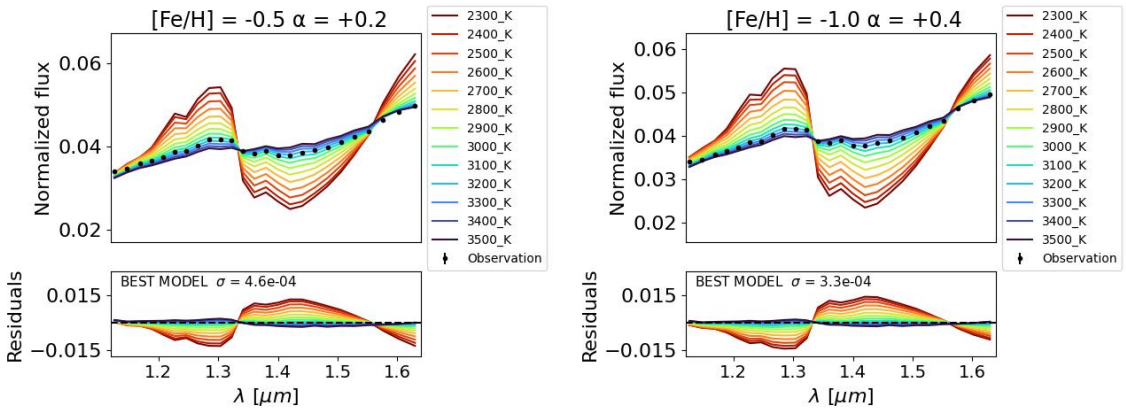

Figure 5.4: Comparison between the observed out-of-transit stellar spectrum (dots, uncertainties are within the symbol size) and simulated spectra corresponding to an α enriched star: the left panel corresponds to a composition of [Fe/H] $= -0.5$ dex and $\alpha = +0.2$ and the right panel corresponds to a composition of [Fe/H] $= -1.0$ dex and $\alpha = +0.4$, both cases with a range of temperatures between 2300 and 3500 K. In each graph we show the standard deviation of the best model for each given stellar composition.

Table 5.2: List of χ^2 values for each stellar composition test with a given stellar temperature of 3100 K, 3200 K and 3300 K, the values of the stellar temperature nearest to the best fit of the data. "Z" is the metallicity and "α" the α enrichment of the star.

Z	α	χ^2_{3100K}	χ^2_{3200K}	χ^2_{3300K}
-1.0	0.0	4.30e-03	4.76e-03	4.95e-03
-0.5	0.0	3.06e-03	3.43e-03	3.71e-03
0.0	0.0	1.45e-03	1.92e-03	2.44e-03
+0.5	0.0	5.25e-04	1.05e-03	1.85e-03
+1.0	0.0	2.32e-04	8.17e-04	2.03e-03
-0.5	+0.2	2.28e-04	1.39e-04	3.67e-04
-1.0	0.4	4.41e-04	7.26e-05	1.32e-04

(Bonney and Kennefick 2022) and the good correspondence between the temperature of this model (3200 K) and that derived by literature (3216 ± 39 K, derived by Ment et al. 2019), strongly suggests to rule out any strong stellar activity contribution in this transit observation. This lack of stellar activity implies that the planetary spectrum doesn't need a correction for stellar activity contamination and that its spectral features are only due to

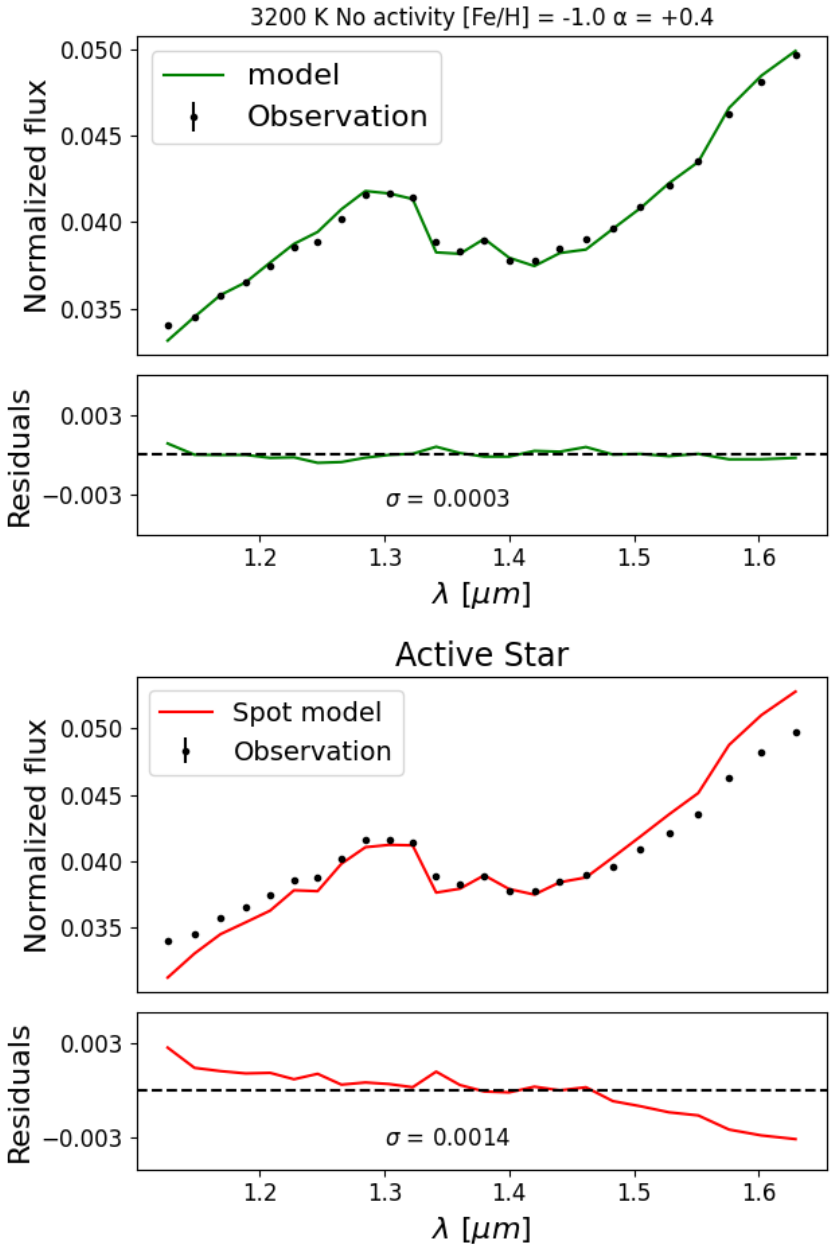

Figure 5.5: Top: comparison between the observed HST data (black dots) and the simulated phoenix spectrum at 3200 K and with a composition of [Fe/H] = -1.0 and α = +0.4 (green line). Bottom: comparison between the same data (black dots) with the best-fit spectrum (red line) corresponding to the best one spot model found by our stellar activity simulations. In both images residuals are shown in the lower panel with the related standard deviation.

the planetary atmosphere.

5.3.2 Stellar Activity Evaluation

As a further check, we compared the observations with the simulated spectrum of a star with a dominant spot, following the methodology described in Cracchiolo, G. Micela, Morello, et al. 2021.

The star is modeled as having one dominant circular spot with radius R_s (normalized to the stellar radius $R_\star$) on the stellar surface, whose projection onto the stellar disk is an ellipse with eccentricity dependent on the fractional distance d between the spot center and the center of the stellar disk. In this case the stellar disk is divided into N = 10 000 annuli, each with radius r_i and width d_r , and characterized by an emission $I_\lambda(r_i)$ given by a linear combination between the intensity emitted from the spot and the intensity emitted from the photosphere.

The out-of-transit flux F_λ^{out} will be obtained by summing up the intensities from all the annuli:

$$F_\lambda^{out} = \sum_{i=1}^{N} I_\lambda(r_i) 2\pi r_i d_r$$

$$I_\lambda(r_i) = ff_i \times I_\lambda(T_s, r_i) + (1 - ff_i) \times I_\lambda(T_\star, r_i) \tag{5.3.2}$$

where ff_i is the fraction of the i^{th} annulus covered by the spot. $I_\lambda(T_s, r_i)$ and $I_\lambda(T_\star, r_i)$ are the intensity profiles emitted from the photosphere and from the spot, respectively, for each annulus. Each intensity profile is obtained with a 4-coefficients limb darkening law (Claret, Hauschildt, and Witte 2012):

$$\frac{I_\lambda(\mu_i)}{I_\lambda(1)} = 1 - \sum_{i=1}^{4} a_{n,\lambda}(1 - \mu_i^{n/2}) \tag{5.3.3}$$

with $\mu_i = \sqrt{1 - r_i^2}$ and $a_{n,\lambda}$ the four LDCs. Here, we neglected the dependence of the limb darkening effect on the temperature and we assumed the same LDCs (the same from Edwards, Quentin Changeat, et al. 2021) for the spots and the photosphere. This model identifies the spot with 3 parameters: d, R_s and T_s. Using as fitting algorithm the MCMC code emcee with the same methodology of Cracchiolo, G. Micela, Morello, et al. 2021 we obtained as a result the fit showed in Figure 5.5. Comparing the results of the model corresponding to a different composition of the star and the results of the model involving spot presence (Active Star in Figure 5.5) it is clear that the second one has a standard deviation

much higher than the first one and a clear chromaticity of the residuals. Furthermore, the results of the fit accounting for the stellar activity suggest the presence of a big spot, with $R_s \sim 0.57\,R_\star$, results not compatible with the results of Riccardo Spinelli et al. 2023 which found a low level of activity for LHS 1140.
As a consequence, we are quite confident that the spectral modulation studied by Edwards, Quentin Changeat, et al. 2021 is due to the planetary atmosphere without relevant stellar activity contamination. Our results also suggests that stellar composition must be considered in analysis of exoplanetary transmission spectra.

5.4 Stellar Population Membership

Low metallicity values and α-element enrichment are typical of old stars of the thick disk (compatible with the estimated age of this star $>$ 5 billion years, R. Spinelli et al. 2019). We, therefore, analyzed the kinematics of the target to determine its kinematics age. Galactic-spatial velocity components (U, V, W) were computed using Gaia DR3 (Gaia Collaboration et al. 2023) proper motions, parallax and radial velocities by using the methodology described in Maldonado, Martínez-Arnáiz, et al. 2010; Maldonado, G. Micela, et al. 2020. The derived values are $U = 4.38 \pm 0.04\,\mathrm{km\,s^{-1}}$, $V = -49.52 \pm 0.09\,\mathrm{km\,s^{-1}}$ and $W = 4.2 \pm 0.4\,\mathrm{km\,s^{-1}}$, while the corresponding Toomre diagram is shown in Figure 5.7. To classify the star as belonging to the thin/thick disc population, we made use of the procedure described by Bensby, Feltzing, and Lundström 2003; Bensby, Feltzing, Lundström, and Ilyin 2005. We found that LHS1140 shows a kinematics compatible with an old thin disk star, populating the most external thin disk region of the Toomre diagram (Figure 5.7). However, the kinematics criterion is a statistical one and alone is not enough to classify an individual star as a member of the thick or thin disk population.

In order to further clarify the chemical composition of LHS 1140, we analyzed the available HARPS high-resolution optical spectra of this star. We use the methodology developed in Maldonado, G. Micela, et al. 2020 which is based on the use of principal component analysis and sparse Bayesian methods and is calibrated using M dwarfs in binary systems around an FGK primary. We derived a metallicity value of [Fe/H] = -0.38 dex, thus, confirming that LHS 1140 is a metal poor star. Moreover, we find that α elements show higher abundances

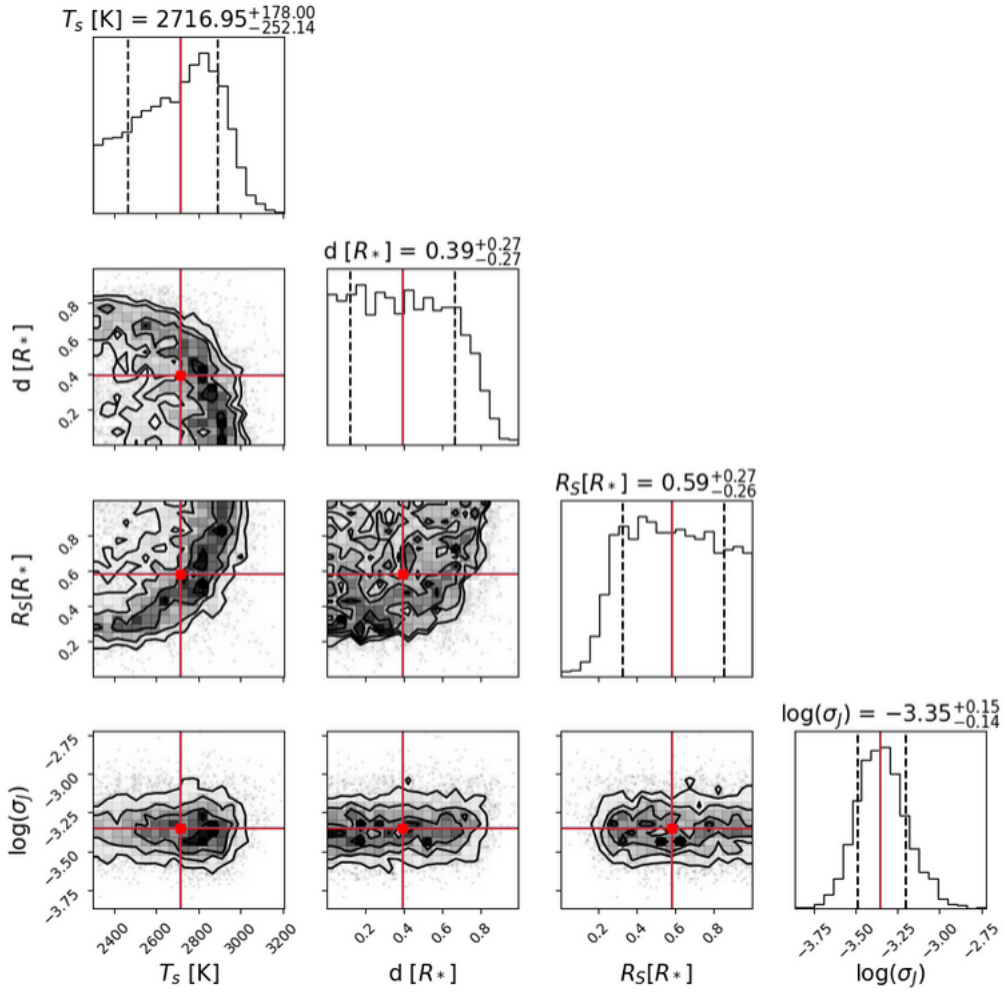

Figure 5.6: Corner plot of the best-fit parameters obtained from the fitting of n^{scan} in forward model using a one spot model for stellar activity simulations. T_s is the temperature of the spot, d is the distance between the center of the spot and the center of the stellar disk. R_s is the radius of the spot normalized to the stellar radius $R_\star$ and σ_j is the jitter noise. The red lines correspond to the values of maximum probability (MAP) for the fit and the dotted lines delimit their confidence interval.

([Mg/H] = 0.01 dex, [Si/H] = -0.15 dex, [Ca/H] = -0.10 dex). We should caution to use quantitative results from Maldonado, G. Micela, et al. 2020 since it might not be optimal for metal poor stars, as the number of "training" stars in this region of metallicities is rather low. However also this analysis points toward a poor metal star with enhanced α elements, that cannot be properly described by assuming solar-like atmospheric composition models.

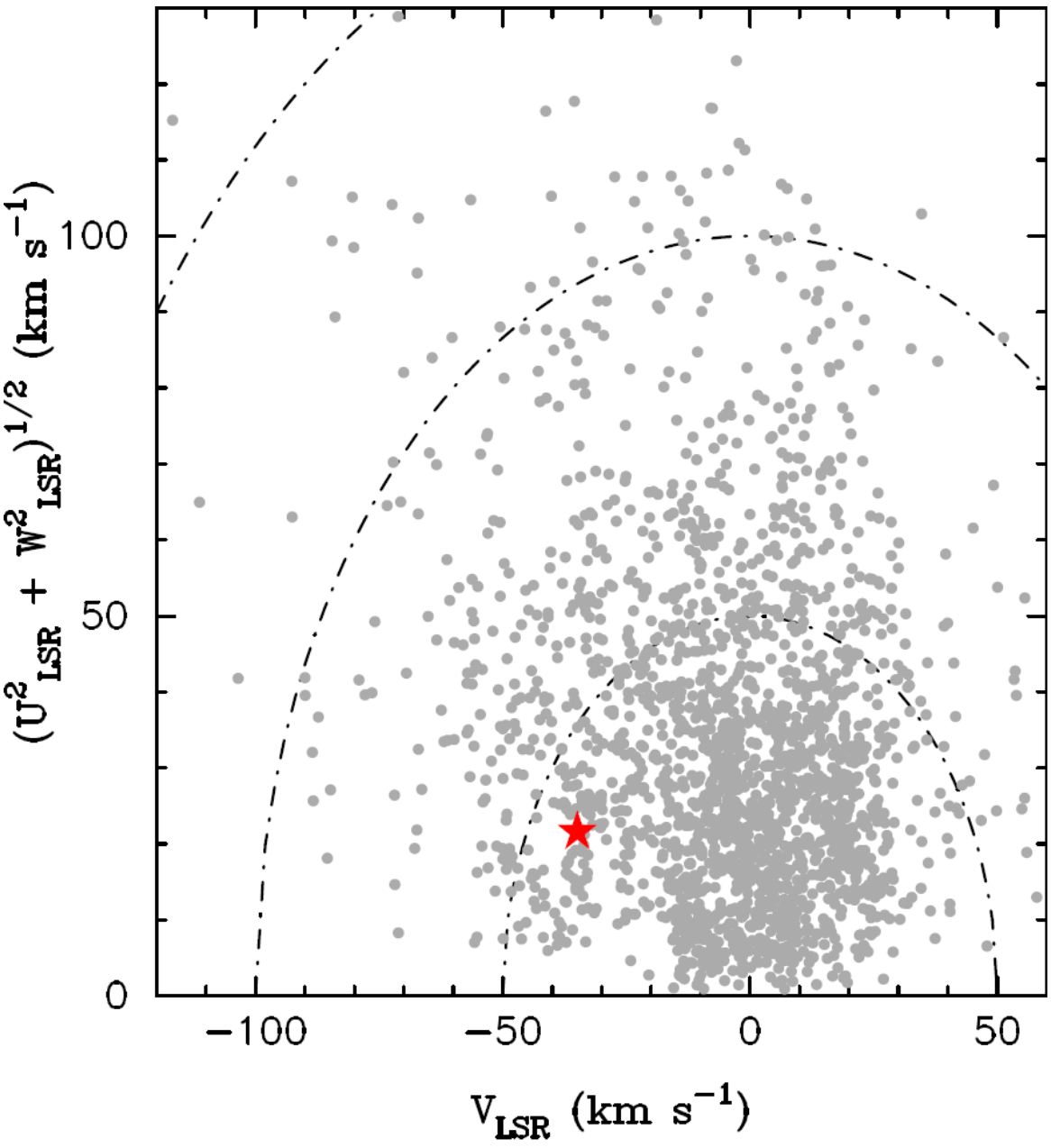

Figure 5.7: Toomre diagram for the stellar neighborhood of LHS 1140 (shown as a red symbol in image). Dotted lines indicate constant peculiar space velocities, $v_{pec} = (U^2_{LSR} + V_{LSR^2} + W^2_{LSR})^{1/2}$ in steps of 50 km s^{-1}, where U_{LSR}, V_{LSR} and W_{LSR} are the velocities of the star with respect to the local standard of rest (LSR).

5.5 Atmospheric Retrieval

Given our new findings regarding the chemical composition of LHS 1140 and the consequent attribution of the features of the in-transit spectrum to the planet, we reviewed the

work of Edwards, Quentin Changeat, et al. 2021 analyzing the planetary spectrum by using the TauREx3 retrieval framework (Al-Refaie et al. 2021) with the same priors of Edwards, Quentin Changeat, et al. 2021 (shown in Tab. 5.3) and a grid of atmospheric parameters with different combinations of H_2O, CH_4, N_2 and clouds as in Table 5.4. Our aim was to

Table 5.3: Priors of TauREx atmospheric retrieval framework used in our work. "V_x" is the volume mixing ratio of the molecular species studied.

Parameter	**Prior Bounds**	**Scale**
V_x	-12, 0	$\log_{10}$
T_{eq}(K)	50, 500	linear
P_{clouds}(Pa)	-4, 6	$\log_{10}$
$R_p(R_{jup})$	0.123, 0.185	linear
He/H_2	0.172	fixed
N_2/H_2	0.2	fixed

confirm the results of Edwards, Quentin Changeat, et al. 2021 using the updated values for the planetary mass and radius from Cadieux et al. 2023, because the mass in particular can have a relevant impact in atmospheric retrievals (Di Maio, Q. Changeat, et al. 2023). We wanted also to expand the number of combinations of H_2O, CH_4, N_2 and clouds in the simulated atmosphere, including also the flat case of an atmosphere without any relevant molecular contribution in the planetary spectrum for reference. To efficiently explore the parameter space, we used TauREx3 with the MultiNest optimizer, employing 3000 live points to enhance fitting precision. In our retrieval procedure we used the molecular cross-sections of H_2O and CH_4 taken from Polyansky et al. 2018 and Yurchenko et al. 2017 respectively. Finally, we took into account collision-induced-absorption (CIA) due to $H_2 - H_2$ (Abel et al. 2011; Fletcher, Gustafsson, and Orton 2018) and to $H_2 - He$ and also Rayleigh scattering for all the molecules in the atmosphere.

Following the criterion illustrated in Kass and Raftery 1995, bayesian evidence does not allow us to identify any specific atmospheric composition, probably because of the wavelength range and low resolution of our data that do not allow us to distinguish the bands of the specific molecules. However, the bayesian evidence suggests that the hypothesis of a flat

atmosphere can be rejected and led to a slightly higher probability for H_2O comprehensive scenarios (Table 5.4) with respect to CH_4 rich atmosphere. The corner plot corresponding to the best fit is shown in Figure 5.8. Figure 5.9 instead shows the comparison between the observed HST data and the two most extreme scenarios that we simulated: H_2O dominated and CH_4-dominated atmosphere, without cloud contributions. It is clear from the figure that, despite some small differences, both curves are similar and hard to distinguish.

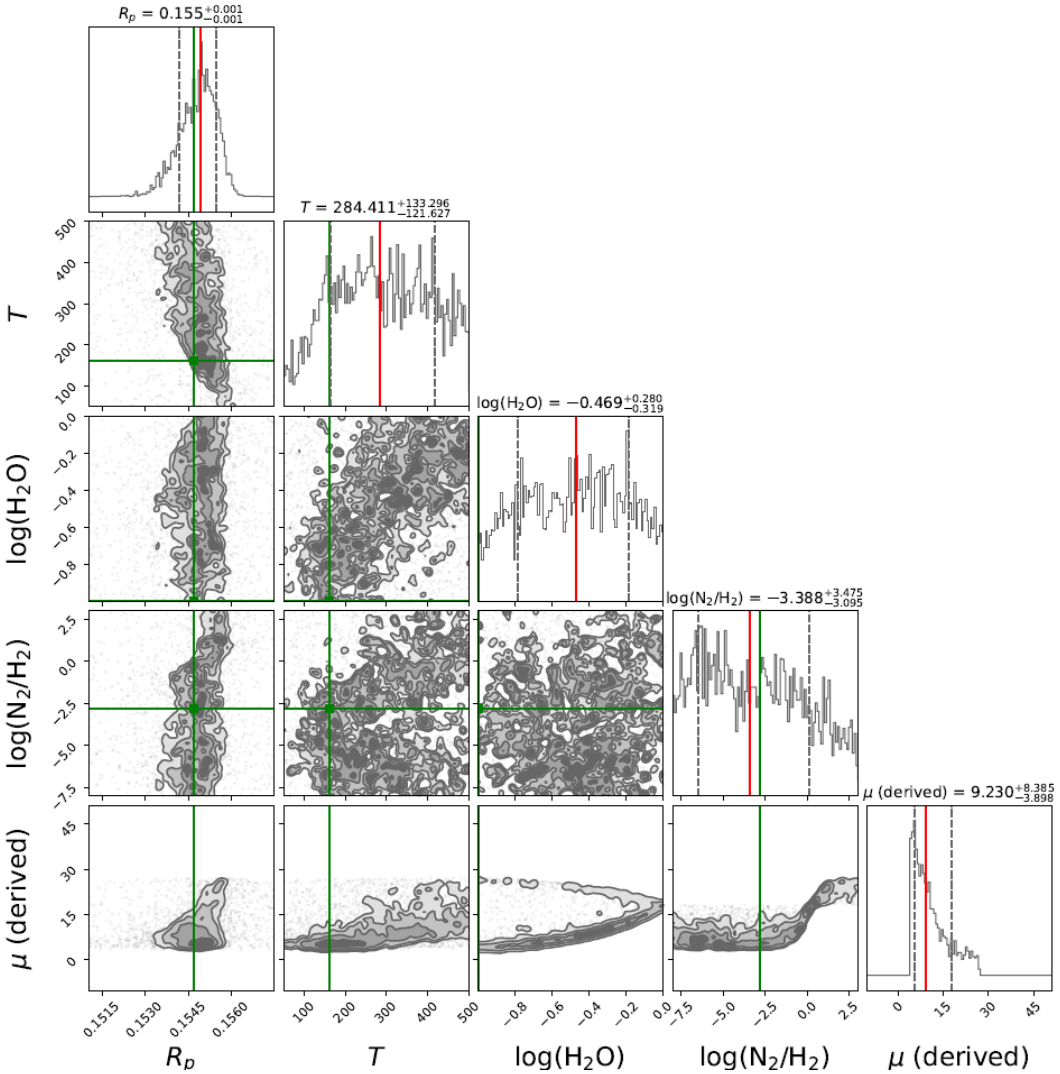

Figure 5.8: Retrieval results obtained for best atmospheric model, corresponding to an atmosphere with N_2, H_2O and without clouds. The green and red vertical solid lines highlight the maximum a posterior (MAP) and median values, respectively, while the vertical dashed-lines represent the values at 1σ from the median.

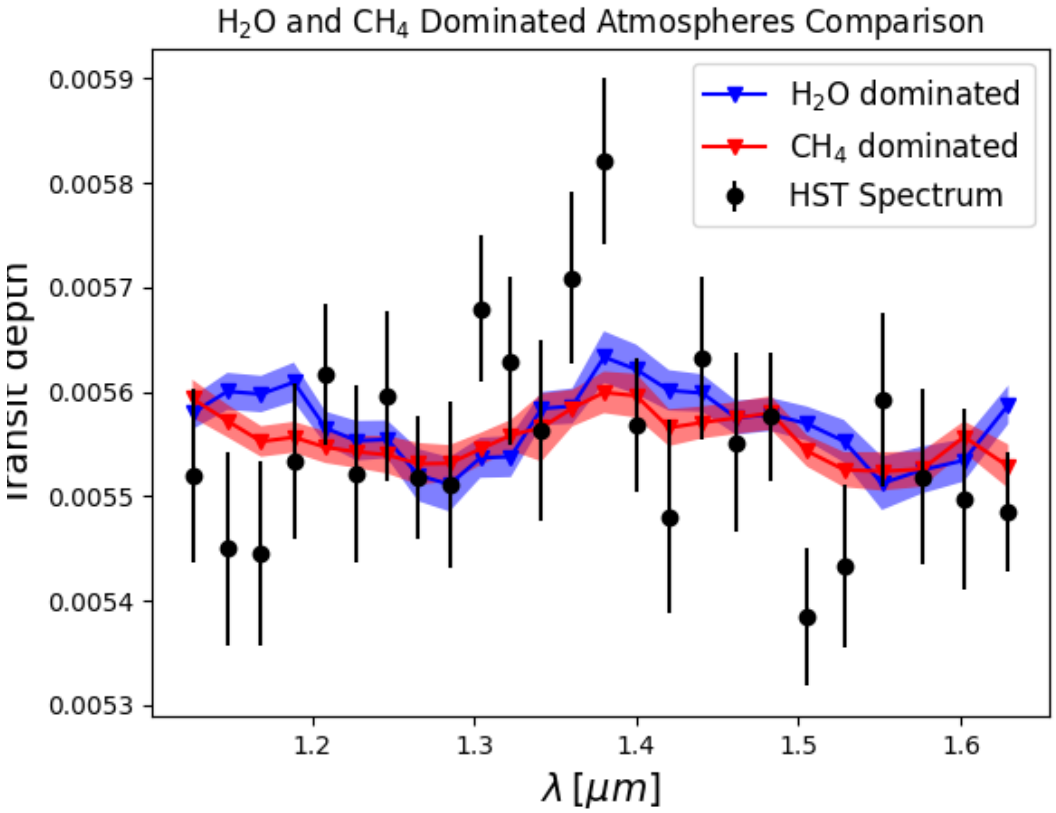

Figure 5.9: Comparison between the observed planetary spectrum (black dots) and the best fit for a secondary atmosphere dominated by H_2O (blue) and one dominated by CH_4 (red), without clouds. The green line represents the flat model.

5.6 Conclusions

LHS 1140 b is a planet close to the HZ of its host star. Previous studies (e.g. Edwards, Quentin Changeat, et al. 2021) analyzed its atmosphere, suggesting the presence of water, but couldn't rule out the possibility that the modulation of the in-transit spectrum could be due to stellar activity contamination.

In this work, we found that the out-of-transit spectra of LHS 1140 during HST observations can be explained by a quiet, inactive star, with low [Fe/H] and high α abundances, so the difference between the in- and -out transit spectra can be entirely attributed to the LHS 1140 b planet atmosphere. Therefore, we are confident that the derived planetary spectrum (retrieved using Iraclis) is not contaminated by a significant stellar contribution and that any spectral feature presented does indeed reflect the planetary atmosphere of LHS 1140 b.

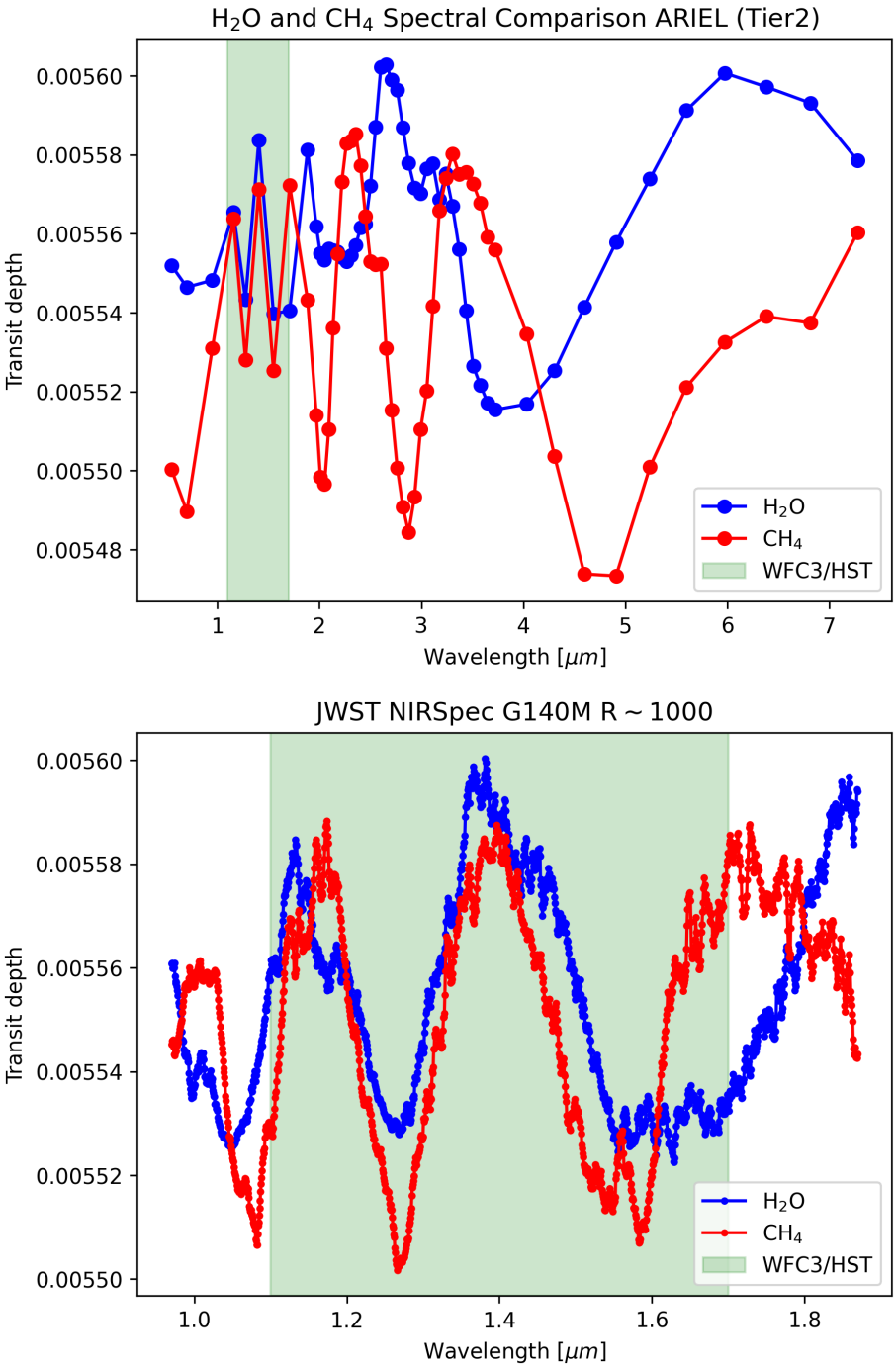

Figure 5.10: Comparison between the expected transit spectrum of LHS 1140 b with an atmosphere enriched in H_2O or CH_4, the same scenarios shown in Figure as observed by Ariel tier 2 (top) and JWST Nirspec with medium resolution G140M grism (bottom). The spectral range of WFC3/HST is shown by the green area.

A proper evaluation of the atmospheric composition of LHS 1140 b will therefore require additional observations, as example with JWST or the upcoming Ariel mission, with higher spectral resolution or broader band coverage. In particular, we simulated the atmospheric signal of LHS 1140 b during a transit as observed with Ariel tier 2, obtained through ArielRad (L. Mugnai et al. 2019) and we did the same also for JWST Nirspec (Jakobsen et al. 2022) with G140M grism, using PandEXo (Batalha et al. 2017) to simulate the expected observed flux for this target. Figure 5.10 shows the results of these simulations, that is, the comparison between the simulated atmosphere of LHS 1140 b with the same scenarios analyzed in Figure 5.9. It can be seen that the difference between both cases is quite clear, and therefore detectable, especially through ARIEL observations, mainly thanks to its long wavelength coverage, thus, allowing us to confirm or rule out the presence of water on the planet and to retrieve its abundance. The challenges in properly modeling the atmosphere of LHS 1140 b using HST WFC3 observations may arise from their low resolution and narrow spectral range, together with a low signal-to-noise. We finally stress the importance of an accurate modelling of the host stellar spectra, not limited to stellar activity but including also its chemical composition, when dealing with suspect features in the retrieved in-transit spectra.

Table 5.4: Fit corresponding to the many models tried to fit the planetary spectrum. We use a combination of H_2O, CH_4 as active molecules, with and without clouds and scenarios where we impose that H_2O or CH_4 are above 10% of the planetary atmospheres ("H_2O dominated" and CH_4 dominated"). We also show the results obtained from a flat model.Log$\mathcal{Z}$ is the bayesian evidence for each model. T is the temperature retrieved for the planet and R_p its radius. When a parameter is not used in the model, it is labeled as "-". When not specified, the atmospheric fill gases are H and He with a ratio of 0.172, while in other cases N_2 is also present as fill gas and its concentration is fitted.

MODEL	**log** $\mathcal{Z}$	$R_p(R_J)$	**T (K)**	**log**(H_2O)	**log**(CH_4)	**log**(N_2/H_2)	**log** Pclouds
$N_2 - H_2O$ no clouds	195.0	$0.1548^{+0.0006}_{-0.0007}$	289^{+133}_{-121}	$-0.5^{+0.3}_{-0.3}$	-	-3^{+3}_{-3}	-
$N_2 - H_2O$-clouds	194.4	$0.1540^{+0.0009}_{-0.0016}$	312^{+111}_{-122}	$-0.5^{+0.3}_{-0.3}$	-	-4^{+3}_{-2}	$3.6^{+1.4}_{-1.3}$
$N_2 - H_2O - CH_4$ no clouds	193.9	$0.1547^{+0.0006}_{-0.0008}$	276^{+127}_{-113}	$-0.6^{+0.3}_{-0.3}$	$-0.6^{+0.3}_{-0.3}$	-3^{+4}_{-4}	-
$N_2 - H_2O - CH_4$-clouds	193.6	$0.1544^{+0.0007}_{-0.0011}$	285^{+126}_{-134}	$-0.6^{+0.3}_{-0.3}$	$-0.6^{+0.3}_{-0.3}$	-3^{+4}_{-3}	3^{+2}_{-3}
$N_2 - CH_4$-clouds	192.7	$0.153^{+0.001}_{-0.005}$	246^{+163}_{-112}	-	-5^{+3}_{-5}	$-2^{+.3}_{-5}$	2^{+2}_{-5}
$N_2 - CH_4$ no clouds	192.6	$0.1553^{+0.0006}_{-0.0009}$	219^{+200}_{-91}	-	-4^{+2}_{-3}	-1^{+2}_{-5}	-
H_2O dominated no clouds	191.7	$0.1559^{+0.0004}_{-0.0004}$	134^{+57}_{-46}	$-0.6^{+0.4}_{-0.3}$	-	-	-
H_2O no clouds	191.4	$0.1553^{+0.0005}_{-0.0005}$	139^{+52}_{-47}	$-2.7^{+1.5}_{-1.2}$	-	-	-
CH_4 dominated-clouds	191.1	$0.153^{+0.002}_{-0.003}$	274^{+138}_{-136}	-	$-0.5^{+0.4}_{-0.3}$	-	$0.8^{+1.3}_{-1.9}$
H_2O dominated-clouds	191.0	$0.1550^{+0.0006}_{-0.0019}$	176^{+112}_{-62}	$-0.6^{+0.4}_{-0.3}$	-	-	3^{+2}_{-5}
H_2O-clouds	191.0	$0.152^{+0.001}_{-0.009}$	201^{+179}_{-71}	-5^{+2}_{-5}	-	-	2^{+2}_{-5}
CH_4-clouds	191.0	$0.150^{+0.003}_{-0.005}$	259^{+136}_{-129}	-	-5^{+2}_{-5}	-	2^{+2}_{-4}
flat model	190.4	$0.154^{+0.001}_{-0.003}$	267^{+160}_{-145}	-	-	-	-
CH_4 dominated no clouds	189.9	$0.1552^{+0.0007}_{-0.0010}$	226^{+185}_{-107}	-	$-0.3^{+0.1}_{-0.3}$	-	-
CH_4 no clouds	189.5	$0.1551^{+0.0007}_{-0.0007}$	275^{+131}_{-121}	-	$-0.2^{+0.1}_{-0.2}$	-	-

Chapter 6

Papers publication

6.1 Analysis of V1298 Tau

Authors: Biagini, Alfredo; Petralia, Antonino; Di Maio, Claudia; Betti, Lorenzo ; Pace, Emanuele; Micela, Giuseppina

6.1.1 Abstract

Context. Stellar activity consists of different phenomena, mainly spots and faculae, and it is one of the main sources of noise in exoplanetary observations because it affects both spectroscopic and photometric observations. If we want to study young active planetary systems, we need to model the activity of the host stars in order to remove astrophysical noise from our observational data. Aims. We modelled the contribution of stellar spots in photometric observations. Through the use of multiband photometry, we aim to extract the geometric properties of the spots and constrain their temperature. Methods. We analyzed multiband photometric observations acquired with the 80 cm Marcon telescope of the Osservatorio Polifunzionale del Chianti of V1298 Tau, assuming that the photometric modulation observed in different bands should be due to cold spots. Results. We constrained the effective temperature of the active regions present on the surface of V1298 Tau, which is composed by the contemporary presence of spots and faculae. We tested our hypothesis on solar data, verifying that we in fact measure the size of the dominant active region and its averaged effective temperature.

This work is described in chapter 3 and is currently subjected to the referee process.

6.2 Correcting Exoplanet Transmission Spectra for Stellar Activity with an Optimized Retrieval Framework

Authors: Thompson, Alexandra; Biagini, Alfredo; Cracchiolo, Gianluca; Petralia, Antonino; Changeat, Quentin; Saba, Arianna; Morello, Giuseppe; Morvan, Mario; Micela, Giuseppina; Tinetti, Giovanna

Reference: Thompson et al. 2024, ApJ, 960, 107.

6.2.1 Abstract

The chromatic contamination that arises from photospheric heterogeneities, e.g., spots and faculae on the host star, presents a significant noise source for exoplanet transmission spectra. If this contamination is not corrected for, it can introduce substantial bias in our analysis of the planetary atmosphere. We utilize two stellar models of differing complexity, StARPA (Stellar Activity Removal for Planetary Atmospheres) and ASteRA (Active Stellar Retrieval Algorithm), to explore the biases introduced by stellar contamination in retrieval under differing degrees of stellar activity. We use the retrieval framework TauREx3 and a grid of 27 synthetic, spot-contaminated transmission spectra to investigate potential biases and to determine how complex our stellar models must be in order to accurately extract the planetary parameters from transmission spectra. The input observation is generated using the more complex model (StARPA), in which the spot latitude is an additional, fixable parameter. This observation is then fed into a combined stellar-planetary retrieval, which contains a simplified stellar model (ASteRA). Our results confirm that the inclusion of stellar activity parameters in retrieval minimizes bias under all activity regimes considered. ASteRA performs very well under low-to-moderate activity conditions, retrieving the planetary parameters with a high degree of accuracy. For the most active cases, characterized by larger, higher-temperature contrast spots, some minor residual bias remains due to ASteRA neglecting the interplay between the spot and the limb-darkening effect. As a result of this, we find larger errors in retrieved planetary parameters for central spots (0 deg) and those found close to the limb (60 deg) than those at intermediate latitudes (30 deg).

This paper is described in chapter 4.

6.3 A reanalysis of the LHS 1140 b atmosphere

Authors: Biagini, Alfredo; Cracchiolo, Gianluca; Petralia, Antonino; Maldonado, Jesús; Di Maio, Claudia; Micela, Giuseppina

Reference: Biagini et al. 2024, MNRAS, 530, 1054.

6.3.1 Abstract

The super-Earth LHS 1140 b is an interesting target for atmospheric observations since it is close to the habitable zone of its star and falls in the gap of the radius distribution of small exoplanets, in the region thought to correspond to the transition between planets with and without atmospheres. Observations of the primary transit with WFC3 onboard of the Hubble Space Telescope (HST) revealed a modulation in the planet transmission spectrum compatible with the presence of water; however, this modulation may be also due to stellar activity-related phenomena. Here, we present a detailed analysis of the WFC3/HST observations to probe the nature of this modulation and to understand if it can be attributable to the presence of unocculted spots on the stellar surface. Our analysis strongly suggests that LHS1140 is a rather quiet star with subsolar [Fe/H] and enriched in α elements. Therefore, we rule out the possibility that the planetary spectrum is affected by the presence of spots and faculae. This analysis shows the importance of a proper modelling of the stellar spectrum when analyzing transit observations. Finally, we modelled the planetary atmosphere of LHS1140 b to retrieve its atmospheric composition. However, the low resolution and the narrow spectral range of HST observations prevented us from definitively determining whether the spectral features are attributable to the presence of water or of other molecules in the planetary atmosphere.

This paper is described in chapter 5.

Chapter 7

Conclusions

In this thesis, we studied if and how stellar activity can be modeled and taken into account to extract the planet signal in an unbiased way. In fact, stellar activity is the main source of astrophysical noise for planetary observations and cannot be neglected, especially in atmospheric observations that require high accurate analysis. As a first step, we studied an extreme active and young star, V1298 Tau, through simultaneous multiband photometry to test the possibility of constraining the spots/faculae parameters, thanks to their different chromatic thermal emission (lower for spots, higher for faculae) with respect to quiet photosphere. The method uses a bayesan approach that calculates bayesian evidence associated to the estimated parameters to fit the data to a simple stellar model, including a quiet photosphere and up to four spots responsible for the chromatic modulation observed. The analysis has been applied to different observation runs, obtaining different spot temperatures. The proposed explanation was that the retrieved spot temperature is a sort of average of the temperatures of the spots and faculae present on the stars. The change of the derived temperature then can be related to a variation of the ratio between faculae and spot areas. A clue of a such evolution was found in spectroscopic data from HARPS-N showing evolution of the ratio between emission in CaII and Hα lines. To further strengthen the results, we tested the approach on solar multiband photometric data, exploiting the possibility to compare the photometry results with contemporaneous actual images of the solar spots. The procedure was able to correctly locate the dominant solar active region, including various small spots and faculae, supporting the hypothesis that the applied procedure retrieves the global properties of the entire active region.

Having verified the possibility to retrieve mean properties of the stellar active regions

and then to model the star, in chapter 4, we tested how this modeling can help to correct in-transit planetary spectra affected by stellar activity. To this goal, we developed a new tool (STARPA) to simulate and retrieve stellar activity effects on in-transit planetary spectra (especially useful for future Ariel observations), as an updated version of the method developed by Cracchiolo, G. Micela, and Peres 2021 and Cracchiolo, G. Micela, Morello, et al. 2021 for mean spots parameters retrieval in spectroscopic analysis. Using STARPA, we simulated several different spots-faculae configurations, to test the retrieval method and to analyze the impact of the use of stellar activity models for in-transit spectrum correction in atmospheric retrievals and in H_2O detection. We performed the analysis on a simulated sub-Netptune planet orbiting a K and an M dwarf. We demonstrated the capability of the method to correctly retrieve the equilibrium temperature and to detect (and measure) H_2O in the planet atmosphere after planetary spectrum correction, even in cases with high stellar activity, though with higher scattering in presence of big spots and in M dwarf case.

Finally, in chapter 5, we analyzed the case of the transiting planet LHS 1140 b looking for clues of stellar activity in low resolution HST-WFC3 data to verify the plausibility of H_2O detection by Edwards, Quentin Changeat, et al. 2021. Analyzing the out-of-transit spectrum of the star, we found no indication of stellar activity, instead signatures of a non-solar composition of the star that risked being confused for stellar activity signals. This work confirmed the H_2O detection on the planet without the needs to invoke the role of stellar activity. We finally tested through simulations the possibility of JWST and incoming ARIEL mission to characterize the atmosphere of this planet finding that the wide spectral range of ARIEL should allow us to better constrain its chemistry, especially distinguishing the contribution of methane from that of water. This last case stresses the importance of a very accurate knowledge of the host star, when analyzing the planetary properties.

In conclusion, we have developed a roadmap to derive the planetary atmospheric parameters, including an accurate modeling of the stellar activity and in general of the star, using the out-of-transit spectrum, allowing a correct extraction of the planetary spectrum during a transit.

The developed model open a number of future possibilities. In particular, we aim to combine simultaneous study of spectral and multiband photometrical data to retrieve with higher precision the characteristics of spots and faculae in active stars. With this goal in

mind, we obtained simultaneous observations from HARPS-N (high resolution spectroscopy) at TNG during AOT48 period and REM telescope (multiband photometry) for 3 active stars. Another possibility is to extend STARPA model to spot-crossing transits to develop a more global spectral correction method for spectral transits observations. Finally, given the results obtained on V1298 Tau, we are planning new multiband photometric observations of V1298 Tau star with better temporal coverage in order to study its activity with a higher level of precision in order to disentangle contributions from spots and faculae.

Appendix A

Observing proposals

During this PhD work two observing proposals were submitted and accepted:

- Infrared and optical observations of active stars, AOT45 for REM telescope
- Spectroscopic counterpart of photometrical observations of Active Stars, AOT48 for REM telescope and HARPS-N.

one for AOT45 and one for AOT48.

Gal-Hassin observatory also observed for 5 nights the young active star TOI-5398 and the transit of its planet b Mantovan et al. 2024 in g', r' and z' Sloan bands. The aim was to characterize the activity of this target through multiband photometric observations in order to correct the observation of the transit and study the planet and its ephemerids.

All these data will be analyzed with the spots-faculae retrieval method described in chapter 3 after its publication.

A.1 Infrared and optical observations of active stars

This proposal's goal was to measure the absolute photometric variations in both optical and IR bands for V1298 Tau and DS Tucanae A, two active stars, using TYC 1258-8-1 and UCAC4 104-113995 as known reference stars to calculate the absolute flux of the targets. The measures lasted 3 periods of rotations of the stars (about 9 days in total) to evaluate spots evolution on these targets. The proposal also involved the differential photometric study of the active star TOI-179 without the need of a reference standard field or star. This choice was due to the longer period of rotation of this star, about 5 days. The observations

were performed using both ROS2 and REMIR detectors of REM telescope (described in chapter 2).

A.2 Spectroscopic counterpart of photometrical observations of Active Stars.

The aim of this proposal was to verify, through H alpha and Ca II H-K lines observations, the hypothesis of chapter 3 about the correspondence between the change in the effective temperature of the active regions of the stars and the change in their faculae-spots ratio. Specifically, we wanted to measure the correlation between the change of $\log R'_{HK}$ ratio and the spot filling factor and temperature retrieved through multiband differential photometry in IR and optical bands, with the procedure described in chapter 3.

Our targets were HD 70573, AD Leonis and TYC 5909319-1. The three stars were selected for their high level of activity, for their high v sin i value to use the method developed by Di Maio, Petralia, et al. 2024 for spots analysis through CCF and finally for their position in the sky that allows contemporary observations from TNG and La Silla observatory. In fact, our method requires both multiband photometric observations in both optical and IR bands from REM telescopes and spectra from HARPS-N at least during a period of rotations observed photometrically.

Appendix B

Photometric data

In table B.1 and B.2 we show V1298 Tau flux variation amplitudes in different filters measured by Gal-Hassin and REM telescopes respectively. Because these data are not used in spot retrieval, due to their low SNR, flux variations amplitude were estimated through a simple fit performed using python-scipy package "$curve - fit$" function (Newville et al. 2014) In Figure B.1 we show a comparison of simultaneous observations from OPC and Gal-Hassin, where the stellar light-curves are shifted for clarity purpose. Finally, in Figure B.2 I show V1298 Tau light-curves in different filters as measured by REM telescope in December 2021 observations. It's clear the decrease in amplitude of stellar flux variations at longer wavelengths, due to the thermal contrast between spots/faculae and quiet photosphere.

Table B.1: Amplitude of flux variations of V1298 Tau as measured from Gal-Hassin in different photometric bands.

Gal-Hassin	r'	g'	z'	H alpha
02/2021	0.015 ± 0.009	/	/	0.033 ± 0.015
09/2022	0.002 ± 0.003	0.004 ± 0.003	0.005 ± 0.005	0.048 ± 0.011

Table B.2: Amplitude of flux variations of V1298 Tau as measured from REM telescope in different photometric bands.

REM	r'	g'	i'	z'	J
12/2021	0.042 ± 0.009	0.040 ± 0.008	0.033 ± 0.006	0.017 ± 0.006	0.021 ± 0.006
09/2022	0.018 ± 0.001	0.011 ± 0.001	0.011 ± 0.001	0.009 ± 0.001	0.007 ± 0.003

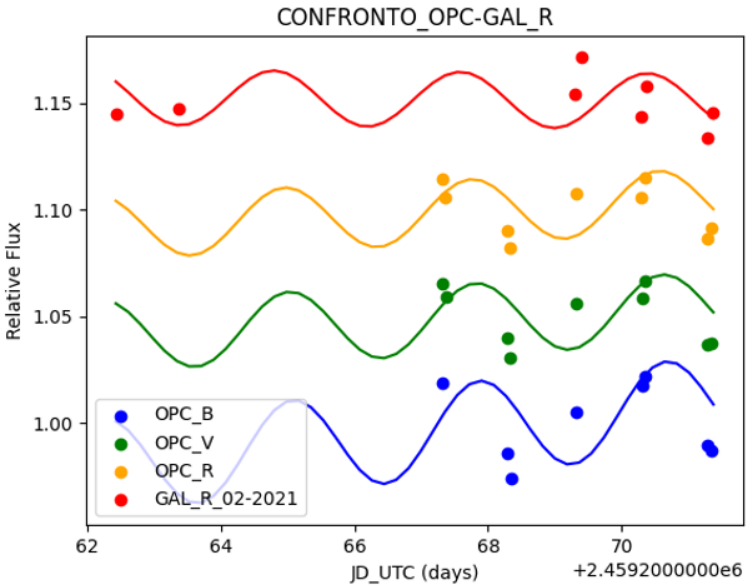

Figure B.1: Data and fitted light-curve of V1298 Tau observed in February 2021 by Gal-Hassin and OPC simultaneously. Lightcurves are shifted for clarity purpose.

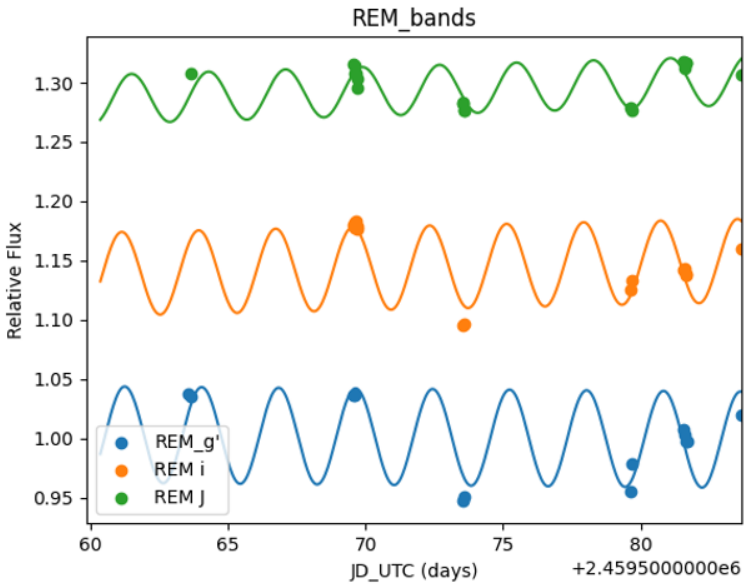

Figure B.2: Data and fitted light-curve of V1298 Tau observed in December 2021 by REM telescope. It's clear a reduction of stellar flux variations amplitude at longer wavelengths. Lightcurves are shifted for clarity purpose.

Appendix C

Atmospheric simulations' results

Here we show the complete results of atmospheric retrievals described in Chapter 3 for both K (Table C.1) and M (Table C.2) dwarf cases.

Table C.1: List of atmospheric and planetary parameters retrieved for each case analyzed for K dwarf star.

Case	$\mathrm{ff_{spot}}$	$\mathrm{ff_{fac}}$	**Rplanet (Rj)**	**T (K)**	**log mixH2O**	**Spot crossing**
0	0.0	0.0	$0.273^{+0.001}_{-0.001}$	1047^{+42}_{-41}	$-3.21^{+0.23}_{-0.21}$	no
1	0.0	0.001	$0.273^{+0.001}_{-0.001}$	1046^{+45}_{-40}	$-3.2^{+0.24}_{-0.2}$	no
2	0.0	0.007	$0.273^{+0.001}_{-0.001}$	1049^{+44}_{-40}	$-3.22^{+0.22}_{-0.21}$	no
3	0.022	0.0	$0.273^{+0.001}_{-0.001}$	1049^{+42}_{-38}	$-3.14^{+0.22}_{-0.2}$	no
4	0.022	0.003	$0.273^{+0.001}_{-0.001}$	1061^{+41}_{-40}	$-3.16^{+0.22}_{-0.21}$	no
5	0.022	0.018	$0.273^{+0.001}_{-0.001}$	1061^{+41}_{-39}	$-3.16^{+0.23}_{-0.2}$	no
6	0.089	0.001	$0.273^{+0.001}_{-0.001}$	820^{+33}_{-29}	$-2.42^{+0.25}_{-0.24}$	yes
7	0.089	0.006	$0.273^{+0.001}_{-0.001}$	851^{+36}_{-31}	$-2.5^{+0.22}_{-0.22}$	yes
8	0.089	0.032	$0.272^{+0.001}_{-0.001}$	980^{+31}_{-33}	$-2.8^{+0.21}_{-0.2}$	yes
9	0.023	0.0	$0.273^{+0.001}_{-0.001}$	1049^{+40}_{-38}	$-3.14^{+0.22}_{-0.2}$	no
10	0.023	0.003	$0.273^{+0.001}_{-0.001}$	1060^{+41}_{-40}	$-3.15^{+0.22}_{-0.2}$	no
11	0.023	0.018	$0.273^{+0.001}_{-0.001}$	1022^{+44}_{-37}	$-3.09^{+0.23}_{-0.23}$	no
12	0.038	0.0	$0.272^{+0.001}_{-0.001}$	1052^{+41}_{-39}	$-3.09^{+0.22}_{-0.21}$	no
13	0.038	0.004	$0.272^{+0.001}_{-0.001}$	1069^{+38}_{-40}	$-3.13^{+0.21}_{-0.19}$	no

14	0.038	0.023	$0.273^{+0.001}_{-0.001}$	1000^{+37}_{-36}	$-3.0^{+0.22}_{-0.22}$	no
15	0.09	0.001	$0.273^{+0.001}_{-0.001}$	817^{+32}_{-29}	$-2.4^{+0.23}_{-0.23}$	yes
16	0.09	0.006	$0.273^{+0.001}_{-0.001}$	843^{+35}_{-29}	$-2.48^{+0.23}_{-0.23}$	yes
17	0.09	0.032	$0.273^{+0.001}_{-0.001}$	920^{+36}_{-33}	$-2.68^{+0.21}_{-0.22}$	yes
18	0.09	0.001	$0.259^{+0.001}_{-0.001}$	1459^{+18}_{-18}	$-1.52^{+0.07}_{-0.07}$	yes
19	0.09	0.006	$0.263^{+0.001}_{-0.001}$	1341^{+17}_{-18}	$-3.67^{+0.19}_{-0.12}$	yes
20	0.09	0.032	$0.26^{+0.001}_{-0.001}$	1432^{+11}_{-15}	$-1.68^{+0.06}_{-0.12}$	yes
21	0.091	0.001	$0.26^{+0.001}_{-0.001}$	1366^{+12}_{-9}	$-1.62^{+0.07}_{-0.04}$	yes
22	0.091	0.006	$0.259^{+0.001}_{-0.001}$	1457^{+17}_{-18}	$-1.54^{+0.07}_{-0.07}$	yes
23	0.091	0.033	$0.264^{+0.001}_{-0.001}$	1267^{+9}_{-13}	$-3.53^{+0.08}_{-0.08}$	yes
24	0.121	0.001	$0.26^{+0.001}_{-0.001}$	1458^{+19}_{-19}	$-1.12^{+0.05}_{-0.06}$	yes
25	0.121	0.007	$0.261^{+0.001}_{-0.001}$	1362^{+6}_{-9}	$-1.24^{+0.02}_{-0.01}$	yes
26	0.121	0.037	$0.261^{+0.001}_{-0.001}$	1440^{+16}_{-14}	$-1.3^{+0.04}_{-0.04}$	yes
27	0.0	0.0	$0.273^{+0.001}_{-0.001}$	1046^{+41}_{-41}	$-3.21^{+0.2}_{-0.22}$	no
28	0.0	0.001	$0.273^{+0.001}_{-0.001}$	1047^{+42}_{-42}	$-3.2^{+0.23}_{-0.21}$	no
29	0.0	0.006	$0.273^{+0.001}_{-0.001}$	1049^{+44}_{-41}	$-3.22^{+0.23}_{-0.22}$	no
30	0.017	0.0	$0.273^{+0.001}_{-0.001}$	1033^{+45}_{-41}	$-3.16^{+0.23}_{-0.23}$	no
31	0.017	0.003	$0.273^{+0.001}_{-0.001}$	1038^{+44}_{-40}	$-3.17^{+0.22}_{-0.22}$	no
32	0.017	0.017	$0.272^{+0.001}_{-0.001}$	1107^{+42}_{-39}	$-3.26^{+0.21}_{-0.2}$	no
33	0.069	0.001	$0.273^{+0.001}_{-0.001}$	1005^{+40}_{-39}	$-3.04^{+0.23}_{-0.23}$	yes
34	0.069	0.005	$0.273^{+0.001}_{-0.001}$	1012^{+46}_{-37}	$-3.06^{+0.23}_{-0.24}$	yes
35	0.069	0.028	$0.273^{+0.001}_{-0.001}$	1061^{+38}_{-41}	$-3.17^{+0.24}_{-0.21}$	yes
36	0.023	0.0	$0.273^{+0.001}_{-0.001}$	1050^{+41}_{-39}	$-3.14^{+0.23}_{-0.2}$	no
37	0.023	0.003	$0.273^{+0.001}_{-0.001}$	1060^{+42}_{-38}	$-3.15^{+0.22}_{-0.22}$	no
38	0.023	0.02	$0.273^{+0.001}_{-0.001}$	1043^{+44}_{-40}	$-3.13^{+0.24}_{-0.21}$	no
39	0.04	0.001	$0.272^{+0.001}_{-0.001}$	1067^{+40}_{-38}	$-3.14^{+0.21}_{-0.2}$	no

40	0.04	0.006	$0.273^{+0.001}_{-0.001}$	999^{+43}_{-40}	$-3.01^{+0.23}_{-0.24}$	no
41	0.04	0.031	$0.273^{+0.001}_{-0.001}$	1063^{+39}_{-42}	$-3.14^{+0.23}_{-0.2}$	no
42	0.091	0.001	$0.273^{+0.001}_{-0.001}$	964^{+37}_{-37}	$-2.87^{+0.23}_{-0.22}$	yes
43	0.091	0.008	$0.273^{+0.001}_{-0.001}$	975^{+35}_{-36}	$-2.89^{+0.22}_{-0.24}$	yes
44	0.091	0.042	$0.273^{+0.001}_{-0.001}$	1029^{+44}_{-38}	$-3.04^{+0.24}_{-0.24}$	yes
45	0.09	0.001	$0.259^{+0.001}_{-0.001}$	1428^{+6}_{-7}	$-1.58^{+0.06}_{-0.06}$	yes
46	0.09	0.006	$0.263^{+0.001}_{-0.001}$	1434^{+10}_{-11}	$-3.98^{+0.05}_{-0.08}$	yes
47	0.09	0.035	$0.264^{+0.001}_{-0.001}$	1353^{+17}_{-14}	$-3.71^{+0.09}_{-0.09}$	yes
48	0.107	0.001	$0.259^{+0.001}_{-0.001}$	1462^{+18}_{-19}	$-1.37^{+0.06}_{-0.06}$	yes
49	0.107	0.009	$0.259^{+0.001}_{-0.001}$	1459^{+18}_{-20}	$-1.43^{+0.06}_{-0.07}$	yes
50	0.107	0.046	$0.264^{+0.001}_{-0.001}$	1437^{+15}_{-16}	$-3.94^{+0.08}_{-0.08}$	yes
51	0.159	0.001	$0.262^{+0.001}_{-0.001}$	1433^{+9}_{-13}	$-0.94^{+0.03}_{-0.03}$	yes
52	0.159	0.011	$0.261^{+0.001}_{-0.001}$	1469^{+18}_{-23}	$-0.97^{+0.04}_{-0.05}$	yes
53	0.159	0.057	$0.261^{+0.001}_{-0.001}$	1448^{+18}_{-19}	$-1.34^{+0.04}_{-0.05}$	yes
54	0.0	0.0	$0.273^{+0.001}_{-0.001}$	1046^{+45}_{-44}	$-3.21^{+0.25}_{-0.2}$	no
55	0.0	0.0	$0.273^{+0.001}_{-0.001}$	1047^{+42}_{-41}	$-3.21^{+0.22}_{-0.21}$	no
56	0.0	0.005	$0.273^{+0.001}_{-0.001}$	1046^{+42}_{-42}	$-3.2^{+0.23}_{-0.22}$	no
57	0.008	0.0	$0.273^{+0.001}_{-0.001}$	1065^{+40}_{-43}	$-3.27^{+0.23}_{-0.2}$	no
58	0.008	0.001	$0.273^{+0.001}_{-0.001}$	1071^{+42}_{-41}	$-3.28^{+0.22}_{-0.2}$	no
59	0.008	0.01	$0.273^{+0.001}_{-0.001}$	1107^{+47}_{-43}	$-3.32^{+0.22}_{-0.23}$	no
60	0.031	0.0	$0.273^{+0.001}_{-0.001}$	1103^{+48}_{-45}	$-3.41^{+0.22}_{-0.21}$	yes
61	0.031	0.002	$0.273^{+0.001}_{-0.001}$	1116^{+50}_{-42}	$-3.44^{+0.22}_{-0.22}$	yes
62	0.031	0.015	$0.272^{+0.001}_{-0.001}$	1172^{+41}_{-45}	$-3.47^{+0.22}_{-0.19}$	yes
63	0.023	0.0	$0.273^{+0.001}_{-0.001}$	1050^{+43}_{-39}	$-3.14^{+0.24}_{-0.21}$	no
64	0.023	0.003	$0.273^{+0.001}_{-0.001}$	1060^{+42}_{-39}	$-3.15^{+0.21}_{-0.21}$	no
65	0.023	0.019	$0.273^{+0.001}_{-0.001}$	1032^{+44}_{-38}	$-3.11^{+0.22}_{-0.22}$	no

66	0.03	0.0	$0.273^{+0.001}_{-0.001}$	1069^{+40}_{-38}	$-3.18^{+0.22}_{-0.2}$	no
67	0.03	0.004	$0.273^{+0.001}_{-0.001}$	1020^{+46}_{-41}	$-3.1^{+0.25}_{-0.23}$	no
68	0.03	0.024	$0.273^{+0.001}_{-0.001}$	1060^{+40}_{-42}	$-3.17^{+0.22}_{-0.19}$	no
69	0.053	0.001	$0.273^{+0.001}_{-0.001}$	1052^{+42}_{-46}	$-3.24^{+0.23}_{-0.2}$	yes
70	0.053	0.005	$0.273^{+0.001}_{-0.001}$	1054^{+41}_{-42}	$-3.23^{+0.24}_{-0.22}$	yes
71	0.053	0.029	$0.273^{+0.001}_{-0.001}$	1115^{+48}_{-42}	$-3.32^{+0.22}_{-0.22}$	yes
72	0.09	0.001	$0.259^{+0.001}_{-0.001}$	1460^{+19}_{-18}	$-1.52^{+0.07}_{-0.07}$	yes
73	0.09	0.006	$0.259^{+0.001}_{-0.001}$	1456^{+17}_{-16}	$-1.55^{+0.07}_{-0.08}$	yes
74	0.09	0.034	$0.264^{+0.001}_{-0.001}$	1435^{+14}_{-13}	$-3.97^{+0.07}_{-0.06}$	yes
75	0.098	0.001	$0.26^{+0.001}_{-0.001}$	1367^{+7}_{-9}	$-1.68^{+0.03}_{-0.04}$	yes
76	0.098	0.007	$0.263^{+0.001}_{-0.001}$	1350^{+19}_{-15}	$-3.65^{+0.15}_{-0.14}$	yes
77	0.098	0.039	$0.264^{+0.001}_{-0.001}$	1360^{+14}_{-12}	$-3.69^{+0.08}_{-0.08}$	yes
78	0.121	0.001	$0.263^{+0.001}_{-0.001}$	1359^{+11}_{-11}	$-3.65^{+0.22}_{-0.11}$	yes
79	0.121	0.008	$0.259^{+0.001}_{-0.001}$	1462^{+18}_{-16}	$-1.63^{+0.08}_{-0.08}$	yes
80	0.121	0.044	$0.264^{+0.001}_{-0.001}$	1457^{+22}_{-22}	$-3.86^{+0.14}_{-0.13}$	yes
81	0.0	0.0	$0.273^{+0.001}_{-0.001}$	1046^{+43}_{-43}	$-3.21^{+0.24}_{-0.21}$	no
82	0.0	0.001	$0.273^{+0.001}_{-0.001}$	1047^{+46}_{-41}	$-3.21^{+0.23}_{-0.21}$	no
83	0.0	0.006	$0.273^{+0.001}_{-0.001}$	1050^{+40}_{-42}	$-3.22^{+0.22}_{-0.2}$	no
84	0.022	0.0	$0.273^{+0.001}_{-0.001}$	1051^{+40}_{-40}	$-3.14^{+0.23}_{-0.2}$	no
85	0.022	0.003	$0.273^{+0.001}_{-0.001}$	1060^{+40}_{-37}	$-3.16^{+0.22}_{-0.2}$	no
86	0.022	0.02	$0.272^{+0.001}_{-0.001}$	1088^{+38}_{-41}	$-3.19^{+0.21}_{-0.21}$	no
87	0.089	0.001	$0.273^{+0.001}_{-0.001}$	821^{+33}_{-27}	$-2.42^{+0.21}_{-0.22}$	no
88	0.089	0.006	$0.273^{+0.001}_{-0.001}$	851^{+34}_{-32}	$-2.5^{+0.24}_{-0.23}$	no
89	0.089	0.033	$0.272^{+0.001}_{-0.001}$	979^{+31}_{-36}	$-2.79^{+0.22}_{-0.21}$	no
90	0.02	0.0	$0.273^{+0.001}_{-0.001}$	1056^{+42}_{-39}	$-3.18^{+0.23}_{-0.2}$	no
91	0.02	0.003	$0.273^{+0.001}_{-0.001}$	1026^{+42}_{-40}	$-3.12^{+0.24}_{-0.21}$	no

92	0.02	0.019	$0.272^{+0.001}_{-0.001}$	1102^{+43}_{-43}	$-3.25^{+0.24}_{-0.21}$	no
93	0.042	0.001	$0.272^{+0.001}_{-0.001}$	1067^{+41}_{-37}	$-3.13^{+0.21}_{-0.21}$	no
94	0.042	0.006	$0.272^{+0.001}_{-0.001}$	1079^{+41}_{-38}	$-3.14^{+0.21}_{-0.21}$	no
95	0.042	0.03	$0.272^{+0.001}_{-0.001}$	1072^{+39}_{-39}	$-3.13^{+0.22}_{-0.21}$	no
96	0.102	0.001	$0.273^{+0.001}_{-0.001}$	761^{+29}_{-32}	$-2.22^{+0.21}_{-0.24}$	no
97	0.102	0.007	$0.273^{+0.001}_{-0.001}$	790^{+28}_{-30}	$-2.3^{+0.21}_{-0.23}$	no
98	0.102	0.036	$0.273^{+0.001}_{-0.001}$	933^{+38}_{-31}	$-2.66^{+0.24}_{-0.2}$	no
99	0.078	0.001	$0.272^{+0.001}_{-0.001}$	1082^{+41}_{-38}	$-3.08^{+0.21}_{-0.21}$	no
100	0.078	0.006	$0.273^{+0.001}_{-0.001}$	969^{+35}_{-39}	$-2.88^{+0.25}_{-0.21}$	no
101	0.078	0.03	$0.273^{+0.001}_{-0.001}$	1018^{+42}_{-34}	$-2.99^{+0.23}_{-0.23}$	no
102	0.094	0.001	$0.273^{+0.001}_{-0.001}$	906^{+34}_{-35}	$-2.69^{+0.24}_{-0.22}$	no
103	0.094	0.006	$0.273^{+0.001}_{-0.001}$	935^{+37}_{-34}	$-2.76^{+0.24}_{-0.21}$	no
104	0.094	0.033	$0.273^{+0.001}_{-0.001}$	999^{+36}_{-36}	$-2.9^{+0.23}_{-0.22}$	no
105	0.139	0.001	$0.275^{+0.001}_{-0.001}$	584^{+42}_{-43}	$-1.5^{+0.18}_{-0.22}$	no
106	0.139	0.008	$0.274^{+0.001}_{-0.001}$	619^{+50}_{-37}	$-1.59^{+0.2}_{-0.23}$	no
107	0.139	0.039	$0.273^{+0.001}_{-0.001}$	782^{+24}_{-31}	$-2.14^{+0.26}_{-0.27}$	no
108	0.0	0.0	$0.273^{+0.001}_{-0.001}$	1047^{+45}_{-44}	$-3.21^{+0.25}_{-0.22}$	no
109	0.0	0.0	$0.273^{+0.001}_{-0.001}$	1047^{+46}_{-42}	$-3.21^{+0.25}_{-0.21}$	no
110	0.0	0.006	$0.273^{+0.001}_{-0.001}$	1049^{+42}_{-42}	$-3.21^{+0.24}_{-0.22}$	no
111	0.017	0.0	$0.273^{+0.001}_{-0.001}$	1032^{+44}_{-39}	$-3.16^{+0.23}_{-0.22}$	no
112	0.017	0.003	$0.273^{+0.001}_{-0.001}$	1039^{+42}_{-40}	$-3.18^{+0.23}_{-0.22}$	no
113	0.017	0.014	$0.273^{+0.001}_{-0.001}$	1074^{+41}_{-42}	$-3.24^{+0.23}_{-0.22}$	no
114	0.069	0.0	$0.273^{+0.001}_{-0.001}$	1002^{+43}_{-39}	$-3.04^{+0.24}_{-0.23}$	no
115	0.069	0.005	$0.273^{+0.001}_{-0.001}$	1011^{+38}_{-37}	$-3.05^{+0.23}_{-0.23}$	no
116	0.069	0.025	$0.273^{+0.001}_{-0.001}$	1050^{+41}_{-48}	$-3.15^{+0.26}_{-0.21}$	no
117	0.02	0.0	$0.273^{+0.001}_{-0.001}$	1058^{+44}_{-41}	$-3.19^{+0.22}_{-0.2}$	no

118	0.02	0.003	$0.273^{+0.001}_{-0.001}$	1024^{+43}_{-41}	$-3.12^{+0.23}_{-0.23}$	no
119	0.02	0.016	$0.273^{+0.001}_{-0.001}$	1070^{+39}_{-40}	$-3.2^{+0.21}_{-0.21}$	no
120	0.031	0.0	$0.273^{+0.001}_{-0.001}$	1068^{+43}_{-40}	$-3.19^{+0.21}_{-0.2}$	no
121	0.031	0.004	$0.273^{+0.001}_{-0.001}$	1022^{+46}_{-41}	$-3.1^{+0.24}_{-0.22}$	no
122	0.031	0.019	$0.273^{+0.001}_{-0.001}$	1060^{+40}_{-43}	$-3.18^{+0.24}_{-0.22}$	no
123	0.07	0.0	$0.273^{+0.001}_{-0.001}$	1005^{+41}_{-39}	$-3.04^{+0.24}_{-0.23}$	no
124	0.07	0.005	$0.273^{+0.001}_{-0.001}$	1008^{+43}_{-38}	$-3.05^{+0.22}_{-0.22}$	no
125	0.07	0.025	$0.273^{+0.001}_{-0.001}$	1036^{+44}_{-39}	$-3.12^{+0.23}_{-0.21}$	no
126	0.078	0.001	$0.272^{+0.001}_{-0.001}$	1079^{+38}_{-39}	$-3.08^{+0.21}_{-0.2}$	no
127	0.078	0.005	$0.273^{+0.001}_{-0.001}$	968^{+37}_{-35}	$-2.88^{+0.23}_{-0.22}$	no
128	0.078	0.028	$0.273^{+0.001}_{-0.001}$	1019^{+41}_{-35}	$-2.98^{+0.23}_{-0.22}$	no
129	0.079	0.001	$0.272^{+0.001}_{-0.001}$	1081^{+41}_{-36}	$-3.08^{+0.21}_{-0.2}$	no
130	0.079	0.005	$0.273^{+0.001}_{-0.001}$	968^{+36}_{-37}	$-2.89^{+0.23}_{-0.23}$	no
131	0.079	0.028	$0.273^{+0.001}_{-0.001}$	1011^{+42}_{-38}	$-2.98^{+0.24}_{-0.23}$	no
132	0.099	0.001	$0.273^{+0.001}_{-0.001}$	963^{+35}_{-37}	$-2.87^{+0.22}_{-0.23}$	no
133	0.099	0.006	$0.273^{+0.001}_{-0.001}$	970^{+36}_{-36}	$-2.89^{+0.23}_{-0.2}$	no
134	0.099	0.03	$0.273^{+0.001}_{-0.001}$	1011^{+39}_{-35}	$-2.97^{+0.22}_{-0.23}$	no
135	0.0	0.0	$0.273^{+0.001}_{-0.001}$	1046^{+45}_{-43}	$-3.21^{+0.24}_{-0.21}$	no
136	0.0	0.0	$0.273^{+0.001}_{-0.001}$	1047^{+45}_{-42}	$-3.2^{+0.24}_{-0.2}$	no
137	0.0	0.004	$0.273^{+0.001}_{-0.001}$	1046^{+45}_{-39}	$-3.21^{+0.22}_{-0.21}$	no
138	0.008	0.0	$0.273^{+0.001}_{-0.001}$	1066^{+40}_{-43}	$-3.28^{+0.23}_{-0.19}$	no
139	0.008	0.001	$0.273^{+0.001}_{-0.001}$	1068^{+39}_{-44}	$-3.27^{+0.22}_{-0.2}$	no
140	0.008	0.009	$0.273^{+0.001}_{-0.001}$	1102^{+44}_{-44}	$-3.31^{+0.21}_{-0.2}$	no
141	0.031	0.0	$0.273^{+0.001}_{-0.001}$	1104^{+45}_{-45}	$-3.42^{+0.21}_{-0.2}$	no
142	0.031	0.002	$0.273^{+0.001}_{-0.001}$	1114^{+50}_{-46}	$-3.43^{+0.22}_{-0.22}$	no
143	0.031	0.014	$0.272^{+0.001}_{-0.001}$	1165^{+40}_{-47}	$-3.46^{+0.22}_{-0.19}$	no

144	0.02	0.0	$0.273^{+0.001}_{-0.001}$	1057^{+41}_{-41}	$-3.18^{+0.22}_{-0.21}$	no
145	0.02	0.003	$0.273^{+0.001}_{-0.001}$	1025^{+45}_{-39}	$-3.11^{+0.24}_{-0.23}$	no
146	0.02	0.016	$0.273^{+0.001}_{-0.001}$	1077^{+40}_{-42}	$-3.21^{+0.22}_{-0.22}$	no
147	0.027	0.0	$0.273^{+0.001}_{-0.001}$	1036^{+47}_{-43}	$-3.16^{+0.23}_{-0.22}$	no
148	0.027	0.004	$0.273^{+0.001}_{-0.001}$	1043^{+48}_{-41}	$-3.19^{+0.25}_{-0.21}$	no
149	0.027	0.021	$0.272^{+0.001}_{-0.001}$	1109^{+41}_{-39}	$-3.28^{+0.2}_{-0.21}$	no
150	0.05	0.001	$0.273^{+0.001}_{-0.001}$	1063^{+44}_{-44}	$-3.31^{+0.23}_{-0.21}$	no
151	0.05	0.005	$0.273^{+0.001}_{-0.001}$	1065^{+44}_{-46}	$-3.31^{+0.26}_{-0.22}$	no
152	0.05	0.026	$0.272^{+0.001}_{-0.001}$	1159^{+42}_{-45}	$-3.39^{+0.23}_{-0.2}$	no
153	0.078	0.001	$0.272^{+0.001}_{-0.001}$	1081^{+40}_{-37}	$-3.07^{+0.2}_{-0.21}$	no
154	0.078	0.005	$0.273^{+0.001}_{-0.001}$	968^{+36}_{-38}	$-2.88^{+0.23}_{-0.23}$	no
155	0.078	0.029	$0.273^{+0.001}_{-0.001}$	1024^{+40}_{-37}	$-3.0^{+0.24}_{-0.22}$	no
156	0.086	0.001	$0.273^{+0.001}_{-0.001}$	975^{+36}_{-39}	$-2.92^{+0.24}_{-0.22}$	no
157	0.086	0.006	$0.273^{+0.001}_{-0.001}$	980^{+36}_{-37}	$-2.93^{+0.23}_{-0.22}$	no
158	0.086	0.034	$0.273^{+0.001}_{-0.001}$	1043^{+40}_{-39}	$-3.06^{+0.24}_{-0.21}$	no
159	0.109	0.001	$0.273^{+0.001}_{-0.001}$	1006^{+42}_{-37}	$-3.05^{+0.22}_{-0.24}$	no
160	0.109	0.007	$0.273^{+0.001}_{-0.001}$	1019^{+42}_{-41}	$-3.08^{+0.24}_{-0.23}$	no
161	0.109	0.039	$0.273^{+0.001}_{-0.001}$	1078^{+39}_{-42}	$-3.2^{+0.24}_{-0.22}$	no
162	0.0	0.0	$0.273^{+0.001}_{-0.001}$	1046^{+45}_{-42}	$-3.22^{+0.22}_{-0.22}$	no
163	0.0	0.0	$0.273^{+0.001}_{-0.001}$	1047^{+46}_{-42}	$-3.2^{+0.24}_{-0.22}$	no
164	0.0	0.005	$0.273^{+0.001}_{-0.001}$	1047^{+44}_{-40}	$-3.21^{+0.23}_{-0.21}$	no
165	0.022	0.0	$0.273^{+0.001}_{-0.001}$	1052^{+43}_{-38}	$-3.14^{+0.22}_{-0.21}$	no
166	0.022	0.003	$0.273^{+0.001}_{-0.001}$	1061^{+41}_{-37}	$-3.15^{+0.21}_{-0.21}$	no
167	0.022	0.019	$0.272^{+0.001}_{-0.001}$	1077^{+39}_{-42}	$-3.18^{+0.23}_{-0.21}$	no
168	0.089	0.001	$0.273^{+0.001}_{-0.001}$	823^{+34}_{-28}	$-2.42^{+0.22}_{-0.24}$	no
169	0.089	0.006	$0.273^{+0.001}_{-0.001}$	852^{+35}_{-33}	$-2.5^{+0.22}_{-0.22}$	no

170	0.089	0.034	$0.272^{+0.001}_{-0.001}$	983^{+30}_{-34}	$-2.8^{+0.2}_{-0.2}$	no
171	0.011	0.0	$0.273^{+0.001}_{-0.001}$	1049^{+43}_{-44}	$-3.25^{+0.24}_{-0.21}$	no
172	0.011	0.002	$0.273^{+0.001}_{-0.001}$	1052^{+46}_{-40}	$-3.23^{+0.23}_{-0.2}$	no
173	0.011	0.012	$0.273^{+0.001}_{-0.001}$	1110^{+45}_{-40}	$-3.31^{+0.23}_{-0.21}$	no
174	0.033	0.0	$0.273^{+0.001}_{-0.001}$	1070^{+41}_{-39}	$-3.18^{+0.21}_{-0.21}$	no
175	0.033	0.005	$0.273^{+0.001}_{-0.001}$	1020^{+43}_{-39}	$-3.1^{+0.23}_{-0.24}$	no
176	0.033	0.026	$0.272^{+0.001}_{-0.001}$	1107^{+45}_{-38}	$-3.24^{+0.22}_{-0.21}$	no
177	0.1	0.001	$0.273^{+0.001}_{-0.001}$	823^{+34}_{-30}	$-2.43^{+0.25}_{-0.24}$	no
178	0.1	0.008	$0.273^{+0.001}_{-0.001}$	859^{+34}_{-34}	$-2.53^{+0.24}_{-0.24}$	no
179	0.1	0.041	$0.272^{+0.001}_{-0.001}$	992^{+33}_{-33}	$-2.83^{+0.22}_{-0.22}$	no
180	0.045	0.0	$0.273^{+0.001}_{-0.001}$	1058^{+43}_{-47}	$-3.34^{+0.26}_{-0.21}$	no
181	0.045	0.003	$0.273^{+0.001}_{-0.001}$	1059^{+44}_{-47}	$-3.34^{+0.24}_{-0.21}$	no
182	0.045	0.02	$0.272^{+0.001}_{-0.001}$	1136^{+49}_{-44}	$-3.39^{+0.25}_{-0.2}$	no
183	0.067	0.001	$0.273^{+0.001}_{-0.001}$	1043^{+45}_{-41}	$-3.2^{+0.23}_{-0.21}$	no
184	0.067	0.006	$0.273^{+0.001}_{-0.001}$	1051^{+43}_{-40}	$-3.22^{+0.24}_{-0.21}$	no
185	0.067	0.033	$0.272^{+0.001}_{-0.001}$	1143^{+48}_{-45}	$-3.35^{+0.23}_{-0.22}$	no
186	0.134	0.001	$0.274^{+0.001}_{-0.001}$	787^{+27}_{-31}	$-2.31^{+0.26}_{-0.28}$	no
187	0.134	0.009	$0.273^{+0.001}_{-0.001}$	834^{+37}_{-29}	$-2.47^{+0.26}_{-0.28}$	no
188	0.134	0.048	$0.272^{+0.001}_{-0.001}$	1037^{+41}_{-36}	$-2.95^{+0.24}_{-0.23}$	no
189	0.0	0.0	$0.273^{+0.001}_{-0.001}$	1047^{+47}_{-43}	$-3.21^{+0.23}_{-0.22}$	no
190	0.0	0.0	$0.273^{+0.001}_{-0.001}$	1048^{+44}_{-42}	$-3.22^{+0.23}_{-0.2}$	no
191	0.0	0.004	$0.273^{+0.001}_{-0.001}$	1045^{+45}_{-40}	$-3.21^{+0.23}_{-0.2}$	no
192	0.017	0.0	$0.273^{+0.001}_{-0.001}$	1032^{+44}_{-40}	$-3.16^{+0.24}_{-0.21}$	no
193	0.017	0.003	$0.273^{+0.001}_{-0.001}$	1040^{+43}_{-41}	$-3.18^{+0.21}_{-0.23}$	no
194	0.017	0.015	$0.273^{+0.001}_{-0.001}$	1086^{+39}_{-42}	$-3.23^{+0.23}_{-0.2}$	no
195	0.069	0.0	$0.273^{+0.001}_{-0.001}$	1003^{+40}_{-39}	$-3.04^{+0.22}_{-0.22}$	no

196	0.069	0.005	$0.273^{+0.001}_{-0.001}$	1012^{+44}_{-39}	$-3.06^{+0.22}_{-0.23}$	no
197	0.069	0.026	$0.273^{+0.001}_{-0.001}$	1050^{+44}_{-41}	$-3.16^{+0.25}_{-0.22}$	no
198	0.011	0.0	$0.273^{+0.001}_{-0.001}$	1045^{+46}_{-44}	$-3.23^{+0.25}_{-0.22}$	no
199	0.011	0.002	$0.273^{+0.001}_{-0.001}$	1054^{+42}_{-43}	$-3.25^{+0.23}_{-0.22}$	no
200	0.011	0.011	$0.273^{+0.001}_{-0.001}$	1099^{+45}_{-38}	$-3.29^{+0.22}_{-0.21}$	no
201	0.028	0.0	$0.273^{+0.001}_{-0.001}$	1045^{+44}_{-42}	$-3.21^{+0.24}_{-0.23}$	no
202	0.028	0.004	$0.273^{+0.001}_{-0.001}$	1048^{+45}_{-43}	$-3.23^{+0.22}_{-0.22}$	no
203	0.028	0.021	$0.272^{+0.001}_{-0.001}$	1099^{+44}_{-40}	$-3.26^{+0.22}_{-0.22}$	no
204	0.077	0.001	$0.273^{+0.001}_{-0.001}$	1013^{+41}_{-42}	$-3.07^{+0.23}_{-0.23}$	no
205	0.077	0.005	$0.273^{+0.001}_{-0.001}$	1020^{+46}_{-40}	$-3.1^{+0.24}_{-0.23}$	no
206	0.077	0.026	$0.273^{+0.001}_{-0.001}$	1055^{+41}_{-42}	$-3.18^{+0.25}_{-0.22}$	no
207	0.045	0.0	$0.273^{+0.001}_{-0.001}$	1059^{+44}_{-48}	$-3.34^{+0.25}_{-0.22}$	no
208	0.045	0.003	$0.273^{+0.001}_{-0.001}$	1059^{+45}_{-43}	$-3.34^{+0.23}_{-0.21}$	no
209	0.045	0.017	$0.273^{+0.001}_{-0.001}$	1105^{+47}_{-42}	$-3.35^{+0.21}_{-0.21}$	no
210	0.058	0.0	$0.273^{+0.001}_{-0.001}$	1057^{+45}_{-42}	$-3.3^{+0.24}_{-0.2}$	no
211	0.058	0.004	$0.273^{+0.001}_{-0.001}$	1066^{+43}_{-44}	$-3.33^{+0.23}_{-0.21}$	no
212	0.058	0.021	$0.273^{+0.001}_{-0.001}$	1101^{+46}_{-44}	$-3.36^{+0.23}_{-0.21}$	no
213	0.095	0.0	$0.273^{+0.001}_{-0.001}$	1040^{+44}_{-41}	$-3.19^{+0.24}_{-0.21}$	no
214	0.095	0.005	$0.273^{+0.001}_{-0.001}$	1042^{+46}_{-42}	$-3.19^{+0.26}_{-0.22}$	no
215	0.095	0.027	$0.273^{+0.001}_{-0.001}$	1066^{+47}_{-42}	$-3.27^{+0.25}_{-0.24}$	no
216	0.0	0.0	$0.273^{+0.001}_{-0.001}$	1047^{+44}_{-41}	$-3.22^{+0.22}_{-0.22}$	no
217	0.0	0.0	$0.273^{+0.001}_{-0.001}$	1047^{+44}_{-41}	$-3.21^{+0.22}_{-0.22}$	no
218	0.0	0.003	$0.273^{+0.001}_{-0.001}$	1044^{+44}_{-43}	$-3.2^{+0.25}_{-0.22}$	no
219	0.008	0.0	$0.273^{+0.001}_{-0.001}$	1066^{+39}_{-42}	$-3.28^{+0.23}_{-0.2}$	no
220	0.008	0.001	$0.273^{+0.001}_{-0.001}$	1067^{+43}_{-44}	$-3.27^{+0.24}_{-0.21}$	no
221	0.008	0.006	$0.273^{+0.001}_{-0.001}$	1079^{+39}_{-43}	$-3.28^{+0.21}_{-0.2}$	no

222	0.031	0.0	$0.273^{+0.001}_{-0.001}$	1105^{+49}_{-43}	$-3.42^{+0.21}_{-0.21}$	no
223	0.031	0.002	$0.273^{+0.001}_{-0.001}$	1112^{+47}_{-44}	$-3.42^{+0.21}_{-0.2}$	no
224	0.031	0.011	$0.273^{+0.001}_{-0.001}$	1143^{+46}_{-46}	$-3.43^{+0.23}_{-0.2}$	no
225	0.011	0.0	$0.273^{+0.001}_{-0.001}$	1046^{+48}_{-41}	$-3.23^{+0.24}_{-0.22}$	no
226	0.011	0.002	$0.273^{+0.001}_{-0.001}$	1053^{+43}_{-43}	$-3.25^{+0.22}_{-0.21}$	no
227	0.011	0.009	$0.273^{+0.001}_{-0.001}$	1081^{+43}_{-39}	$-3.27^{+0.2}_{-0.21}$	no
228	0.016	0.0	$0.273^{+0.001}_{-0.001}$	1061^{+42}_{-41}	$-3.29^{+0.22}_{-0.2}$	no
229	0.016	0.002	$0.273^{+0.001}_{-0.001}$	1068^{+41}_{-43}	$-3.29^{+0.22}_{-0.21}$	no
230	0.016	0.01	$0.273^{+0.001}_{-0.001}$	1092^{+42}_{-44}	$-3.31^{+0.21}_{-0.21}$	no
231	0.031	0.0	$0.273^{+0.001}_{-0.001}$	1102^{+47}_{-42}	$-3.4^{+0.21}_{-0.21}$	no
232	0.031	0.002	$0.273^{+0.001}_{-0.001}$	1111^{+47}_{-43}	$-3.42^{+0.21}_{-0.2}$	no
233	0.031	0.011	$0.273^{+0.001}_{-0.001}$	1132^{+49}_{-43}	$-3.44^{+0.21}_{-0.2}$	no
234	0.045	0.0	$0.273^{+0.001}_{-0.001}$	1058^{+45}_{-46}	$-3.34^{+0.24}_{-0.22}$	no
235	0.045	0.003	$0.273^{+0.001}_{-0.001}$	1058^{+43}_{-47}	$-3.35^{+0.24}_{-0.22}$	no
236	0.045	0.016	$0.273^{+0.001}_{-0.001}$	1105^{+47}_{-41}	$-3.34^{+0.22}_{-0.22}$	no
237	0.045	0.0	$0.273^{+0.001}_{-0.001}$	1061^{+43}_{-44}	$-3.34^{+0.25}_{-0.21}$	no
238	0.045	0.003	$0.273^{+0.001}_{-0.001}$	1057^{+46}_{-44}	$-3.34^{+0.25}_{-0.21}$	no
239	0.045	0.016	$0.273^{+0.001}_{-0.001}$	1106^{+50}_{-43}	$-3.36^{+0.23}_{-0.22}$	no
240	0.051	0.0	$0.273^{+0.001}_{-0.001}$	1068^{+44}_{-47}	$-3.39^{+0.24}_{-0.22}$	no
241	0.051	0.003	$0.273^{+0.001}_{-0.001}$	1075^{+43}_{-45}	$-3.39^{+0.23}_{-0.21}$	no
242	0.051	0.016	$0.273^{+0.001}_{-0.001}$	1129^{+51}_{-43}	$-3.42^{+0.23}_{-0.22}$	no

Table C.2: List of atmospheric and planetary parameters retrieved for each case analyzed for M dwarf star.

Case	ff_{spot}	ff_{fac}	**Rplanet (Rj)**	**T (K)**	**log mixH2O**	**Spot crossing**
0	0.0	0.0	$0.281^{+0.001}_{-0.001}$	122^{+2}_{-2}	$-0.01^{+0.0}_{-0.0}$	no

1	0.0	0.001	$0.28^{+0.001}_{-0.001}$	101^{+1}_{-1}	$-6.85^{+0.66}_{-3.31}$	no
2	0.0	0.007	$0.28^{+0.001}_{-0.001}$	326^{+6}_{-4}	$-0.04^{+0.01}_{-0.01}$	no
3	0.022	0.0	$0.281^{+0.001}_{-0.001}$	112^{+11}_{-5}	$-0.03^{+0.02}_{-0.03}$	no
4	0.022	0.003	$0.281^{+0.001}_{-0.001}$	103^{+1}_{-2}	$-0.01^{+0.01}_{-0.01}$	no
5	0.022	0.018	$0.279^{+0.001}_{-0.001}$	1108^{+100}_{-92}	$-0.01^{+0.0}_{-0.01}$	no
6	0.089	0.001	$0.28^{+0.001}_{-0.001}$	101^{+1}_{-1}	$-8.8^{+1.83}_{-2.4}$	no
7	0.089	0.006	$0.281^{+0.001}_{-0.001}$	106^{+6}_{-3}	$-0.02^{+0.01}_{-0.02}$	no
8	0.089	0.032	$0.281^{+0.001}_{-0.001}$	110^{+10}_{-5}	$-0.02^{+0.01}_{-0.02}$	no
9	0.023	0.0	$0.281^{+0.001}_{-0.001}$	106^{+7}_{-3}	$-0.02^{+0.01}_{-0.02}$	no
10	0.023	0.003	$0.281^{+0.001}_{-0.001}$	105^{+7}_{-3}	$-0.02^{+0.01}_{-0.02}$	no
11	0.023	0.018	$0.281^{+0.001}_{-0.001}$	108^{+8}_{-4}	$-0.02^{+0.01}_{-0.02}$	no
12	0.038	0.0	$0.28^{+0.001}_{-0.001}$	101^{+1}_{-1}	$-7.34^{+0.79}_{-2.92}$	no
13	0.038	0.004	$0.281^{+0.001}_{-0.001}$	106^{+7}_{-3}	$-0.02^{+0.01}_{-0.02}$	no
14	0.038	0.023	$0.279^{+0.001}_{-0.001}$	1084^{+89}_{-85}	$-0.01^{+0.0}_{-0.01}$	no
15	0.09	0.001	$0.281^{+0.001}_{-0.001}$	113^{+5}_{-3}	$-0.02^{+0.01}_{-0.02}$	no
16	0.09	0.006	$0.281^{+0.001}_{-0.001}$	104^{+2}_{-2}	$-0.01^{+0.01}_{-0.01}$	no
17	0.09	0.032	$0.281^{+0.001}_{-0.001}$	108^{+8}_{-4}	$-0.02^{+0.01}_{-0.02}$	no
18	0.09	0.001	$0.281^{+0.001}_{-0.001}$	120^{+2}_{-3}	$-0.02^{+0.01}_{-0.01}$	no
19	0.09	0.006	$0.28^{+0.001}_{-0.001}$	101^{+1}_{-1}	$-7.78^{+1.08}_{-3.22}$	no
20	0.09	0.032	$0.281^{+0.001}_{-0.001}$	110^{+9}_{-5}	$-0.04^{+0.01}_{-0.02}$	no
21	0.091	0.001	$0.28^{+0.001}_{-0.001}$	101^{+1}_{-1}	$-8.78^{+1.9}_{-2.23}$	no
22	0.091	0.006	$0.281^{+0.001}_{-0.001}$	101^{+1}_{-1}	$-0.01^{+0.0}_{-0.0}$	no
23	0.091	0.033	$0.281^{+0.001}_{-0.001}$	122^{+5}_{-5}	$-0.02^{+0.01}_{-0.01}$	no
24	0.121	0.001	$0.281^{+0.001}_{-0.001}$	101^{+1}_{-1}	$-8.68^{+1.94}_{-2.29}$	no
25	0.121	0.007	$0.28^{+0.001}_{-0.001}$	101^{+1}_{-1}	$-8.28^{+1.54}_{-2.89}$	no
26	0.121	0.037	$0.281^{+0.001}_{-0.001}$	107^{+8}_{-4}	$-0.02^{+0.01}_{-0.02}$	no

27	0.0	0.0	$0.281^{+0.001}_{-0.001}$	146^{+8}_{-2}	$-0.33^{+0.03}_{-0.02}$	no
28	0.0	0.001	$0.281^{+0.001}_{-0.001}$	106^{+7}_{-3}	$-0.02^{+0.01}_{-0.02}$	no
29	0.0	0.006	$0.281^{+0.001}_{-0.001}$	108^{+8}_{-4}	$-0.02^{+0.01}_{-0.02}$	no
30	0.017	0.0	$0.28^{+0.001}_{-0.001}$	100^{+1}_{-1}	$-6.09^{+0.38}_{-0.34}$	no
31	0.017	0.003	$0.281^{+0.001}_{-0.001}$	106^{+7}_{-3}	$-0.02^{+0.01}_{-0.02}$	no
32	0.017	0.017	$0.279^{+0.001}_{-0.001}$	1349^{+33}_{-67}	$-0.0^{+0.0}_{-0.0}$	no
33	0.069	0.001	$0.28^{+0.001}_{-0.001}$	101^{+1}_{-1}	$-7.46^{+0.98}_{-3.49}$	no
34	0.069	0.005	$0.281^{+0.001}_{-0.001}$	106^{+1}_{-3}	$-0.04^{+0.0}_{-0.0}$	no
35	0.069	0.028	$0.279^{+0.001}_{-0.001}$	1196^{+10}_{-11}	$-0.0^{+0.0}_{-0.0}$	no
36	0.023	0.0	$0.28^{+0.001}_{-0.001}$	101^{+1}_{-1}	$-7.1^{+0.75}_{-2.91}$	no
37	0.023	0.003	$0.279^{+0.001}_{-0.001}$	971^{+17}_{-32}	$-0.01^{+0.0}_{-0.01}$	no
38	0.023	0.02	$0.279^{+0.001}_{-0.001}$	1388^{+8}_{-15}	$-0.0^{+0.0}_{-0.0}$	no
39	0.04	0.001	$0.281^{+0.001}_{-0.001}$	184^{+1}_{-1}	$-0.0^{+0.0}_{-0.0}$	no
40	0.04	0.006	$0.281^{+0.001}_{-0.001}$	106^{+7}_{-3}	$-0.02^{+0.01}_{-0.02}$	no
41	0.04	0.031	$0.281^{+0.001}_{-0.001}$	109^{+8}_{-4}	$-0.02^{+0.01}_{-0.02}$	no
42	0.091	0.001	$0.281^{+0.001}_{-0.001}$	105^{+6}_{-2}	$-0.02^{+0.01}_{-0.02}$	no
43	0.091	0.008	$0.281^{+0.001}_{-0.001}$	106^{+7}_{-3}	$-0.01^{+0.01}_{-0.02}$	no
44	0.091	0.042	$0.279^{+0.001}_{-0.001}$	1487^{+7}_{-15}	$-0.01^{+0.01}_{-0.01}$	no
45	0.09	0.001	$0.281^{+0.001}_{-0.001}$	104^{+5}_{-2}	$-0.01^{+0.01}_{-0.02}$	no
46	0.09	0.006	$0.28^{+0.001}_{-0.001}$	100^{+1}_{-1}	$-11.02^{+0.74}_{-0.4}$	no
47	0.09	0.035	$0.281^{+0.001}_{-0.001}$	110^{+11}_{-5}	$-0.02^{+0.01}_{-0.02}$	no
48	0.107	0.001	$0.281^{+0.001}_{-0.001}$	103^{+4}_{-1}	$-0.01^{+0.01}_{-0.02}$	no
49	0.107	0.009	$0.28^{+0.001}_{-0.001}$	100^{+1}_{-1}	$-6.17^{+0.53}_{-0.53}$	no
50	0.107	0.046	$0.279^{+0.001}_{-0.001}$	1390^{+7}_{-14}	$-0.01^{+0.0}_{-0.01}$	no
51	0.159	0.001	$0.281^{+0.001}_{-0.001}$	108^{+6}_{-4}	$-0.02^{+0.01}_{-0.02}$	no
52	0.159	0.011	$0.28^{+0.001}_{-0.001}$	101^{+1}_{-1}	$-7.16^{+0.62}_{-2.46}$	no

53	0.159	0.057	$0.279^{+0.001}_{-0.001}$	1489^{+6}_{-12}	$-0.06^{+0.03}_{-0.03}$	no
54	0.0	0.0	$0.281^{+0.001}_{-0.001}$	106^{+8}_{-3}	$-0.02^{+0.01}_{-0.02}$	no
55	0.0	0.0	$0.281^{+0.001}_{-0.001}$	105^{+3}_{-3}	$-0.05^{+0.01}_{-0.01}$	no
56	0.0	0.005	$0.281^{+0.001}_{-0.001}$	109^{+8}_{-4}	$-0.02^{+0.01}_{-0.02}$	no
57	0.008	0.0	$0.281^{+0.001}_{-0.001}$	107^{+7}_{-4}	$-0.02^{+0.01}_{-0.02}$	no
58	0.008	0.001	$0.281^{+0.001}_{-0.001}$	106^{+7}_{-3}	$-0.02^{+0.01}_{-0.02}$	no
59	0.008	0.01	$0.281^{+0.001}_{-0.001}$	107^{+7}_{-4}	$-0.02^{+0.01}_{-0.02}$	no
60	0.031	0.0	$0.281^{+0.001}_{-0.001}$	107^{+8}_{-4}	$-0.02^{+0.01}_{-0.02}$	no
61	0.031	0.002	$0.28^{+0.001}_{-0.001}$	112^{+1}_{-1}	$-0.23^{+0.02}_{-0.02}$	no
62	0.031	0.015	$0.281^{+0.001}_{-0.001}$	122^{+5}_{-9}	$-0.1^{+0.03}_{-0.03}$	no
63	0.023	0.0	$0.281^{+0.001}_{-0.001}$	115^{+11}_{-8}	$-0.03^{+0.02}_{-0.03}$	no
64	0.023	0.003	$0.281^{+0.001}_{-0.001}$	106^{+6}_{-3}	$-0.02^{+0.01}_{-0.02}$	no
65	0.023	0.019	$0.279^{+0.001}_{-0.001}$	1223^{+91}_{-16}	$-0.0^{+0.0}_{-0.0}$	no
66	0.03	0.0	$0.281^{+0.001}_{-0.001}$	106^{+7}_{-3}	$-0.02^{+0.01}_{-0.02}$	no
67	0.03	0.004	$0.281^{+0.001}_{-0.001}$	106^{+7}_{-3}	$-0.02^{+0.01}_{-0.02}$	no
68	0.03	0.024	$0.279^{+0.001}_{-0.001}$	1386^{+10}_{-19}	$-0.0^{+0.0}_{-0.0}$	no
69	0.053	0.001	$0.28^{+0.001}_{-0.001}$	101^{+1}_{-1}	$-5.98^{+0.52}_{-0.68}$	no
70	0.053	0.005	$0.281^{+0.001}_{-0.001}$	107^{+7}_{-4}	$-0.02^{+0.01}_{-0.02}$	no
71	0.053	0.029	$0.279^{+0.001}_{-0.001}$	1398^{+1}_{-3}	$-0.0^{+0.0}_{-0.0}$	no
72	0.09	0.001	$0.281^{+0.001}_{-0.001}$	103^{+4}_{-2}	$-0.01^{+0.01}_{-0.01}$	no
73	0.09	0.006	$0.281^{+0.001}_{-0.001}$	107^{+1}_{-2}	$-0.02^{+0.01}_{-0.02}$	no
74	0.09	0.034	$0.281^{+0.001}_{-0.001}$	109^{+10}_{-5}	$-0.02^{+0.01}_{-0.02}$	no
75	0.098	0.001	$0.281^{+0.001}_{-0.001}$	100^{+1}_{-1}	$-6.62^{+0.44}_{-0.43}$	no
76	0.098	0.007	$0.28^{+0.001}_{-0.001}$	101^{+1}_{-1}	$-7.68^{+0.89}_{-3.62}$	no
77	0.098	0.039	$0.279^{+0.001}_{-0.001}$	1196^{+5}_{-11}	$-0.0^{+0.0}_{-0.0}$	no
78	0.121	0.001	$0.281^{+0.001}_{-0.001}$	104^{+5}_{-2}	$-0.01^{+0.01}_{-0.02}$	no

79	0.121	0.008	$0.281^{+0.001}_{-0.001}$	105^{+6}_{-3}	$-0.02^{+0.01}_{-0.02}$	no
80	0.121	0.044	$0.279^{+0.001}_{-0.001}$	1259^{+31}_{-77}	$-0.04^{+0.01}_{-0.02}$	no
81	0.0	0.0	$0.281^{+0.001}_{-0.001}$	153^{+3}_{-2}	$-0.01^{+0.01}_{-0.01}$	no
82	0.0	0.001	$0.28^{+0.001}_{-0.001}$	101^{+1}_{-1}	$-6.4^{+0.61}_{-1.36}$	no
83	0.0	0.006	$0.28^{+0.001}_{-0.001}$	101^{+1}_{-1}	$-6.55^{+0.61}_{-1.73}$	no
84	0.022	0.0	$0.281^{+0.001}_{-0.001}$	106^{+6}_{-3}	$-0.02^{+0.01}_{-0.02}$	no
85	0.022	0.003	$0.281^{+0.001}_{-0.001}$	106^{+7}_{-3}	$-0.02^{+0.01}_{-0.02}$	no
86	0.022	0.02	$0.279^{+0.001}_{-0.001}$	1299^{+3}_{-5}	$-0.0^{+0.0}_{-0.0}$	no
87	0.089	0.001	$0.28^{+0.001}_{-0.001}$	104^{+4}_{-2}	$-0.01^{+0.01}_{-0.01}$	no
88	0.089	0.006	$0.281^{+0.001}_{-0.001}$	105^{+6}_{-3}	$-0.02^{+0.01}_{-0.02}$	no
89	0.089	0.033	$0.279^{+0.001}_{-0.001}$	1172^{+85}_{-88}	$-0.01^{+0.0}_{-0.01}$	no
90	0.02	0.0	$0.28^{+0.001}_{-0.001}$	101^{+1}_{-1}	$-11.79^{+0.1}_{-0.15}$	no
91	0.02	0.003	$0.281^{+0.001}_{-0.001}$	106^{+7}_{-4}	$-0.02^{+0.01}_{-0.02}$	no
92	0.02	0.019	$0.281^{+0.001}_{-0.001}$	209^{+4}_{-5}	$-0.01^{+0.0}_{-0.01}$	no
93	0.042	0.001	$0.28^{+0.001}_{-0.001}$	101^{+1}_{-1}	$-7.8^{+1.46}_{-3.1}$	no
94	0.042	0.006	$0.281^{+0.001}_{-0.001}$	109^{+7}_{-5}	$-0.02^{+0.01}_{-0.02}$	no
95	0.042	0.03	$0.28^{+0.001}_{-0.001}$	673^{+28}_{-27}	$-0.02^{+0.01}_{-0.01}$	no
96	0.102	0.001	$0.28^{+0.001}_{-0.001}$	502^{+33}_{-24}	$-0.18^{+0.02}_{-0.03}$	no
97	0.102	0.007	$0.281^{+0.001}_{-0.001}$	105^{+6}_{-2}	$-0.02^{+0.01}_{-0.02}$	no
98	0.102	0.036	$0.281^{+0.001}_{-0.001}$	109^{+11}_{-5}	$-0.02^{+0.01}_{-0.02}$	no
99	0.078	0.001	$0.281^{+0.001}_{-0.001}$	105^{+5}_{-2}	$-0.01^{+0.01}_{-0.02}$	no
100	0.078	0.006	$0.281^{+0.001}_{-0.001}$	136^{+9}_{-6}	$-0.03^{+0.02}_{-0.03}$	no
101	0.078	0.03	$0.281^{+0.001}_{-0.001}$	110^{+10}_{-5}	$-0.02^{+0.01}_{-0.02}$	no
102	0.094	0.001	$0.28^{+0.001}_{-0.001}$	100^{+1}_{-1}	$-6.53^{+0.47}_{-0.81}$	no
103	0.094	0.006	$0.28^{+0.001}_{-0.001}$	101^{+1}_{-1}	$-6.42^{+0.56}_{-0.84}$	no
104	0.094	0.033	$0.281^{+0.001}_{-0.001}$	111^{+12}_{-6}	$-0.02^{+0.01}_{-0.02}$	no

105	0.139	0.001	$0.281^{+0.001}_{-0.001}$	103^{+4}_{-1}	$-0.01^{+0.01}_{-0.01}$	no
106	0.139	0.008	$0.281^{+0.001}_{-0.001}$	105^{+5}_{-3}	$-0.02^{+0.01}_{-0.02}$	no
107	0.139	0.039	$0.279^{+0.001}_{-0.001}$	1189^{+7}_{-10}	$-0.0^{+0.0}_{-0.0}$	no
108	0.0	0.0	$0.281^{+0.001}_{-0.001}$	105^{+6}_{-3}	$-0.02^{+0.01}_{-0.02}$	no
109	0.0	0.0	$0.281^{+0.001}_{-0.001}$	106^{+7}_{-3}	$-0.02^{+0.01}_{-0.02}$	no
110	0.0	0.006	$0.281^{+0.001}_{-0.001}$	121^{+4}_{-5}	$-0.03^{+0.0}_{-0.0}$	no
111	0.017	0.0	$0.281^{+0.001}_{-0.001}$	106^{+7}_{-3}	$-0.02^{+0.01}_{-0.02}$	no
112	0.017	0.003	$0.28^{+0.001}_{-0.001}$	776^{+24}_{-24}	$-0.01^{+0.0}_{-0.01}$	no
113	0.017	0.014	$0.281^{+0.001}_{-0.001}$	108^{+9}_{-5}	$-0.02^{+0.01}_{-0.02}$	no
114	0.069	0.0	$0.281^{+0.001}_{-0.001}$	105^{+6}_{-3}	$-0.02^{+0.01}_{-0.02}$	no
115	0.069	0.005	$0.281^{+0.001}_{-0.001}$	106^{+7}_{-3}	$-0.02^{+0.01}_{-0.02}$	no
116	0.069	0.025	$0.281^{+0.001}_{-0.001}$	111^{+11}_{-6}	$-0.03^{+0.01}_{-0.02}$	no
117	0.02	0.0	$0.281^{+0.001}_{-0.001}$	105^{+6}_{-3}	$-0.02^{+0.01}_{-0.02}$	no
118	0.02	0.003	$0.281^{+0.001}_{-0.001}$	106^{+7}_{-3}	$-0.02^{+0.01}_{-0.02}$	no
119	0.02	0.016	$0.279^{+0.001}_{-0.001}$	1075^{+72}_{-87}	$-0.01^{+0.0}_{-0.01}$	no
120	0.031	0.0	$0.281^{+0.001}_{-0.001}$	105^{+6}_{-3}	$-0.02^{+0.01}_{-0.02}$	no
121	0.031	0.004	$0.28^{+0.001}_{-0.001}$	101^{+1}_{-1}	$-7.06^{+0.85}_{-3.58}$	no
122	0.031	0.019	$0.281^{+0.001}_{-0.001}$	108^{+8}_{-4}	$-0.02^{+0.01}_{-0.02}$	no
123	0.07	0.0	$0.281^{+0.001}_{-0.001}$	105^{+4}_{-3}	$-0.02^{+0.01}_{-0.02}$	no
124	0.07	0.005	$0.281^{+0.001}_{-0.001}$	105^{+6}_{-3}	$-0.01^{+0.01}_{-0.02}$	no
125	0.07	0.025	$0.281^{+0.001}_{-0.001}$	108^{+8}_{-4}	$-0.02^{+0.01}_{-0.02}$	no
126	0.078	0.001	$0.281^{+0.001}_{-0.001}$	105^{+5}_{-3}	$-0.02^{+0.01}_{-0.02}$	no
127	0.078	0.005	$0.281^{+0.001}_{-0.001}$	105^{+7}_{-3}	$-0.02^{+0.01}_{-0.02}$	no
128	0.078	0.028	$0.281^{+0.001}_{-0.001}$	110^{+11}_{-6}	$-0.02^{+0.01}_{-0.02}$	no
129	0.079	0.001	$0.28^{+0.001}_{-0.001}$	100^{+1}_{-1}	$-11.02^{+1.06}_{-0.59}$	no
130	0.079	0.005	$0.281^{+0.001}_{-0.001}$	245^{+2}_{-2}	$-0.01^{+0.01}_{-0.01}$	no

131	0.079	0.028	$0.279^{+0.001}_{-0.001}$	1384^{+11}_{-20}	$-0.0^{+0.0}_{-0.0}$	no
132	0.099	0.001	$0.281^{+0.001}_{-0.001}$	120^{+3}_{-3}	$-0.02^{+0.01}_{-0.01}$	no
133	0.099	0.006	$0.281^{+0.001}_{-0.001}$	106^{+7}_{-3}	$-0.02^{+0.01}_{-0.02}$	no
134	0.099	0.03	$0.279^{+0.001}_{-0.001}$	1295^{+4}_{-8}	$-0.0^{+0.0}_{-0.0}$	no
135	0.0	0.0	$0.281^{+0.001}_{-0.001}$	106^{+7}_{-3}	$-0.02^{+0.01}_{-0.02}$	no
136	0.0	0.0	$0.28^{+0.001}_{-0.001}$	101^{+1}_{-1}	$-6.2^{+0.5}_{-1.0}$	no
137	0.0	0.004	$0.28^{+0.001}_{-0.001}$	412^{+14}_{-105}	$-0.05^{+0.02}_{-0.06}$	no
138	0.008	0.0	$0.28^{+0.001}_{-0.001}$	553^{+7}_{-8}	$-0.0^{+0.0}_{-0.0}$	no
139	0.008	0.001	$0.281^{+0.001}_{-0.001}$	116^{+11}_{-6}	$-0.03^{+0.02}_{-0.03}$	no
140	0.008	0.009	$0.281^{+0.001}_{-0.001}$	106^{+7}_{-3}	$-0.02^{+0.01}_{-0.02}$	no
141	0.031	0.0	$0.281^{+0.001}_{-0.001}$	107^{+3}_{-3}	$-0.08^{+0.01}_{-0.01}$	no
142	0.031	0.002	$0.281^{+0.001}_{-0.001}$	107^{+8}_{-4}	$-0.02^{+0.01}_{-0.02}$	no
143	0.031	0.014	$0.281^{+0.001}_{-0.001}$	325^{+6}_{-9}	$-0.02^{+0.01}_{-0.02}$	no
144	0.02	0.0	$0.28^{+0.001}_{-0.001}$	101^{+1}_{-1}	$-6.74^{+0.64}_{-1.93}$	no
145	0.02	0.003	$0.28^{+0.001}_{-0.001}$	746^{+49}_{-55}	$-0.01^{+0.01}_{-0.01}$	no
146	0.02	0.016	$0.279^{+0.001}_{-0.001}$	1140^{+109}_{-91}	$-0.01^{+0.0}_{-0.01}$	no
147	0.027	0.0	$0.281^{+0.001}_{-0.001}$	108^{+5}_{-4}	$-0.02^{+0.01}_{-0.02}$	no
148	0.027	0.004	$0.281^{+0.001}_{-0.001}$	147^{+3}_{-5}	$-0.01^{+0.01}_{-0.02}$	no
149	0.027	0.021	$0.281^{+0.001}_{-0.001}$	101^{+1}_{-1}	$-5.24^{+0.66}_{-0.76}$	no
150	0.05	0.001	$0.28^{+0.001}_{-0.001}$	374^{+23}_{-5}	$-0.01^{+0.01}_{-0.01}$	no
151	0.05	0.005	$0.28^{+0.001}_{-0.001}$	760^{+46}_{-80}	$-0.01^{+0.0}_{-0.01}$	no
152	0.05	0.026	$0.279^{+0.001}_{-0.001}$	1485^{+10}_{-14}	$-0.0^{+0.0}_{-0.0}$	no
153	0.078	0.001	$0.281^{+0.001}_{-0.001}$	124^{+1}_{-1}	$-0.06^{+0.0}_{-0.0}$	no
154	0.078	0.005	$0.28^{+0.001}_{-0.001}$	101^{+1}_{-1}	$-7.08^{+0.72}_{-2.99}$	no
155	0.078	0.029	$0.279^{+0.001}_{-0.001}$	1144^{+48}_{-59}	$-0.0^{+0.0}_{-0.0}$	no
156	0.086	0.001	$0.281^{+0.001}_{-0.001}$	105^{+5}_{-3}	$-0.02^{+0.01}_{-0.02}$	no

157	0.086	0.006	$0.281^{+0.001}_{-0.001}$	105^{+6}_{-3}	$-0.02^{+0.01}_{-0.02}$	no
158	0.086	0.034	$0.279^{+0.001}_{-0.001}$	1298^{+3}_{-8}	$-0.0^{+0.0}_{-0.0}$	no
159	0.109	0.001	$0.281^{+0.001}_{-0.001}$	105^{+2}_{-1}	$-0.01^{+0.01}_{-0.01}$	no
160	0.109	0.007	$0.281^{+0.001}_{-0.001}$	106^{+6}_{-3}	$-0.02^{+0.01}_{-0.02}$	no
161	0.109	0.039	$0.279^{+0.001}_{-0.001}$	1378^{+19}_{-53}	$-0.02^{+0.01}_{-0.02}$	no
162	0.0	0.0	$0.28^{+0.001}_{-0.001}$	101^{+1}_{-1}	$-6.36^{+0.6}_{-1.0}$	no
163	0.0	0.0	$0.28^{+0.001}_{-0.001}$	110^{+10}_{-6}	$-0.56^{+0.02}_{-0.01}$	no
164	0.0	0.005	$0.281^{+0.001}_{-0.001}$	106^{+6}_{-3}	$-0.01^{+0.01}_{-0.02}$	no
165	0.022	0.0	$0.281^{+0.001}_{-0.001}$	109^{+1}_{-1}	$-0.04^{+0.0}_{-0.0}$	no
166	0.022	0.003	$0.281^{+0.001}_{-0.001}$	140^{+1}_{-1}	$-0.1^{+0.01}_{-0.0}$	no
167	0.022	0.019	$0.281^{+0.001}_{-0.001}$	110^{+11}_{-6}	$-0.14^{+0.0}_{-0.0}$	no
168	0.089	0.001	$0.28^{+0.001}_{-0.001}$	101^{+1}_{-1}	$-8.7^{+1.85}_{-2.48}$	no
169	0.089	0.006	$0.281^{+0.001}_{-0.001}$	104^{+5}_{-2}	$-0.01^{+0.01}_{-0.02}$	no
170	0.089	0.034	$0.281^{+0.001}_{-0.001}$	109^{+11}_{-5}	$-0.02^{+0.01}_{-0.02}$	no
171	0.011	0.0	$0.281^{+0.001}_{-0.001}$	102^{+3}_{-1}	$-0.01^{+0.0}_{-0.01}$	no
172	0.011	0.002	$0.281^{+0.001}_{-0.001}$	106^{+8}_{-3}	$-0.02^{+0.01}_{-0.02}$	no
173	0.011	0.012	$0.279^{+0.001}_{-0.001}$	1328^{+64}_{-33}	$-0.01^{+0.0}_{-0.01}$	no
174	0.033	0.0	$0.281^{+0.001}_{-0.001}$	106^{+7}_{-3}	$-0.01^{+0.01}_{-0.02}$	no
175	0.033	0.005	$0.281^{+0.001}_{-0.001}$	106^{+7}_{-3}	$-0.02^{+0.01}_{-0.02}$	no
176	0.033	0.026	$0.281^{+0.001}_{-0.001}$	100^{+1}_{-1}	$-10.96^{+1.14}_{-0.37}$	no
177	0.1	0.001	$0.28^{+0.001}_{-0.001}$	104^{+5}_{-2}	$-0.01^{+0.01}_{-0.02}$	no
178	0.1	0.008	$0.28^{+0.001}_{-0.001}$	101^{+1}_{-1}	$-7.55^{+0.57}_{-3.6}$	no
179	0.1	0.041	$0.281^{+0.001}_{-0.001}$	112^{+13}_{-6}	$-0.02^{+0.01}_{-0.02}$	no
180	0.045	0.0	$0.28^{+0.001}_{-0.001}$	811^{+28}_{-22}	$-0.01^{+0.01}_{-0.01}$	no
181	0.045	0.003	$0.28^{+0.001}_{-0.001}$	101^{+1}_{-1}	$-5.51^{+0.62}_{-0.74}$	no
182	0.045	0.02	$0.281^{+0.001}_{-0.001}$	108^{+9}_{-4}	$-0.02^{+0.01}_{-0.02}$	no

183	0.067	0.001	$0.281^{+0.001}_{-0.001}$	295^{+1}_{-2}	$-0.01^{+0.0}_{-0.01}$	no
184	0.067	0.006	$0.281^{+0.001}_{-0.001}$	106^{+8}_{-3}	$-0.02^{+0.01}_{-0.02}$	no
185	0.067	0.033	$0.281^{+0.001}_{-0.001}$	111^{+11}_{-6}	$-0.02^{+0.01}_{-0.02}$	no
186	0.134	0.001	$0.28^{+0.001}_{-0.001}$	101^{+1}_{-1}	$-8.02^{+1.52}_{-2.85}$	no
187	0.134	0.009	$0.281^{+0.001}_{-0.001}$	105^{+6}_{-2}	$-0.01^{+0.01}_{-0.02}$	no
188	0.134	0.048	$0.279^{+0.001}_{-0.001}$	1489^{+8}_{-8}	$-0.01^{+0.01}_{-0.01}$	no
189	0.0	0.0	$0.281^{+0.001}_{-0.001}$	107^{+7}_{-3}	$-0.02^{+0.01}_{-0.02}$	no
190	0.0	0.0	$0.28^{+0.001}_{-0.001}$	101^{+1}_{-1}	$-6.31^{+0.5}_{-1.3}$	no
191	0.0	0.004	$0.281^{+0.001}_{-0.001}$	115^{+3}_{-3}	$-0.02^{+0.01}_{-0.01}$	no
192	0.017	0.0	$0.281^{+0.001}_{-0.001}$	106^{+7}_{-3}	$-0.02^{+0.01}_{-0.02}$	no
193	0.017	0.003	$0.281^{+0.001}_{-0.001}$	107^{+9}_{-3}	$-0.02^{+0.01}_{-0.02}$	no
194	0.017	0.015	$0.281^{+0.001}_{-0.001}$	107^{+8}_{-4}	$-0.02^{+0.01}_{-0.02}$	no
195	0.069	0.0	$0.28^{+0.001}_{-0.001}$	576^{+3}_{-5}	$-0.0^{+0.0}_{-0.01}$	no
196	0.069	0.005	$0.281^{+0.001}_{-0.001}$	105^{+6}_{-3}	$-0.02^{+0.01}_{-0.02}$	no
197	0.069	0.026	$0.281^{+0.001}_{-0.001}$	152^{+13}_{-4}	$-0.01^{+0.0}_{-0.0}$	no
198	0.011	0.0	$0.281^{+0.001}_{-0.001}$	108^{+9}_{-5}	$-0.02^{+0.01}_{-0.02}$	no
199	0.011	0.002	$0.281^{+0.001}_{-0.001}$	106^{+7}_{-3}	$-0.02^{+0.01}_{-0.02}$	no
200	0.011	0.011	$0.28^{+0.001}_{-0.001}$	101^{+1}_{-1}	$-5.88^{+0.5}_{-0.69}$	no
201	0.028	0.0	$0.281^{+0.001}_{-0.001}$	144^{+1}_{-2}	$-0.02^{+0.01}_{-0.01}$	no
202	0.028	0.004	$0.279^{+0.001}_{-0.001}$	1264^{+98}_{-63}	$-0.02^{+0.01}_{-0.01}$	no
203	0.028	0.021	$0.281^{+0.001}_{-0.001}$	108^{+9}_{-4}	$-0.02^{+0.01}_{-0.02}$	no
204	0.077	0.001	$0.281^{+0.001}_{-0.001}$	105^{+6}_{-3}	$-0.02^{+0.01}_{-0.02}$	no
205	0.077	0.005	$0.281^{+0.001}_{-0.001}$	105^{+7}_{-3}	$-0.02^{+0.01}_{-0.02}$	no
206	0.077	0.026	$0.281^{+0.001}_{-0.001}$	109^{+11}_{-5}	$-0.02^{+0.01}_{-0.02}$	no
207	0.045	0.0	$0.281^{+0.001}_{-0.001}$	106^{+7}_{-3}	$-0.02^{+0.01}_{-0.02}$	no
208	0.045	0.003	$0.281^{+0.001}_{-0.001}$	107^{+8}_{-4}	$-0.02^{+0.01}_{-0.02}$	no

209	0.045	0.017	$0.281^{+0.001}_{-0.001}$	111^{+7}_{-5}	$-0.1^{+0.01}_{-0.0}$	no
210	0.058	0.0	$0.28^{+0.001}_{-0.001}$	101^{+1}_{-1}	$-7.6^{+0.14}_{-0.16}$	no
211	0.058	0.004	$0.281^{+0.001}_{-0.001}$	106^{+7}_{-3}	$-0.02^{+0.01}_{-0.02}$	no
212	0.058	0.021	$0.279^{+0.001}_{-0.001}$	1164^{+84}_{-80}	$-0.01^{+0.0}_{-0.01}$	no
213	0.095	0.0	$0.281^{+0.001}_{-0.001}$	105^{+6}_{-3}	$-0.02^{+0.01}_{-0.02}$	no
214	0.095	0.005	$0.281^{+0.001}_{-0.001}$	106^{+7}_{-3}	$-0.02^{+0.01}_{-0.02}$	no
215	0.095	0.027	$0.28^{+0.001}_{-0.001}$	670^{+10}_{-28}	$-0.04^{+0.01}_{-0.01}$	no
216	0.0	0.0	$0.281^{+0.001}_{-0.001}$	115^{+9}_{-2}	$-0.02^{+0.01}_{-0.02}$	no
217	0.0	0.0	$0.281^{+0.001}_{-0.001}$	106^{+7}_{-3}	$-0.02^{+0.01}_{-0.02}$	no
218	0.0	0.003	$0.281^{+0.001}_{-0.001}$	106^{+7}_{-3}	$-0.01^{+0.01}_{-0.01}$	no
219	0.008	0.0	$0.281^{+0.001}_{-0.001}$	106^{+7}_{-3}	$-0.02^{+0.01}_{-0.02}$	no
220	0.008	0.001	$0.28^{+0.001}_{-0.001}$	101^{+1}_{-1}	$-7.68^{+0.95}_{-3.07}$	no
221	0.008	0.006	$0.281^{+0.001}_{-0.001}$	106^{+6}_{-3}	$-0.02^{+0.01}_{-0.02}$	no
222	0.031	0.0	$0.279^{+0.001}_{-0.001}$	1195^{+17}_{-15}	$-0.01^{+0.0}_{-0.01}$	no
223	0.031	0.002	$0.281^{+0.001}_{-0.001}$	107^{+8}_{-4}	$-0.02^{+0.01}_{-0.02}$	no
224	0.031	0.011	$0.281^{+0.001}_{-0.001}$	107^{+8}_{-4}	$-0.02^{+0.01}_{-0.02}$	no
225	0.011	0.0	$0.281^{+0.001}_{-0.001}$	106^{+7}_{-3}	$-0.02^{+0.01}_{-0.02}$	no
226	0.011	0.002	$0.281^{+0.001}_{-0.001}$	105^{+3}_{-3}	$-0.16^{+0.0}_{-0.02}$	no
227	0.011	0.009	$0.281^{+0.001}_{-0.001}$	106^{+7}_{-3}	$-0.02^{+0.01}_{-0.02}$	no
228	0.016	0.0	$0.281^{+0.001}_{-0.001}$	106^{+7}_{-3}	$-0.02^{+0.01}_{-0.02}$	no
229	0.016	0.002	$0.279^{+0.001}_{-0.001}$	889^{+30}_{-23}	$-0.01^{+0.0}_{-0.01}$	no
230	0.016	0.01	$0.281^{+0.001}_{-0.001}$	108^{+7}_{-4}	$-0.02^{+0.01}_{-0.02}$	no
231	0.031	0.0	$0.281^{+0.001}_{-0.001}$	107^{+8}_{-3}	$-0.02^{+0.01}_{-0.02}$	no
232	0.031	0.002	$0.28^{+0.001}_{-0.001}$	101^{+1}_{-1}	$-5.59^{+0.38}_{-0.35}$	no
233	0.031	0.011	$0.281^{+0.001}_{-0.001}$	108^{+8}_{-4}	$-0.02^{+0.01}_{-0.02}$	no
234	0.045	0.0	$0.281^{+0.001}_{-0.001}$	106^{+7}_{-3}	$-0.02^{+0.01}_{-0.02}$	no

235	0.045	0.003	$0.281^{+0.001}_{-0.001}$	142^{+7}_{-6}	$-0.02^{+0.01}_{-0.02}$	no
236	0.045	0.016	$0.279^{+0.001}_{-0.001}$	1206^{+11}_{-7}	$-0.0^{+0.0}_{-0.0}$	no
237	0.045	0.0	$0.281^{+0.001}_{-0.001}$	107^{+8}_{-3}	$-0.02^{+0.01}_{-0.02}$	no
238	0.045	0.003	$0.281^{+0.001}_{-0.001}$	107^{+8}_{-3}	$-0.02^{+0.01}_{-0.02}$	no
239	0.045	0.016	$0.279^{+0.001}_{-0.001}$	1099^{+82}_{-65}	$-0.01^{+0.0}_{-0.01}$	no
240	0.051	0.0	$0.281^{+0.001}_{-0.001}$	107^{+7}_{-3}	$-0.02^{+0.01}_{-0.02}$	no
241	0.051	0.003	$0.28^{+0.001}_{-0.001}$	775^{+47}_{-73}	$-0.01^{+0.0}_{-0.01}$	no
242	0.051	0.016	$0.281^{+0.001}_{-0.001}$	109^{+10}_{-4}	$-0.02^{+0.01}_{-0.02}$	no

Appendix D

Time dependence chromatic effects' analysis in HST observations

As discussed in section 3, processed data could be affected by time-dependent chromatic effects. For this reason, we analyzed separately the pre-transit and post transit data in order to compare the resulting spectra before and after the transit to look for any relevant difference, possible clue of time-dependent systematics in our data. In Fig. D.1 we show the resulting out-of-transit stellar spectra before and after transit. These two spectra clearly match each other and their differences are lower than their associated error and much lower than the differences between these spectra and their common best model. As a further check, we performed the analysis using only pre- or post-transit spectra to verify the self-consistency of our results about the stellar composition of the star. The results obtained from those analyses (see Table D.1) are consistent with the results reported in Table 5.2 confirming the self-consistency of our approach and the temperature and metallicity found in section 4.1.

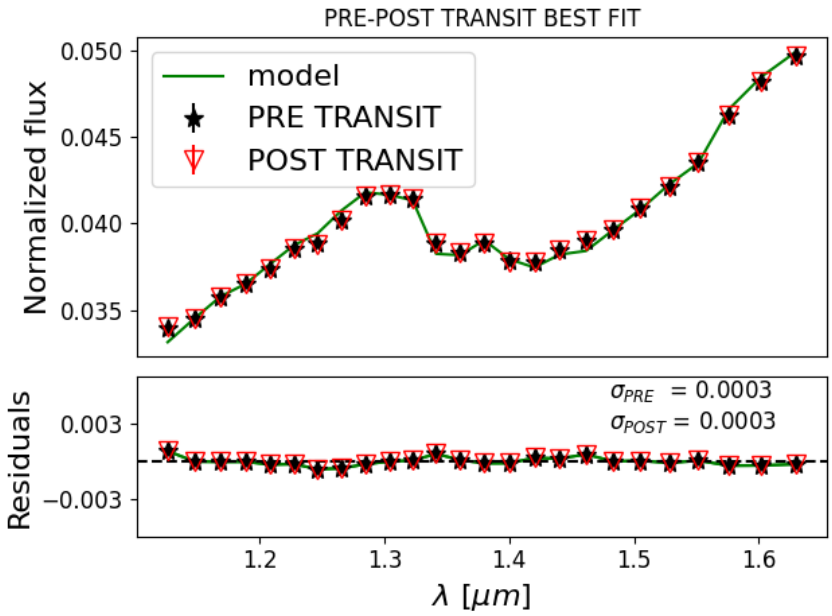

Figure D.1: Comparison between our best stellar model (green line), the pre-transit (black stars) and the post-transit (red triangles) mean stellar spectrum. It is clear that the pre-transit and post-transit spectra match each other with great precision and that their differences are negligible with respect to the residuals of the common best fit model. The error bars are too little to be visible in the figure.

Table D.1: List of χ^2 values from the analysis of pre-transit/post-transit spectra. We show for each stellar composition test the χ^2 at a given stellar temperature of 3100 K, 3200 K and 3300 K, the values of the stellar temperature nearest to the best fit of the data.

Z	α	χ^2_{3100K}	χ^2_{3200K}	χ^2_{3300K}
-1.0	0.0	4.29/4.29e-03	4.75/4.75e-03	4.94/4.94e-03
-0.5	0.0	3.05/3.05e-03	3.42/3.42e-03	3.70/3.70e-03
0.0	0.0	1.45/1.45e-03	1.91/1.91e-03	2.44/2.44e-03
+0.5	0.0	5.20/5.22e-04	1.04/1.04e-03	1.85/1.85e-03
+1.0	0.0	2.29/2.30e-04	8.12/8.14e-04	2.02/2.02e-03
-0.5	+0.2	2.25/2.26e-04	1.37/1.38e-04	3.65/3.66e-04
-1.0	0.4	4.39/4.40e-04	7.16/7.26e-05	1.32/1.33e-04

RINGRAZIAMENTI

Ringrazio la mia famiglia per il suo grandissimo e incondizionato supporto. Senza di loro non sarei mai arrivato dove sono.

Si ringrazia anche il mio "malefico", adorato fratellino.

Si ringrazia tutto il personale dell'Osservatorio Astronomico di Palermo - OAPA per avermi supportato (e sopportato) durante questi anni. Grazie di tutto davvero.

Ringrazio infine la fantastica tradizione degli schiticchi per i Kg acquisiti durante il lavoro in osservatorio.

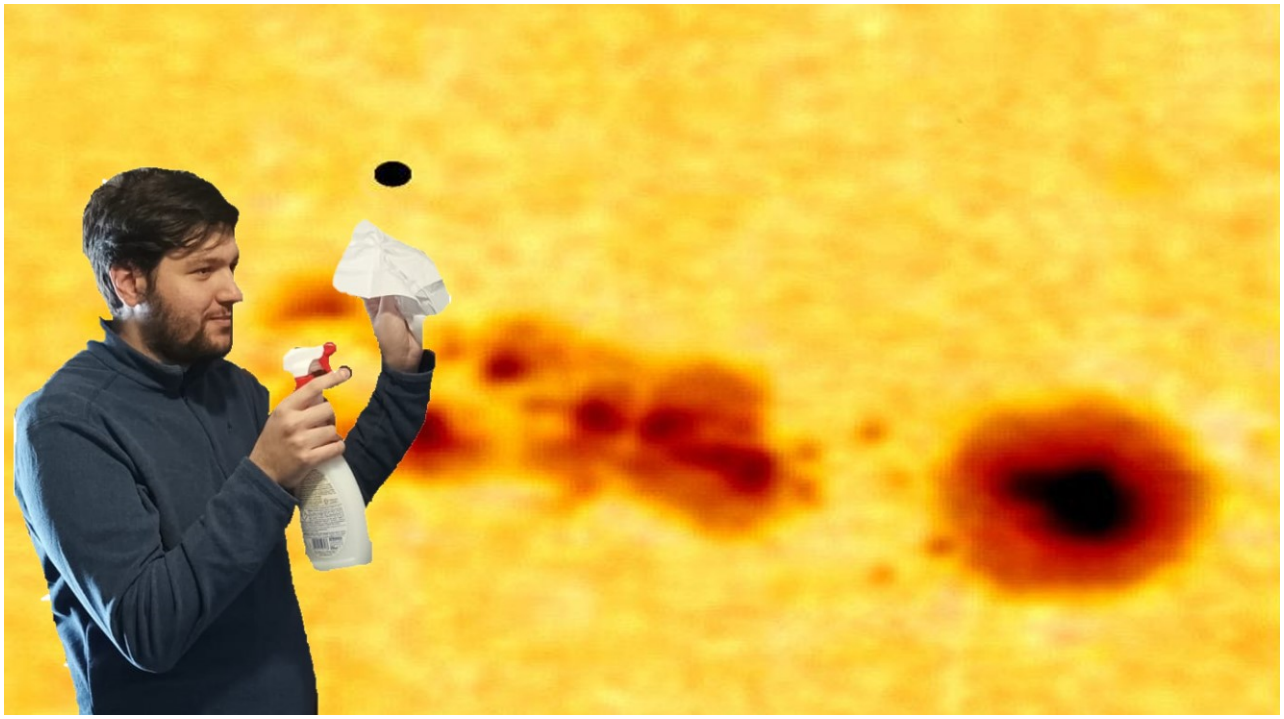

Figure D.2: Rara immagine del sottoscritto al lavoro per smacchiare le stelle (fonte: calendario EXOPA 2023).

List of Figures

Bibliography

Abel, Martin et al. (June 2011). "Collision-Induced Absorption by H2Pairs: From Hundreds to Thousands of Kelvin". In: *Journal of Physical Chemistry A* 115.25, pp. 6805–6812. DOI: 10.1021/jp109441f.

Agol, Eric et al. (Oct. 2010). "The Climate of HD 189733b from Fourteen Transits and Eclipses Measured by Spitzer". In: 721.2, pp. 1861–1877. DOI: 10.1088/0004-637X/721/2/1861. arXiv: 1007.4378 [astro-ph.EP].

Ash, A. et al. (Jan. 2020). "Rotationally Modulated Magnetic Variability in Praesepe K and M Dwarfs". In: *American Astronomical Society Meeting Abstracts #235*. Vol. 235. American Astronomical Society Meeting Abstracts, 273.09, p. 273.09.

Auvergne, M. et al. (Oct. 2009). "The CoRoT satellite in flight: description and performance". In: 506.1, pp. 411–424. DOI: 10.1051/0004-6361/200810860. arXiv: 0901.2206 [astro-ph.SR].

Ballerini, P. et al. (Mar. 2012). "Multiwavelength flux variations induced by stellar magnetic activity: effects on planetary transits". In: 539, A140, A140. DOI: 10.1051/0004-6361/201117102. arXiv: 1201.3514 [astro-ph.EP].

Batalha, Natasha E. et al. (June 2017). "PandExo: A Community Tool for Transiting Exoplanet Science with JWST & HST". In: 129.976, p. 064501. DOI: 10.1088/1538-3873/aa65b0. arXiv: 1702.01820 [astro-ph.IM].

Beeck, B. et al. (Oct. 2013). "Three-dimensional simulations of near-surface convection in main-sequence stars. I. Overall structure". In: 558, A48, A48. DOI: 10.1051/0004-6361/201321343. arXiv: 1308.4874 [astro-ph.SR].

Bensby, T., S. Feltzing, and I. Lundström (Nov. 2003). "Elemental abundance trends in the Galactic thin and thick disks as traced by nearby F and G dwarf stars". In: 410, pp. 527–551. DOI: 10.1051/0004-6361:20031213.

Bensby, T., S. Feltzing, I. Lundström, and I. Ilyin (Apr. 2005). "α-, r-, and s-process element trends in the Galactic thin and thick disks". In: 433.1, pp. 185–203. DOI: 10.1051/0004-6361:20040332. arXiv: astro-ph/0412132 [astro-ph].

Berdyugina, Svetlana V. (Dec. 2005). "Starspots: A Key to the Stellar Dynamo". In: *Living Reviews in Solar Physics* 2.1, 8, p. 8. DOI: 10.12942/lrsp-2005-8.

Berta, Zachory K., David Charbonneau, et al. (July 2011). "The GJ1214 Super-Earth System: Stellar Variability, New Transits, and a Search for Additional Planets". In: 736.1, 12, p. 12. DOI: 10.1088/0004-637X/736/1/12. arXiv: 1012.0518 [astro-ph.EP].

Berta, Zachory K., Jonathan Irwin, et al. (Nov. 2012). "Transit Detection in the MEarth Survey of Nearby M Dwarfs: Bridging the Clean-first, Search-later Divide". In: 144.5, 145, p. 145. DOI: 10.1088/0004-6256/144/5/145. arXiv: 1206.4715 [astro-ph.EP].

Biagini, Alfredo et al. (May 2024). "A reanalysis of the LHS 1140 b atmosphere observed with the Hubble Space Telescope". In: 530.1, pp. 1054–1065. DOI: 10.1093/mnras/stae823. arXiv: 2403.20285 [astro-ph.EP].

Blunt, Sarah et al. (Aug. 2023). "Overfitting Affects the Reliability of Radial Velocity Mass Estimates of the V1298 Tau Planets". In: 166.2, 62, p. 62. DOI: 10.3847/1538-3881/acde78. arXiv: 2306.08145 [astro-ph.EP].

Bonney, Paul and Julia Kennefick (June 2022). "On The Hydrosphere Stability of TESS Targets: Applications to 700 d, 256 b, and 203 b". In: *American Astronomical Society Meeting Abstracts*. Vol. 54. American Astronomical Society Meeting Abstracts, 309.03, p. 309.03.

Borsa, F. et al. (Nov. 2019). "The GAPS Programme with HARPS-N at TNG. XIX. Atmospheric Rossiter-McLaughlin effect and improved parameters of KELT-9b". In: 631, A34, A34. DOI: 10.1051/0004-6361/201935718. arXiv: 1907.10078 [astro-ph.EP].

Borucki, William J. et al. (Feb. 2010). "Kepler Planet-Detection Mission: Introduction and First Results". In: *Science* 327.5968, p. 977. DOI: 10.1126/science.1185402.

Buchner, J. et al. (Apr. 2014). "X-ray spectral modelling of the AGN obscuring region in the CDFS: Bayesian model selection and catalogue". In: 564, A125, A125. DOI: 10.1051/0004-6361/201322971. arXiv: 1402.0004 [astro-ph.HE].

Cadieux, Charles et al. (Oct. 2023). "New Mass and Radius Constraints on the LHS 1140 Planets – LHS 1140 b is Either a Temperate Mini-Neptune or a Water World". In: *arXiv e-prints*, arXiv:2310.15490, arXiv:2310.15490. DOI: 10.48550/arXiv.2310.15490. arXiv: 2310.15490 [astro-ph.EP].

Carleo, I. et al. (June 2020). "The GAPS Programme at TNG. XXI. A GIARPS case study of known young planetary candidates: confirmation of HD 285507 b and refutation of AD Leonis b". In: 638, A5, A5. DOI: 10.1051/0004-6361/201937369. arXiv: 2002.10562 [astro-ph.EP].

Catling, David C. and James F. Kasting (2017). *Atmospheric Evolution on Inhabited and Lifeless Worlds*.

Chaplin, W. J. and T. Appourchaux (Nov. 1999). "Depth of excitation and reversal of asymmetry of low-l solar P modes: a complementary analysis of BiSON* and VIRGO/SPM† data". In: 309.3, pp. 761–768. DOI: 10.1046/j.1365-8711.1999.02915.x.

Chatzistergos, Theodosios et al. (Nov. 2022). "Scrutinising the relationship between plage areas and sunspot areas and numbers". In: 667, A167, A167. DOI: 10.1051/0004-6361/202244913. arXiv: 2209.07077 [astro-ph.SR].

Claret, A. (Nov. 2000). "A new non-linear limb-darkening law for LTE stellar atmosphere models. Calculations for -5.0 ¡= log[M/H] ¡= +1, 2000 K ¡= T_{eff} ¡= 50000 K at several surface gravities". In: 363, pp. 1081–1190.

Claret, A., P. H. Hauschildt, and S. Witte (Oct. 2012). "New limb-darkening coefficients for PHOENIX/1D model atmospheres. I. Calculations for 1500 K $\leq T_{eff} \leq$ 4800 K Kepler, CoRot, Spitzer, uvby, UBVRIJHK, Sloan, and 2MASS photometric systems". In: 546, A14, A14. DOI: 10.1051/0004-6361/201219849.

Collins, Karen A., Kevin I. Collins, et al. (Nov. 2018). "The KELT Follow-up Network and Transit False-positive Catalog: Pre-vetted False Positives for TESS". In: 156.5, 234, p. 234. DOI: 10.3847/1538-3881/aae582. arXiv: 1803.01869 [astro-ph.EP].

Collins, Karen A., John F. Kielkopf, et al. (Feb. 2017). "AstroImageJ: Image Processing and Photometric Extraction for Ultra-precise Astronomical Light Curves". In: 153.2, 77, p. 77. DOI: 10.3847/1538-3881/153/2/77. arXiv: 1701.04817 [astro-ph.IM].

Conconi, Paolo et al. (Sept. 2004). "The commissioning of the REM-IR camera at La Silla". In: *Ground-based Instrumentation for Astronomy*. Ed. by Alan F. M. Moorwood and Masanori Iye. Vol. 5492. Society of Photo-Optical Instrumentation Engineers (SPIE) Conference Series, pp. 1602–1612. DOI: 10.1117/12.551289.

Cosentino, Rosario et al. (Sept. 2012). "Harps-N: the new planet hunter at TNG". In: *Ground-based and Airborne Instrumentation for Astronomy IV*. Ed. by Ian S. McLean, Suzanne K. Ramsay, and Hideki Takami. Vol. 8446. Society of Photo-Optical Instrumentation Engineers (SPIE) Conference Series, 84461V, p. 84461V. DOI: 10.1117/12.925738.

Covino, E. et al. (June 2013). "The GAPS programme with HARPS-N at TNG. I. Observations of the Rossiter-McLaughlin effect and characterisation of the transiting system Qatar-1". In: 554, A28, A28. DOI: 10.1051/0004-6361/201321298. arXiv: 1304.0005 [astro-ph.SR].

Cracchiolo, G., G. Micela, G. Morello, et al. (Nov. 2021). "Correcting the effect of stellar spots on ARIEL transmission spectra - II. The limb-darkening effect". In: 507.4, pp. 6118–6131. DOI: 10.1093/mnras/stab2509. arXiv: 2108.12526 [astro-ph.EP].

Cracchiolo, G., G. Micela, and G. Peres (Feb. 2021). "Correcting the effect of stellar spots on ARIEL transmission spectra". In: 501.2, pp. 1733–1747. DOI: 10.1093/mnras/staa3621. arXiv: 2011.10085 [astro-ph.SR].

Czesla, S. et al. (Oct. 2009). "How stellar activity affects the size estimates of extrasolar planets". In: 505.3, pp. 1277–1282. DOI: 10.1051/0004-6361/200912454. arXiv: 0906.3604 [astro-ph.SR].

David, Trevor J., Ann Marie Cody, et al. (Aug. 2019). "A Warm Jupiter-sized Planet Transiting the Pre-main-sequence Star V1298 Tau". In: 158.2, 79, p. 79. DOI: 10.3847/1538-3881/ab290f. arXiv: 1902.09670 [astro-ph.EP].

David, Trevor J., Erik A. Petigura, et al. (Nov. 2019). "Four Newborn Planets Transiting the Young Solar Analog V1298 Tau". In: 885.1, L12, p. L12. DOI: 10.3847/2041-8213/ab4c99. arXiv: 1910.04563 [astro-ph.EP].

Deming, Drake et al. (Sept. 2013). "Infrared Transmission Spectroscopy of the Exoplanets HD 209458b and XO-1b Using the Wide Field Camera-3 on the Hubble Space Telescope". In: 774.2, 95, p. 95. DOI: 10.1088/0004-637X/774/2/95. arXiv: 1302.1141 [astro-ph.EP].

Désert, J. -M. et al. (Feb. 2011). "Transit spectrophotometry of the exoplanet HD 189733b. II. New Spitzer observations at 3.6 μm". In: 526, A12, A12. DOI: 10.1051/0004-6361/200913093. arXiv: 1008.2481 [astro-ph.EP].

Di Maio, C., C. Argiroffi, et al. (Oct. 2020). "The GAPS programme at TNG. XXVI. Magnetic activity in M stars: spectroscopic monitoring of AD Leonis". In: 642, A53, A53. DOI: 10.1051/0004-6361/202038011. arXiv: 2008.04242 [astro-ph.SR].

Di Maio, C., Q. Changeat, et al. (Jan. 2023). "Analysis of the planetary mass uncertainties on the accuracy of atmospherical retrieval". In: 669, A150, A150. DOI: 10.1051/0004-6361/202244881. arXiv: 2211.02897 [astro-ph.EP].

Di Maio, C., A. Petralia, et al. (Dec. 2023). "The GAPS programme at TNG LII. Spot modeling of V1298 Tau using SpotCCF tool". In: *arXiv e-prints*, arXiv:2312.14269, arXiv:2312.14269. DOI: 10.48550/arXiv.2312.14269. arXiv: 2312.14269 [astro-ph.SR].

— (Mar. 2024). "The GAPS programme at TNG. LII. Spot modelling of V1298 Tau using the SpotCCF tool". In: 683, A239, A239. DOI: 10.1051/0004-6361/202348223. arXiv: 2312.14269 [astro-ph.SR].

Dittmann, Jason A. et al. (Apr. 2017). "A temperate rocky super-Earth transiting a nearby cool star". In: 544.7650, pp. 333–336. DOI: 10.1038/nature22055. arXiv: 1704.05556 [astro-ph.EP].

Domingo, V., B. Fleck, and A. I. Poland (Dec. 1995). "The SOHO Mission: an Overview". In: 162.1-2, pp. 1–37. DOI: 10.1007/BF00733425.

Dressing, Courtney D. and David Charbonneau (July 2015). "The Occurrence of Potentially Habitable Planets Orbiting M Dwarfs Estimated from the Full Kepler Dataset and an Empirical Measurement of the Detection Sensitivity". In: 807.1, 45, p. 45. DOI: 10.1088/0004-637X/807/1/45. arXiv: 1501.01623 [astro-ph.EP].

Edwards, Billy, Quentin Changeat, et al. (Jan. 2021). "Hubble WFC3 Spectroscopy of the Habitable-zone Super-Earth LHS 1140 b". In: 161.1, 44, p. 44. DOI: 10.3847/1538-3881/abc6a5. arXiv: 2011.08815 [astro-ph.EP].

Edwards, Billy, Lorenzo Mugnai, et al. (Sept. 2019). "An Updated Study of Potential Targets for Ariel". In: *EPSC-DPS Joint Meeting 2019*. Vol. 2019, EPSC-DPS2019-603, EPSC-DPS2019–603.

Feinstein, Adina D. et al. (Jan. 2022). "V1298 Tau with TESS: Updated Ephemerides, Radii, and Period Constraints from a Second Transit of V1298 Tau e". In: 925.1, L2, p. L2. DOI: 10.3847/2041-8213/ac4745. arXiv: 2111.08660 [astro-ph.EP].

Feroz, F., M. P. Hobson, and M. Bridges (Oct. 2009). "MULTINEST: an efficient and robust Bayesian inference tool for cosmology and particle physics". In: 398.4, pp. 1601–1614. DOI: 10.1111/j.1365-2966.2009.14548.x. arXiv: 0809.3437 [astro-ph].

Fletcher, Leigh N., Magnus Gustafsson, and Glenn S. Orton (Mar. 2018). "Hydrogen Dimers in Giant-planet Infrared Spectra". In: 235.1, 24, p. 24. DOI: 10.3847/1538-4365/aaa07a. arXiv: 1712.02813 [astro-ph.EP].

Foreman-Mackey, Daniel et al. (Mar. 2013). "emcee: The MCMC Hammer". In: 125.925, p. 306. DOI: 10.1086/670067. arXiv: 1202.3665 [astro-ph.IM].

Fröhlich, Claus et al. (Jan. 1997). "First Results from VIRGO, the Experiment for Helioseismology and Solar Irradiance Monitoring on SOHO". In: 170.1, pp. 1–25. DOI: 10.1023/A:1004969622753.

Fulton, Benjamin J. et al. (Sept. 2017). "The California-Kepler Survey. III. A Gap in the Radius Distribution of Small Planets". In: 154.3, 109, p. 109. DOI: 10.3847/1538-3881/aa80eb. arXiv: 1703.10375 [astro-ph.EP].

Gaia Collaboration et al. (June 2023). "Gaia Data Release 3. Summary of the content and survey properties". In: 674, A1, A1. DOI: 10.1051/0004-6361/202243940. arXiv: 2208.00211 [astro-ph.GA].

Gomes, G. O. and S. Ferraz-Mello (June 2020). "Tidal evolution of exoplanetary systems hosting potentially habitable exoplanets. The cases of LHS-1140 b-c and K2-18 b-c". In: 494.4, pp. 5082–5090. DOI: 10.1093/mnras/staa1110. arXiv: 2005.10318 [astro-ph.EP].

Goulding, N. T. et al. (Dec. 2012). "J-band variability of M dwarfs in the WFCAM Transit Survey". In: 427.4, pp. 3358–3373. DOI: 10.1111/j.1365-2966.2012.21932.x. arXiv: 1211.5288 [astro-ph.SR].

Greene, Thomas P. et al. (Jan. 2016). "Characterizing Transiting Exoplanet Atmospheres with JWST". In: 817.1, 17, p. 17. DOI: 10.3847/0004-637X/817/1/17. arXiv: 1511.05528 [astro-ph.EP].

Gully-Santiago, Michael A. et al. (Feb. 2017). "Placing the Spotted T Tauri Star LkCa 4 on an HR Diagram". In: 836.2, 200, p. 200. DOI: 10.3847/1538-4357/836/2/200. arXiv: 1701.06703 [astro-ph.SR].

Husser, T. -O. et al. (May 2013). "A new extensive library of PHOENIX stellar atmospheres and synthetic spectra". In: 553, A6, A6. DOI: 10.1051/0004-6361/201219058. arXiv: 1303.5632 [astro-ph.SR].

Jackson, R. J. and R. D. Jeffries (May 2013). "On the relationship between the size and surface coverage of starspots on magnetically active low-mass stars". In: 431.2, pp. 1883–1890. DOI: 10.1093/mnras/stt304. arXiv: 1302.4202 [astro-ph.SR].

Jakobsen, P. et al. (May 2022). "The Near-Infrared Spectrograph (NIRSpec) on the James Webb Space Telescope. I. Overview of the instrument and its capabilities". In: 661, A80, A80. DOI: 10.1051/0004-6361/202142663. arXiv: 2202.03305 [astro-ph.IM].

Järvinen, S. P. et al. (Dec. 2018). "Mapping EK Draconis with PEPSI. Possible evidence for starspot penumbrae". In: 620, A162, A162. DOI: 10.1051/0004-6361/201833496. arXiv: 1812.03675 [astro-ph.SR].

Kass, Robert E. and Adrian E. Raftery (1995). "Bayes Factors". In: *Journal of the American Statistical Association* 90.430, pp. 773–795. DOI: 10.1080/01621459.1995.10476572.

Klein, Baptiste et al. (June 2022). "One year of AU Mic with HARPS - II. Stellar activity and star-planet interaction". In: 512.4, pp. 5067–5084. DOI: 10.1093/mnras/stac761. arXiv: 2203.08190 [astro-ph.EP].

Kokori, Anastasia et al. (Apr. 2022). "ExoClock project: an open platform for monitoring the ephemerides of Ariel targets with contributions from the public". In: *Experimental Astronomy* 53.2, pp. 547–588. DOI: 10.1007/s10686-020-09696-3. arXiv: 2012.07478 [astro-ph.EP].

Kowalski, Adam F. (Feb. 2024). "Stellar flares". In: *arXiv e-prints*, arXiv:2402.07885, arXiv:2402.07885. DOI: 10.48550/arXiv.2402.07885. arXiv: 2402.07885 [astro-ph.SR].

Kreidberg, Laura et al. (Jan. 2014). "Clouds in the atmosphere of the super-Earth exoplanet GJ1214b". In: 505.7481, pp. 69–72. DOI: 10.1038/nature12888. arXiv: 1401.0022 [astro-ph.EP].

Kuntschner, H. et al. (Jan. 2011). *Revised Flux Calibration of the WFC3 G102 and G141 grisms*. ST-ECF Instrument Science Report WFC3-2011-05, 13 pages.

Kutyrev, A. S. et al. (July 2008). "Microshutter arrays: high contrast programmable field masks for JWST NIRSpec". In: *Space Telescopes and Instrumentation 2008: Optical, Infrared, and Millimeter*. Ed. by Jr. Oschmann Jacobus M., Mattheus W. M. de Graauw, and Howard A. MacEwen. Vol. 7010. Society of Photo-Optical Instrumentation Engineers (SPIE) Conference Series, 70103D, p. 70103D. DOI: 10.1117/12.790192.

Latham, David W. et al. (May 2011). "A First Comparison of Kepler Planet Candidates in Single and Multiple Systems". In: 732.2, L24, p. L24. DOI: 10.1088/2041-8205/732/2/L24. arXiv: 1103.3896 [astro-ph.EP].

Luger, Rodrigo et al. (Sept. 2021). "Mapping Stellar Surfaces. I. Degeneracies in the Rotational Light-curve Problem". In: 162.3, 123, p. 123. DOI: 10.3847/1538-3881/abfdb8. arXiv: 2102.00007 [astro-ph.SR].

Maldonado, J., R. M. Martínez-Arnáiz, et al. (Oct. 2010). "A spectroscopy study of nearby late-type stars, possible members of stellar kinematic groups". In: 521, A12, A12. DOI: 10.1051/0004-6361/201014948. arXiv: 1007.1132 [astro-ph.SR].

Maldonado, J., G. Micela, et al. (Dec. 2020). "HADES RV programme with HARPS-N at TNG. XII. The abundance signature of M dwarf stars with planets". In: 644, A68, A68. DOI: 10.1051/0004-6361/202039478. arXiv: 2010.14867 [astro-ph.SR].

Mandel, Kaisey and Eric Agol (Dec. 2002). "Analytic Light Curves for Planetary Transit Searches". In: 580.2, pp. L171–L175. DOI: 10.1086/345520. arXiv: astro-ph/0210099 [astro-ph].

Mantovan, G. et al. (Feb. 2024). "The GAPS programme at TNG. XLIX. TOI-5398, the youngest compact multi-planet system composed of an inner sub-Neptune and an outer warm Saturn". In: 682, A129, A129. DOI: 10.1051/0004-6361/202347472. arXiv: 2310.16888 [astro-ph.EP].

Mayor, M. et al. (Dec. 2003). "Setting New Standards with HARPS". In: *The Messenger* 114, pp. 20–24.

Mayor, Michel and Didier Queloz (Nov. 1995). "A Jupiter-mass companion to a solar-type star". In: 378.6555, pp. 355–359. DOI: 10.1038/378355a0.

McCullough, P. and J. MacKenty (May 2012). *Considerations for using Spatial Scans with WFC3*. Instrument Science Report WFC3 2012-08, 17 pages.

McQuillan, A., T. Mazeh, and S. Aigrain (Apr. 2014). "Rotation Periods of 34,030 Kepler Main-sequence Stars: The Full Autocorrelation Sample". In: 211.2, 24, p. 24. DOI: 10.1088/0067-0049/211/2/24. arXiv: 1402.5694 [astro-ph.SR].

Méndez, Abel and Edgard G. Rivera-Valentín (Mar. 2017). "The Equilibrium Temperature of Planets in Elliptical Orbits". In: 837.1, L1, p. L1. DOI: 10.3847/2041-8213/aa5f13. arXiv: 1702.07314 [astro-ph.EP].

Ment, Kristo et al. (Jan. 2019). "A Second Terrestrial Planet Orbiting the Nearby M Dwarf LHS 1140". In: 157.1, 32, p. 32. DOI: 10.3847/1538-3881/aaf1b1. arXiv: 1808.00485 [astro-ph.EP].

Micela, Giuseppina (Dec. 2015). "EChO spectra and stellar activity - I. Correcting the infrared signal using simultaneous optical spectroscopy". In: *Experimental Astronomy* 40.2-3, pp. 723–732. DOI: 10.1007/s10686-014-9430-1.

Modirrousta-Galian, Darius, Daniele Locci, and Giuseppina Micela (Mar. 2020). "The Bimodal Distribution in Exoplanet Radii: Considering Varying Core Compositions and H_2 Envelope's Sizes". In: 891.2, 158, p. 158. DOI: 10.3847/1538-4357/ab7379. arXiv: 2002.02166 [astro-ph.EP].

Molinari, E. et al. (Sept. 2004). "REM. Rapid Eye Mount". In: *Gamma-Ray Bursts: 30 Years of Discovery*. Ed. by E. Fenimore and M. Galassi. Vol. 727. American Institute of Physics Conference Series. AIP, pp. 765–768. DOI: 10.1063/1.1810954.

Molinari, Emilio et al. (July 2014). "ROS2: a multichannel vision for the robotic REM telescope". In: *Ground-based and Airborne Instrumentation for Astronomy V*. Ed. by Suzanne K. Ramsay, Ian S. McLean, and Hideki Takami. Vol. 9147. Society of Photo-

Optical Instrumentation Engineers (SPIE) Conference Series, 91476X, p. 91476X. DOI: 10.1117/12.2056390.

Morbidelli, Alessandro and Sean N. Raymond (Oct. 2016). "Challenges in planet formation". In: *Journal of Geophysical Research (Planets)* 121.10, pp. 1962–1980. DOI: 10.1002/2016JE005088. arXiv: 1610.07202 [astro-ph.EP].

Morello, G. et al. (Feb. 2020). "The ExoTETHyS Package: Tools for Exoplanetary Transits around Host Stars". In: 159.2, 75, p. 75. DOI: 10.3847/1538-3881/ab63dc. arXiv: 1908.09599 [astro-ph.EP].

Mugnai, Lorenzo et al. (Sept. 2019). "ArielRad: the ARIEL Radiometric Model". In: 2019, EPSC-DPS2019-270, EPSC-DPS2019–270.

Mugnai, Lorenzo V. et al. (Oct. 2020). "ArielRad: the Ariel radiometric model". In: *Experimental Astronomy* 50.2-3, pp. 303–328. DOI: 10.1007/s10686-020-09676-7. arXiv: 2009.07824 [astro-ph.IM].

Murray-Clay, Ruth A., Eugene I. Chiang, and Norman Murray (Mar. 2009). "Atmospheric Escape From Hot Jupiters". In: 693.1, pp. 23–42. DOI: 10.1088/0004-637X/693/1/23. arXiv: 0811.0006 [astro-ph].

Newton, Elisabeth R., Jonathan Irwin, et al. (Apr. 2016). "The Impact of Stellar Rotation on the Detectability of Habitable Planets around M Dwarfs". In: 821.1, L19, p. L19. DOI: 10.3847/2041-8205/821/1/L19. arXiv: 1604.03135 [astro-ph.EP].

Newton, Elisabeth R., Nicholas Mondrik, et al. (Nov. 2018). "New Rotation Period Measurements for M Dwarfs in the Southern Hemisphere: An Abundance of Slowly Rotating, Fully Convective Stars". In: 156.5, 217, p. 217. DOI: 10.3847/1538-3881/aad73b. arXiv: 1807.09365 [astro-ph.SR].

Newville, Matthew et al. (Sept. 2014). *LMFIT: Non-Linear Least-Square Minimization and Curve-Fitting for Python*. Version 0.8.0. DOI: 10.5281/zenodo.11813.

Noyes, R. W. et al. (Apr. 1984). "Rotation, convection, and magnetic activity in lower main-sequence stars." In: 279, pp. 763–777. DOI: 10.1086/161945.

Osborn, J. et al. (Sept. 2015). "Atmospheric scintillation in astronomical photometry". In: 452.2, pp. 1707–1716. DOI: 10.1093/mnras/stv1400. arXiv: 1506.06921 [astro-ph.IM].

Oshagh, M. et al. (Aug. 2014). "Impact of occultations of stellar active regions on transmission spectra. Can occultation of a plage mimic the signature of a blue sky?" In: 568, A99, A99. DOI: 10.1051/0004-6361/201424059. arXiv: 1407.2066 [astro-ph.EP].

Pizzolato, N. et al. (Jan. 2003). "The stellar activity-rotation relationship revisited: Dependence of saturated and non-saturated X-ray emission regimes on stellar mass for late-type dwarfs". In: 397, pp. 147–157. DOI: 10.1051/0004-6361:20021560.

Polyansky, Oleg L. et al. (Oct. 2018). "ExoMol molecular line lists XXX: a complete high-accuracy line list for water". In: 480.2, pp. 2597–2608. DOI: 10.1093/mnras/sty1877. arXiv: 1807.04529 [astro-ph.EP].

Pont, F., H. Knutson, et al. (Mar. 2008). "Detection of atmospheric haze on an extrasolar planet: the 0.55-1.05 μm transmission spectrum of HD 189733b with the HubbleSpaceTelescope". In: 385.1, pp. 109–118. DOI: 10.1111/j.1365-2966.2008.12852.x. arXiv: 0712.1374 [astro-ph].

Pont, F., D. K. Sing, et al. (July 2013). "The prevalence of dust on the exoplanet HD 189733b from Hubble and Spitzer observations". In: 432.4, pp. 2917–2944. DOI: 10.1093/mnras/stt651. arXiv: 1210.4163 [astro-ph.EP].

Rackham, Benjamin V., Dániel Apai, and Mark S. Giampapa (Feb. 2018). "The Transit Light Source Effect: False Spectral Features and Incorrect Densities for M-dwarf Transiting Planets". In: 853.2, 122, p. 122. DOI: 10.3847/1538-4357/aaa08c. arXiv: 1711.05691 [astro-ph.EP].

Al-Refaie, A. F. et al. (Aug. 2021). "TauREx 3: A Fast, Dynamic, and Extendable Framework for Retrievals". In: 917.1, 37, p. 37. DOI: 10.3847/1538-4357/ac0252. arXiv: 1912.07759 [astro-ph.IM].

Ricker, George R. et al. (Jan. 2015). "Transiting Exoplanet Survey Satellite (TESS)". In: *Journal of Astronomical Telescopes, Instruments, and Systems* 1, 014003, p. 014003. DOI: 10.1117/1.JATIS.1.1.014003.

Rogers, Leslie A. (Mar. 2015). "Most 1.6 Earth-radius Planets are Not Rocky". In: 801.1, 41, p. 41. DOI: 10.1088/0004-637X/801/1/41. arXiv: 1407.4457 [astro-ph.EP].

Sarkar, Subhajit et al. (Dec. 2018). "Stellar pulsation and granulation as noise sources in exoplanet transit spectroscopy in the ARIEL space mission". In: 481.3, pp. 2871–2877. DOI: 10.1093/mnras/sty2453. arXiv: 1809.05683 [astro-ph.EP].

Scandariato, Gaetano and Giuseppina Micela (Dec. 2015). "EChO spectra and stellar activity II. The case of dM stars". In: *Experimental Astronomy* 40.2-3, pp. 711–722. DOI: 10.1007/s10686-014-9390-5. arXiv: 1401.6947 [astro-ph.IM].

Schoonenberg, Djoeke and Chris W. Ormel (June 2017). "Planetesimal formation near the snowline: in or out?" In: 602, A21, A21. DOI: 10.1051/0004-6361/201630013. arXiv: 1702.02151 [astro-ph.EP].

Schou, J. et al. (Jan. 2012). "Design and Ground Calibration of the Helioseismic and Magnetic Imager (HMI) Instrument on the Solar Dynamics Observatory (SDO)". In: 275.1-2, pp. 229–259. DOI: 10.1007/s11207-011-9842-2.

Seager, S. and G. Mallén-Ornelas (Mar. 2003). "A Unique Solution of Planet and Star Parameters from an Extrasolar Planet Transit Light Curve". In: 585.2, pp. 1038–1055. DOI: 10.1086/346105. arXiv: astro-ph/0206228 [astro-ph].

Seinfeld, John H., Spyros N. Pandis, and Kevin Noone (Oct. 1998). "Atmospheric Chemistry and Physics: From Air Pollution to Climate Change". In: *Physics Today* 51.10, p. 88. DOI: 10.1063/1.882420.

Sing, D. K., J. -M. Désert, J. J. Fortney, et al. (Mar. 2011). "Gran Telescopio Canarias OSIRIS transiting exoplanet atmospheric survey: detection of potassium in XO-2b from narrowband spectrophotometry". In: 527, A73, A73. DOI: 10.1051/0004-6361/201015579. arXiv: 1008.4795 [astro-ph.EP].

Sing, D. K., J. -M. Désert, A. Lecavelier Des Etangs, et al. (Oct. 2009). "Transit spectrophotometry of the exoplanet HD 189733b. I. Searching for water but finding haze with HST NICMOS". In: 505.2, pp. 891–899. DOI: 10.1051/0004-6361/200912776. arXiv: 0907.4991 [astro-ph.EP].

Sing, D. K., F. Pont, et al. (Sept. 2011). "Hubble Space Telescope transmission spectroscopy of the exoplanet HD 189733b: high-altitude atmospheric haze in the optical and near-ultraviolet with STIS". In: 416.2, pp. 1443–1455. DOI: 10.1111/j.1365-2966.2011.19142.x. arXiv: 1103.0026 [astro-ph.EP].

Skumanich, A. (Feb. 1972). "Time Scales for Ca II Emission Decay, Rotational Braking, and Lithium Depletion". In: 171, p. 565. DOI: 10.1086/151310.

Sneep, Maarten and Wim Ubachs (May 2005). "Direct measurement of the Rayleigh scattering cross section in various gases". In: 92.3, pp. 293–310. DOI: 10.1016/j.jqsrt.2004.07.025.

Solanki, Sami K. (Jan. 2003). "Sunspots: An overview". In: 11.2-3, pp. 153–286. DOI: 10.1007/s00159-003-0018-4.

Solanki, Sami K., Bernd Inhester, and Manfred Schüssler (Mar. 2006). "The solar magnetic field". In: *Reports on Progress in Physics* 69.3, pp. 563–668. DOI: 10.1088/0034-4885/69/3/R02. arXiv: 1008.0771 [astro-ph.SR].

Spinelli, R. et al. (July 2019). "The high-energy radiation environment of the habitable-zone super-Earth LHS 1140b". In: 627, A144, A144. DOI: 10.1051/0004-6361/201935636. arXiv: 1906.08783 [astro-ph.EP].

Spinelli, Riccardo et al. (May 2023). "Planetary Parameters, XUV Environments, and Mass-loss Rates for Nearby Gaseous Planets with X-Ray-detected Host Stars". In: 165.5, 200, p. 200. DOI: 10.3847/1538-3881/acc336. arXiv: 2208.01650 [astro-ph.EP].

Suárez Mascareño, A. et al. (Dec. 2021). "Rapid contraction of giant planets orbiting the 20-million-year-old star V1298 Tau". In: *Nature Astronomy* 6, pp. 232–240. DOI: 10.1038/s41550-021-01533-7. arXiv: 2111.09193 [astro-ph.EP].

Thompson, Alexandra et al. (Feb. 2023). "Correcting Exoplanet Transmission Spectra for Stellar Activity with an Optimised Retrieval Framework". In: *arXiv e-prints*, arXiv:2302.04574, arXiv:2302.04574. DOI: 10.48550/arXiv.2302.04574. arXiv: 2302.04574 [astro-ph.EP].

— (Jan. 2024). "Correcting Exoplanet Transmission Spectra for Stellar Activity with an Optimized Retrieval Framework". In: 960.2, 107, p. 107. DOI: 10.3847/1538-4357/ad0369. arXiv: 2302.04574 [astro-ph.EP].

Tinetti, G. et al. (July 2016). "The science of ARIEL (Atmospheric Remote-sensing Infrared Exoplanet Large-survey)". In: *Space Telescopes and Instrumentation 2016: Optical, Infrared, and Millimeter Wave*. Ed. by Howard A. MacEwen et al. Vol. 9904. Society of Photo-Optical Instrumentation Engineers (SPIE) Conference Series, 99041X, p. 99041X. DOI: 10.1117/12.2232370.

Tinetti, Giovanna et al. (Nov. 2018). "A chemical survey of exoplanets with ARIEL". In: *Experimental Astronomy* 46.1, pp. 135–209. DOI: 10.1007/s10686-018-9598-x.

Tsiaras, A., I. P. Waldmann, M. Rocchetto, et al. (Dec. 2016). "A New Approach to Analyzing HST Spatial Scans: The Transmission Spectrum of HD 209458 b". In: 832.2, 202, p. 202. DOI: 10.3847/0004-637X/832/2/202. arXiv: 1511.07796 [astro-ph.EP].

Tsiaras, A., I. P. Waldmann, T. Zingales, et al. (Apr. 2018). "A Population Study of Gaseous Exoplanets". In: 155.4, 156, p. 156. DOI: 10.3847/1538-3881/aaaf75. arXiv: 1704.05413 [astro-ph.EP].

Varley, R., A. Tsiaras, and K. Karpouzas (July 2017). "Wayne—A Simulator for HST WFC3 IR Grism Spectroscopy". In: 231.1, 13, p. 13. DOI: 10.3847/1538-4365/aa7750. arXiv: 1511.09108 [astro-ph.IM].

Werner, M. W. et al. (Sept. 2004). "The Spitzer Space Telescope Mission". In: 154.1, pp. 1–9. DOI: 10.1086/422992. arXiv: astro-ph/0406223 [astro-ph].

Wolszczan, A. and D. A. Frail (Jan. 1992). "A planetary system around the millisecond pulsar PSR1257 + 12". In: 355.6356, pp. 145–147. DOI: 10.1038/355145a0.

Wunderlich, Fabian et al. (Apr. 2019). "Detectability of atmospheric features of Earth-like planets in the habitable zone around M dwarfs". In: 624, A49, A49. DOI: 10.1051/0004-6361/201834504. arXiv: 1905.02560 [astro-ph.EP].

Xu, Fukun, Shenghong Gu, and Panogiotis Ioannidis (Feb. 2021). "Starspot evolution, differential rotation, and correlation between chromospheric and photospheric activities on Kepler-411". In: 501.2, pp. 1878–1890. DOI: 10.1093/mnras/staa3793. arXiv: 2007.07158 [astro-ph.SR].

Yurchenko, Sergei N. et al. (Sept. 2017). "A hybrid line list for CH_4 and hot methane continuum". In: 605, A95, A95. DOI: 10.1051/0004-6361/201731026. arXiv: 1706.05724 [astro-ph.EP].

Zacharias, N. et al. (Feb. 2013). "The Fourth US Naval Observatory CCD Astrograph Catalog (UCAC4)". In: 145.2, 44, p. 44. DOI: 10.1088/0004-6256/145/2/44. arXiv: 1212.6182 [astro-ph.IM].

Zhang, Zhanbo et al. (Oct. 2018). "The Near-infrared Transmission Spectra of TRAPPIST-1 Planets b, c, d, e, f, and g and Stellar Contamination in Multi-epoch Transit Spectra". In: 156.4, 178, p. 178. DOI: 10.3847/1538-3881/aade4f. arXiv: 1802.02086 [astro-ph.EP].